Experimental Investigations of Mechanical Properties of Wet Granular Materials

Dissertation

zur Erlangung des Grades

des Doktors der Naturwissenschaften

der Naturwissenschaftlich - Technischen Fakultät II

- Physik und Mechatronik -

der Universität des Saarlandes

Von

Somnath Karmakar

Saarbrücken, Deutschland

2014

Typeset in LaTeX 2_ε.

Mitglieder des Prüfungsausschusses:

Dekan:	Univ.-Prof. Dr. rer. nat. Christian Wagner
Vorsitzender:	Univ.-Prof. Dr. rer. nat. Albrecht Ott
Erster Gutachter:	Univ.-Prof. Dr. rer. nat. Ralf Seemann
Zweiter Gutachter:	Univ.-Prof. Dr. rer. nat. Christian Wagner
Akademischer Mitarbeiter:	PD Dr. rer. nat. Hendrik Hähl

Tag der Einreichung: 30.01.2014

Tag des Kolloquium: 16.05.2014

Declaration:

I hereby declare that this submission is my own work and to the best of my knowledge, it contains no scientific material, previously published or written by other authors. The scientific results or concepts, taken from other resources, have been appropriately cited in the reference. For all copyright-images that appear in this document, permissions have been taken from respective authorities or concerned persons. Contributions made by all personnel are fully acknowledged. I also declare that for obtaining an academic degree, my thesis or its similar form was not submitted either in Germany or other countries.

M.Sc. Somnath Karmakar

Geometry of Fluid Interfaces Group

Faculty 7.2 Experimental Physics

Universität des Saarlandes

Saarbrücken, Germany

In memory of my loving father (1943 - 2013)

Abstract

Adding small amount of wetting fluid to dry granulates typically leads to the granular stiffness which arises due to the formation of minute liquid-contacts between individual granules by the virtue of capillary forces. We have experimentally studied the mechanical properties of wet granulates, composed of monodisperse spherical glass or basalt beads. The glass microspheres are almost perfectly wetted by water, whereas the basalt microspheres have a rather large contact angle with water. We have investigated the shear strength, measured under cyclic shear deformation for various system parameters like liquid content, shear rate and absolute pressure. At large absolute pressures, the associated energy dissipation of a sheared wet granular pile is considerably smaller than that of a completely dry bead assembly; where the wetting liquid might act as a 'liquid lubricant' by lowering the shear stiffness of wet bead piles. For wettable glass beads, the shear strength is observed to depend on the applied shear rate, whereas the shear strength of wet basalt bead assemblies are largely independent on the applied shear rate. With time resolved X-ray microtomography, we could shed some light on the underlying microscopic mechanisms of sheared wet granulates. We have explored variations in packing fraction during continuous shearing. We could identify that there is a volume-exchange process, occurring between distinct liquid morphologies within sheared wet glass bead piles. But, no such evolution dynamics of distributed liquid volumes is observed for cyclically sheared wet assembly of basalt granulates.

Kurzzusammenfassung

Generell gilt, dass bei Zugabe von kleinen Mengen einer benetzenden Flüssigkeit zu einem trockenen Granulate eine feuchtes Granulat mit erhöhter mechanischer Festigkeit entsteht. Der Grund dafür ist die attraktive Kapillarkohäsion aufgrund von Flüssigkeitsbrücken, die sich zwischen den einzelnen Ganulatkörnern ausbilden. Im Rahmen dieser Arbeit werden die mechanischen Eigenschaften verschiedener feuchter Granulate untersucht, bestehend aus monodispersen Glas- und Basaltmikrokugeln. Das Glasgranulat wird durch die verwendete Flüssigkeit (Wasser), nahezu vollständig benetzt mit geringer Kontakwinkelhysterese. Das Basaltgranulat weist eine geringere Benetzbarkeit und eine größere Kontaktwinkelhysteresis auf. Die mechanische Stabilität und Energiedissipation feuchter Granulate wurde unter zyklischer Scherung in Abhängigkeit unterschiedlicher Systemparameter wie Flüssigkeitsgehalt, Scherrate und Absolutdruck untersucht. Bei geringen Absolutdrücken ist die Energiedissipation in einem gescherten feuchten Granulat gegenüber einem trockenen Granulat deutlich erhöht. Bei großem Absolutdruck steigt die Energiedissipation an, kann aber bei einem feuchten Granulat wesentlich langsamer ansteigen als bei einem trockenen Granulat; Die Benetzungsflüssigkeit kann sich hierbeiwie eine 'Schmierflüssigkeit' verhalten. Dieses Verhalten ist unabhängig von der Benetzbarkeit der verwendeten Kugelgranulate. Interessanterweise beobachten wir zusätzlich einen Einfluß der aufgeprägte Scherrate auf die gemessene Scherfestigkeit der gut benetzbaren Glaskugelgranulaten; während die Scherfestigkeit von schlechter benetzbaren Basaltkugelgranulaten unabhängig von der aufgeprägten Scherrate ist. Mit Hilfe ultraschneller Röntgenmikrotomographie konnten die Reorganisationsprozess ingescherten feuchten Granulaten in Echtzeit bestimmt werden. Die Analyse der tomographischen Daten zeigte, dass während der kontinuierlichen Scherung eines benetzenden Glaskugelgranulats ein Flüssigkeitsaustauschprozess zwischen den einzelnen Flüssigkeitsstrukturen stattfindet. In einem gescherten Basaltkugelgranulat mit größerem Kontaktwinkel konnten hingegen keine derartige zeitliche Entwicklung der Flüssigkeitsstrukturen beobachtet werden.

Acknowledgements

I would like to express my gratitude to my project supervisor, **Prof. Dr. Ralf Seemann** for accepting my candidature in his group and introducing me to this fascinating field of wet granular materials. His motivating guidance, critical comments, our weekly group-meetings and the discussions have always been beneficial in extending my scientific knowledge. Above all, I have learnt from him to work with great patience, while all 'failures' keep knocking at the door.

I would like to acknowledge the 'Graduiertenkolleg-1276', Saarland University for providing the financial support during my PhD tenure. I am also indebted to all beamline scientists and staffs at ID-15A, ESRF, Grenoble (France) for their hospitality and cooperation in conducting our tomographic experiments. I am deeply grateful to the organizers of winter-schools, especially **Prof. Dr. Karin Jacobs** and **Prof. Dr. Ralf Seemann**. These winter-schools have greatly helped me to improve my presentation skills.

I wish to specially thank Dr. Mario Scheel for his support towards my very first experiments at Max Planck Institute for Dynamics and Self-Organization, Göttingen (Germany). I also have to admit that the thesis would have never been completed without the assistance of my colleagues and the congenial atmosphere within our group. I would like to specifically thank Hagen, Marc and Christian Zeitz for their shared expertise on the image processing techniques and the computational issues; Samuel for his support on the Labview programs; Anna-Lena for preparing 2D images of grain-velocities; Michael Jung, Carsten and Michael Hein for their fruitful suggestions in conducting the wettability tests and Stefan for his ample support in measuring the surface-roughness and friction of the bead materials. I am extremely fortunate to have Dr. Kamaljit

Singh as a great colleague and a good friend of mine; whose expertise on the tomographic image processing techniques has helped me to overcome some core issues. I also thank our collaborators, Dr. Ciro Semprebon and Dr. Martin Brinkmann from MPI-DS, Göttingen (Germany) for providing me the numerical results of the liquid bridges. For valuable inputs regarding 'Latex' issues, I specially thank Brindaban-da from Basel (Switzerland). I also thank Melanie for her support in preparing the 'Kurzzusammenfassung' section and Debajit for critical reading of two chapters of the thesis. It would be certainly unfair if I did not acknowledge Ms. Judith Rech, for her assistance with all kinds of administrative affairs. For technical assistance, I am also thankful to Mr. Schmitt and his team at the departmental workshop.

I am also grateful to my kith and kin for their constant moral supports and encouragement. I have really enjoyed the wonderful companies with all my Saarbrücken-friends - Sukhvinder, Joyee, Leonardo, Friederike, Dishant, Moumita, Kalyan, Rudolph, Gawas, Sasi, Aarthy and Venkat. Last but not least, I have no words in expressing my gratitude to my parents, Sefali Karmakar and the late Asit Karmakar, for their unconditional love to me. Without their endless support and silent sacrifices, I would never have reached at this stage. And finally, I thank Sri Ramakrishna Paramahansa for his continuous blessing towards my life.

Contents

1

Introduction

Granular materials like sugar, rice or any kind of grain are very common in our everyday life and have potential importance in many industries such as food processing, pharmaceuticals, oil and gas industries. In present days, globally more than half of the raw materials come in the form of granular matter [1]. Even though the granular materials seem to be very simple, their unique physical properties often differ from that of other conventional states of matter [2–10]. As early as in the eighteenth century, scientists, mostly from an applied engineering aspect, had started to explore the complexity and richness of granular materials. In the last two decades, the field of granular media has become enormously enriched with contributions made by different scientific communities, like physicists or geo-scientists.

As an example, one may consider dry sand which behaves as fluid (seen in **fig. 1.1**a) while it gently runs through the orifice of an hourglass or forms dunes in the desert under the influence of wind. This quasi-fluidity is obviously due to the fact that there is no virtual attractive force

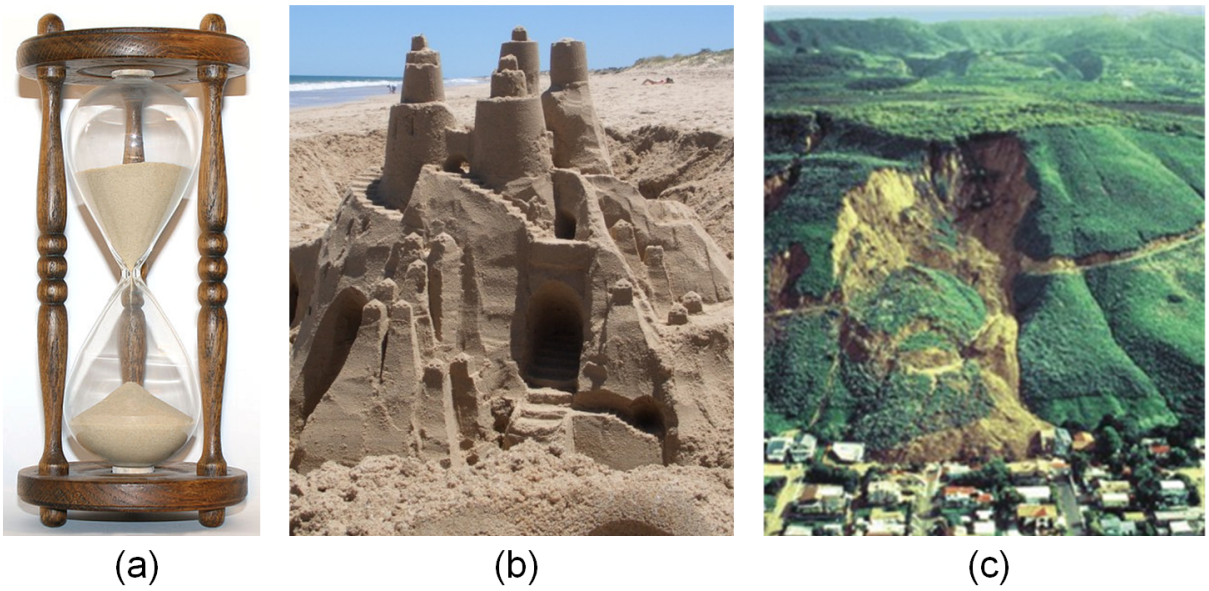

FIGURE 1.1: a) Dry sand flows through the orifice of an hour glass; which depicts its quasi-fluid behaviour (image copyright: S. Sepp, commons.wikimedia.org [11]). b) A sandcastle, constructed with wet sand at Preston Beach (Australia) demonstrates its increased mechanical stability (image courtesy: Petra Weiss, Germany [12]). c) Initiated by heavy rainfall, a massive landslide occurred at La Conchita, California (USA) displays the liquefaction of wet soil-grains (image copyright: Robert L. Schuster, US Geological Survey, USA [13]).

acting between the individual sand grains. In contrast to this illustration, if a small amount of any wetting fluid is added to a dry sand assembly, its mechanical stability dramatically increases; the liquid transforms dry sand to a moldable material. With potential skills and imaginative power, one might even sculpture a sandcastle - only using dry sand and water as ingredients. However, nobody needs a precise knowledge of liquid volumes to be added for building such a sandcastle. In **fig. 1.1**b, a sandcastle constructed at Preston Beach (Australia) demonstrates the increased mechanical strength of wet sand piles. However, an excessive amount of liquid volumes can surprisingly change the mechanical stability of a wet granular assembly. The best examples of such instances are the catastrophic natural hazards, such as landslides or avalanches which often cause extensive property damage or even the loss of lives in mountain areas. The landslides are often observed to be initiated after considerable rainfall to those hilly regions. Any prediction of the landslide-occurrence requires a deep understanding of the wet granular media in many aspects.

In the past decades, there have been enormous studies carried out to understand and predict

the underlying physics of these natural phenomena. For the prediction of landslide-occurrence, the analytic methods or safety factors are mostly calculated based on the empirical correlation between the soil-moisture condition (which straightforwardly depends on the rainfall) and its local stress fields [14–16]. Despite all these challenging efforts made so far, our knowledge is still obscure.Therefore, the study of wet granulates is of extreme importance for diverse fields, from 'soil-mechanics' to 'natural-disaster-management'. In this context, we may consider a rainfall-induced massive landslide which occurred at La Conchita, California (USA) after heavy rains in March 1995. It is well visible in **fig. 1.1**c that the mobility of wet soil-grains has a massive downward movement. However, the deformation is locally concentrated to some regional parts where the velocity gradient is much higher than its adjacent parts. It is intuitively visible that the landslide has dislocated a portion of the road, built on the mountain. Although some individual wet soil blocks are apparently observed, the deformation shape is very similar to the parabolic profile. It is also tempting to suspect that the flow behaviour of wet soil-grains is very similar to that of a viscous fluid.This phenomenon raises an important question of concern: what instigates the liquefaction of wet granulates by lowering its mechanical strength ? Therefore, the main focus of my research work is to understand the mechanical stability of various wet granulates subject to the granular-flows.

A guide to the following chapters is as follows. In **chapter 2**, we begin with the theoretical description of wet granulates and subsequently, a brief experimental overview of the wet granular media is presented. In **chapter 3**, various surface properties of different granular materials, to be used for our experimental studies, are characterized. In **chapter 4**, the mechanical properties (namely, the tensile strength and shear stiffness) of wet granular assemblies are discussed in details. In order to explain the mechanical findings, the shear dynamics of wet granulates investigated *in-situ* with X-ray microtomography are discussed in **chapter 5**. In conclusion, **chapter 6** combines a short summary of our different experimental investigations.

2

Physics of Wet Granulates

2.1 Theoretical background

Within a wet granular assembly, the relevant forces which could be responsible for an attractive cohesion between the granules have to be discussed first. For any granular media, one might think of the van-der-Waals force, to be pertinent due to particle-particle interactions. However, the van-der-Waals force becomes important only when the particle radius (R) is much lower than 40 μm [17]. It should be mentioned that an assembly of smaller particles for $R \leq 40$ μm is considered as powder. The smallest bead radius (R) used in our experiments is about 70 μm. Therefore, any contribution owing to the van-der-Waals force can surely be neglected. Secondly, the electrostatic influences can certainly be ruled out [18], since water (being electrically conductive) is used as fluid phase for preparing the wet granular samples. Moreover, the gravitational influences only come into play if the dimension of a liquid domain is comparable to the capillary length of the

wetting fluid. The capillary length (κ^{-1}) of a liquid is a function of its surface tension (γ) and density (ϱ); which is correlated by the following expression [18]:

$$\kappa^{-1} = \sqrt{\frac{\gamma}{g\varrho}} \tag{2.1}$$

Here, g is the acceleration due to gravity. At room temperature, the capillary length (κ^{-1}) of water is roughly 2.7 mm whereas the length scale of a single liquid bridge typically lies well below the millimetre scale; this is because, the largest particle-dimension ($2R$) in all our experimental studies is within the range of a sub-millimetre scale. Hence, any gravitational influence on the liquid-shape can safely be disregarded. Therefore, the capillary bridge force is the dominating factor in determining the attractive cohesion within our wet granulates.

2.1.1 Wettability and capillary bridge force

Before starting an elaborate discussion on the capillary cohesion, the wettabilty of any material-surface needs to be introduced; which is quantified in terms of the contact angle (θ), an angle formed at the 'three-phase-contact' points by liquid volumes sitting on that particular material surface. According to Young and Dupré, if a material surface is wetted by a fluid, there exists an equilibrium contact angle (θ_{equi}). This sole and unique contact angle is to be obtained for an ideally smooth material surface i.e. no surface heterogeneities. It is quite well-known that for a completely wetting ($\theta = 0°$) case, the liquid fully spreads over the substrate whereas a perfect non-wetting ($\theta = 180°$) scenario occurs when the liquid does not wet the material-surface. However, in the context of real granulates, the grain-surfaces always deviate from perfect due to topographic surface defects and chemical heterogeneities. Even if one assumes that the particles are ideally smooth, the surface crevices may arise due to inelastic particle-particle collisions in experiments such as shear flow or granular fluidization [18]. Hence, the contact angle is experimentally found to be somewhere within the interval of two extreme limits, named as the advancing and receding contact angles. The advancing contact angle (θ_{adv}) is the maximum achievable contact angle while the liquid volume is advancing over a substrate and the receding contact angle (θ_{rec}) is the minimum contact angle, obtained for continuous withdrawn of the liquid volumes. The difference

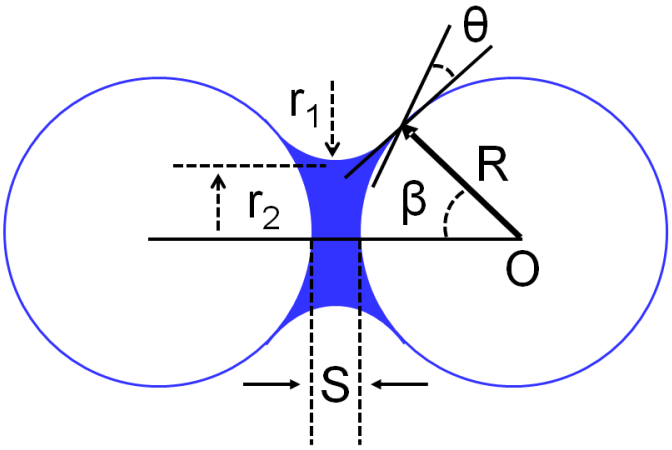

FIGURE 2.1: A stretched capillary bridge spanning between two equal sized spherical particles (R) at a finite surface separation (S).

between the advancing and receding contact angles is defined as the contact angle hysteresis, i.e. $\theta_{hys} = (\theta_{adv} - \theta_{rec})$. It is also known that an addition of tiny liquid volumes to dry granulates will create small liquid bridges between the adjacent granules. Since the surface tension (γ) of wetting liquid tries to minimize the free surface energy, the effective pressure difference between the liquid and its surrounding phases gives rise to the Laplace pressure (P_{Lap}) as expressed by the following relation [18]:

$$P_{Lap} = \left(\frac{1}{r_1} + \frac{1}{r_2}\right) \tag{2.2}$$

Here, r_1 and r_2 are called the principle radii of surface curvature. The mean radius of the surface curvature, also known as the Kelvin radius, is expressed by $r_K = \frac{1}{2}\left(\frac{1}{r_1} + \frac{1}{r_2}\right)$. **Fig. 2.1** schematically displays a capillary bridge existing between two ideally spherical particles (R) at a finite surface separation (S) and, β denotes the bridge angle.

In the past, there have been considerable progress to understand the capillary cohesion for added liquid volumes within various wet granulates. An overview of these different investigations could be found in ref. [7, 18, 19]. It has been recognized that the surface tension (γ) of wetting liquid and the particles' wettability have strong influences on the capillary bridge forces. Meanwhile, the basic physical understanding of bridge forces for ideally spherical bodies is quite well understood

and have become a part of the textbook knowledge [4, 20, 21]. For determining the capillary bridge force, most of the approaches and analytical calculations are derived by considering the toroidal approximation which gives a satisfactory result if the spherical particles, connected by a liquid bridge, rest at perfect contact. However, one of the most comprehensive studies presented by Willett *et al.* [22] describes the dependence of attractive capillary bridge force (F_{cb}) on the surface separation (S); in which, two equal sized spherical particles of radius R are considered to be connected by a capillary bridge of finite liquid volume (V_{cb}). Following their approximations, the attractive capillary bridge force (F_{cb}) as calculated for considerably small contact angles (θ) is given by the expression [18, 22]:

$$F_{cb} \approx \frac{2\pi R\gamma \cos\theta}{1 + 1.05S^{+} + 2.5(S^{+})^{2}} \tag{2.3}$$

Here, the rescaled surface separation (S^{+}) is expressed as follows:

$$S^{+} = S\sqrt{\frac{R}{V_{cb}}} \tag{2.4}$$

While the surface separation (S) gradually increases, the capillary bridge force (F_{cb}) decreases in accordance with the eq. (**2.3**). At a critical surface separation (S_c), the liquid bridge cannot sustain anymore and ruptures. The critical surface separation (S_c) is given by [18, 22]:

$$S_c' = \left(1 + \frac{\theta}{2}\right)\left(V_{cb}^{*(1/3)} + 0.1V_{cb}^{*(2/3)}\right) \tag{2.5}$$

where $S' = S_c/R$ and $V_{cb}^{*} = V_{cb}/R^3$ are the normalized surface separation and bridge volume respectively. The remarkable feature of the capillary bridge force is its hysteretic nature [18]: a liquid bridge ruptures at a finite surface separation between two neighboring particles; however, a liquid bridge can only be reformed while these two particles come into physical contact. From eq. (**2.3**), the attractive capillary bridge force, exerted by a liquid bridge between two ideally spherical particles at perfect contact, can simply be obtained as follows:

$$F_{cb} \approx 2\pi R\gamma \cos\theta \tag{2.6}$$

Moreover, the bridge force equation (**2.6**) which is independent of the bridge volume (V_{cb}) can effortlessly be shown as equal to the surface area of a spherical particle covered by the liquid phase, times the built up Laplace pressure (P_{Lap}) as long as the boundary condition: $r_2 \gg r_1$ is satisfied [18]. In this aspect, one may also consider that there is a liquid bridge between a spherical particle (R) and a flat substrate. Assuming θ and β to be negligibly small, the corresponding cohesive force (F_{bs}) at $S = 0$ can be obtained as follows [21, 23]:

$$F_{bs} \approx 4\pi R\gamma \cos\theta \tag{2.7}$$

Furthermore, it needs to be pointed out that for large liquid volumes and contact angles, the generalized bridge force expressions as mentioned above lose their validation. In this case, the normalized capillary bridge force, F^* ($= F_{cb}/2\pi R\gamma$) should be expressed by the following equation [22]:

$$\ln F^* \approx f_1 - f_2 \exp\left(f_3 \ln S^+ + f_4 \ln^2 S^+\right) \tag{2.8}$$

The constants, f_1, f_2, f_3 and f_4, depend on the effective contact angle (θ) and normalized bridge volume (V_{cb}^*) and their complex expressions could be found ref. [22]. It has to be addressed that the above eq. (**2.8**) is valid as long as θ and V_{cb}^* remain well below 50° and 0.10 respectively [22], else the errors to the estimated capillary bridge force mentioned would be considerably large.

2.1.2 Surface heterogeneity and capillary cohesion

Following the discussion of the previous section, it is clearly understood that the surface roughness and wettability of materials can strongly influence the attractive capillary cohesion within wet granulates. In the past, the correlation between the surface roughness and capillary forces has been

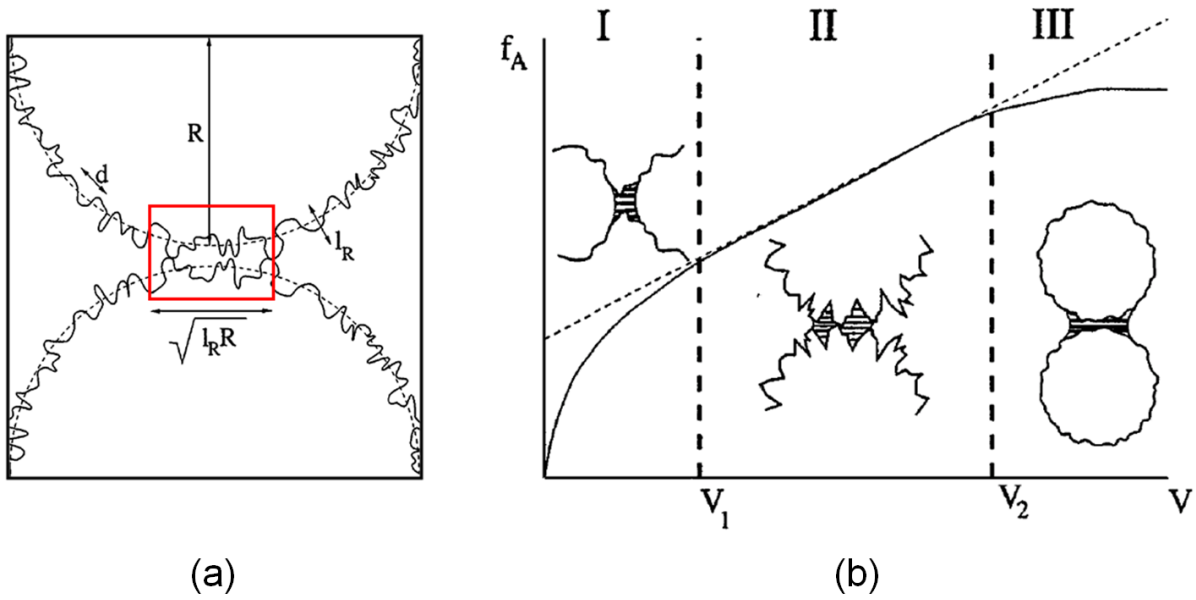

FIGURE 2.2: a) Schematic sketch displaying two rough spherical particles at a zero separation ($S = 0$). b) Dependence of adhesive force (f_A), exerted by a liquid contact, as a function of the added liquid volume (V). The dashed vertical lines distinguish three different regimes (I, II and III) which are named as the asperity, roughness and spherical regimes respectively. Images taken from ref. [28]

demonstrated by several authors [24–27]. An elaborate and compressive theoretical investigation of the capillary bridge force and its relation to the surface roughness has been presented by Halsey and Levine [28]. In their calculation, two spherical particles, having a finite degree of the surface roughness, are assumed to be connected by a liquid-contact of defined fluid volume (V). The surface roughness is additionally characterized by its roughness exponent (l_R) and lateral amplitude (d) where l_R and d are considered to be much smaller than the macroscopic particle radius (R). **Fig. 2.2**a schematically illustrates two rough spherical grains at physical contact. At the microscopic level, Halsey and Levine [28] have identified three different regimes of the capillary cohesion. In **fig. 2.2**b, the adhesive force (f_A), corresponding to these different regimes, is shown as a function of the liquid volumes (V) present at the particle-particle contact. Prior to forming a single capillary bridge, the particle-crevices must be filled with added liquid. For a very small amount of added liquid volumes, a cohesion would result due to accumulated liquid volumes, trapped around the asperities at which two neighbouring particles are in perfect contact. This physical picture is described by the so-called asperity regime (i.e. regime I) which holds as long as the liquid volume does not exceed $V_1 \approx d^2 l_R$. As a result of the increased liquid volume,

a transition occurs from the asperity regime to the roughness regime (i.e. regime II) in which the surface roughness statistically determines the attractive cohesion. In this roughness regime, the liquid volume is significantly large in compared to the asperity regime, but the microscopic particle radius (R) still does not contribute to the bridge force. The maximum threshold of the roughness regime is determined by the liquid volume $V_2 \approx Rl_R^2$. For considerably large liquid volumes, the surface-crevices are saturated by the liquid and consequently, a capillary bridge appears between these two rough spherical particles. In this case, the attractive capillary bridge force is determined by the macroscopic particle radius (R). However, the surface roughness no longer plays any role in determining the attractive bridge force for this saturated regime, named as the spherical regime i.e. regime III. Remarkably, the adhesive force (f_A) in the spherical regime becomes independent of liquid volumes present in that particular liquid bridge. This physical scenario leads to the validation of capillary bridge force eq. (**2.6**) as described in the earlier section.

2.2 Experimental overview of the wet granular media

The underlying physics of wet granular media cannot be described solely by the capillary bridge forces if the particles are in motion. Other pertinent effects, such as flow properties of liquids or the frictional forces between the adjacent grains, have greater importance to capture its peculiar mechanical responses. For the broader aspects of my thesis, the recent progress on the dynamical studies conducted for different wet granular systems - more specifically, in which the spherical microspheres are considered as model systems, are briefly discussed in the following sections. The potential knowledge would also help us to understand the mechanical findings of various wet granulates, to be presented in the later chapters.

2.2.1 Granular packing, jamming and liquid-contacts

The packing fraction (ρ) of a granular assembly, defined as a ratio of the grain-volume to the assembly-volume, is a relevant parameter used to quantify the granular compaction dynamics. For an assembly of randomly distributed monosized spheres, the maximum achievable packing fraction is the so-called 'random close packing' ≈ 0.64 [29, 30]. Another characteristic packing

fraction, namely the 'random loose packing' ≈ 0.55 [29] is the lower limit which is required to keep a granular pile mechanically stable. Beyond this 'random close packing' limit, a densest packing fraction (≈ 0.74) could be obtained only for a 'face centred cubic' (fcc) or a 'hexagonal close packed' geometry [29]. For the densest packing fraction, the compactified granular system is associated with the crystallization of spheres. It is well-known that a granular assembly, subjected to various mechanical perturbations like vibration, tapping or shear, becomes more and more compact until it reaches the maximum limit of its grain packing. In the last decades, the compaction dynamics for dry granulates has widely been explored under several confinements. A detailed description of these different investigations can be found in ref. [29, 31**?** –33]. With vertical tapping, Knight *et al.* [31] has extensively studied the compaction dynamics of dry granular assemblies. It has been reported in ref. [31] that the granular compaction dynamics exhibits a very slow relaxation and the final packing fraction is articulated to be around 0.66, relatively larger than the 'random close packing' fraction. To understand the correlation between the macroscopic compaction dynamics and microscopic grain rearrangement process, Pouliquen *et al.* [33] have investigated the compaction dynamics of monodisperse spherical glass beads by applying a periodic shear. Interestingly, the caging effect, very similar in molecular glasses, has been observed for such granular compaction study; the final packing fraction is found to be about 0.66. As early as in 1964, Scott *et al.* [34] had stated that if an assembly of monosized spherical particles is cyclically sheared, the packing fraction could be achieved well above 0.64. These experimental findings certainly point towards the structural ordering of grain packs. It should also be mentioned that for similar tapping experiments as Knight *et al.* [31] carried out by Philippe and Bideau [32], the final packing fraction is found to lie below 0.64; which suggests a disordered packing geometry. The granular materials, being out-of-equilibrium, might exhibit the memory effects. To find out the evidence for this analogy, Josserand *et al.* [35] has carried out the granular compaction experiments using a similar experimental setup as in Knight *et al.* [31]. In their studies [35], the evolution of packing fraction is found to strongly depend on the initial bead packing and on the sample's history as well. More recently, the compaction dynamics of different wet granular samples, prepared with monodisperse glass beads and various kind of wetting liquids, has been investigated by Fiscina *et al.* [36] with tapping conditions. In their studies [36], the packing fraction of spherical beads is observed to increase non-linearly as

a function of the tapping events. In addition, the surface tension of the test liquid has been mentioned to strongly influence the compaction dynamics: the higher the surface tension, the lower is the bead packing.

For the need of better understanding of contact networks inside dry and wet granulates, the packing fraction of spherical bead assemblies is independently investigated by T. Aste [37, 38] and M. Scheel [39] with X-ray tomography. For a typical packing fraction, ranging between 0.58 and 0.64, the 'number of neighbours in contact' in dry granulates, composed of monodisperse acrylic spheres, is found to vary between 5.5 and 7 (see **fig. 5** in ref. [38]). In case of wet granules, prepared with monodisperse glass beads and highly concentrated ZnI_2 solutions (used to distinguish different phases from each other), the 'number of capillary bridges on a spherical bead' at $W = 0.01$ is obtained to lie between 5.3 and 7.5 over a wide scale of the packing fraction, i.e. $\rho \approx 0.52 - 0.61$ (see **fig. 4.5** in ref. [39]). It should be mentioned that 12 'neighbours in contact' may even be found for a compactified granular assembly [37, 40]. In both granular systems, the bead-contacts are observed to be linearly affected by the packing fraction of spherical beads. The higher the packing fraction, the larger is the number of sphere contacts or capillary bridges. Moreover, for very similar bead packings, a higher number of contacts results inside wet bead assemblies as compared to dry bead packs. This characteristic phenomenon is not very surprising because a liquid bridge, namely a contact network between two neighbouring beads, may even exist for a finite surface separation (S) between the adjacent granulates. From tomographic studies [39] of wet granulates, a higher number of capillary bridges on a spherical bead (≈ 7.3) is obtained with a largest bead packing of $\rho \approx 0.61$, as compared to the experimental results mentioned in ref. [24].

A disordered system, such as a colloidal suspension of particles, dry powder or granulates, may caught into a small region of the phase space over which the particles have no further possibility to escape out [41–44]. This phenomenon, described as the jamming state, can only be unjammed if a finite external energy is applied upon. A number of control parameters, such as temperature (T), packing fraction (ρ) and yield stress (σ_{yield}), are used to describe the jamming behaviour. A few speculative jamming phase diagrams can be found in ref. [19, 41–43]. For a dry granular system, composed of frictionless monodisperse particles, the jamming transition is articulated to occur at a critical bead packing of $\rho \approx 0.639$ [43]. In a wet granular media,

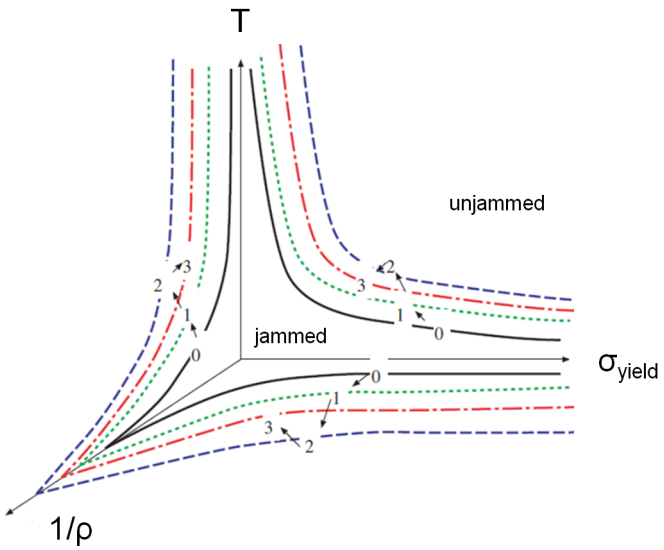

FIGURE 2.3: For dry and wet granular materials, a speculative jamming phase diagram as proposed in ref. [19]. These different curves, labelled with 0, 1, 2 and 3 are due to dry and various wet granular assemblies, distinguished by their liquid contents.

the 'jamming' transition may get affected by the liquid-contacts, present between the adjacent grains. Consequently, the jamming could eventually influence the mechanical properties of wet granulates. A possible jamming phase diagram of different granular systems as proposed in ref. [19] is displayed in **fig. 2.3**. The black curve labelled with '0' represents a non-cohesive dry granular media. An interesting feature of the jamming phase boundaries is the intersecting point on the $(\frac{1}{\rho})$ axis. This intersecting point describes the onset of jamming transition, to be achieved for a threshold packing fraction at $T = 0$ and $\sigma_{yield} = 0$ planes [42]. Other curves which are labelled with '1', '2' and '3' are due to very small liquid content, an optimal liquid content at which the cohesive force is maximum and sufficiently large liquid content while the cohesion is reduced from its maximum value respectively. Furthermore, the jamming phase diagram attains the largest jammed space at a threshold liquid content (W) for which the maximum cohesive stress is obtained. Remarkably, this phase diagram demonstrates that the jamming transition could be modified upon varying the liquid content (W) of wet granulates. More specifically, a wet granular system in comparison with its dry assembly may get into the 'jammed' state even at a lower packing fraction.

With the potential knowledge gained in **section 2.1.2**, it is intuitively understood that a fully

developed liquid bridge between two rough spherical particles can only be formed once the surface-irregularities of granular particles are completely saturated with liquid. Therefore, the number of fully developed liquid bridges on a spherical bead (N_b) within an ideal wet bead assembly should be equal to the total physical contacts of this particular bead to its nearest neighbours. In a frictionless isostatic system, N_b is estimated to be six [45]. However, N_b is experimentally found to depend on the local bead packing and is expressed as follows [24]:

$$N_b = N_0 + f\left(\frac{S}{R}\right) \tag{2.9}$$

Here, N_0 results for perfect contacts of the central bead with its neighbours and $f\left(\frac{S}{R}\right)$ is a dimensionless function of the surface separation (S) and bead radius (R). The existence of $f\left(\frac{S}{R}\right)$ is quite expected, because a capillary bridge may exist even if there is a certain gap between two neighbouring beads. It has been articulated that a stable capillary bridge cannot sustain for a maximum surface separation (S), larger than the critical separation S_c [22]. By detecting liquid bridges with optical microscopy, the dependence of N_b on the liquid content (W) and packing fraction (ρ) are studied by Kohonen *et al.* [24] for a model system of wet granular materials. It is found in their experiments [24] that N_b (W) of densely packed ($\rho \approx 0.62$) wet granular systems is about 10% higher than that of loosely packed ($\rho \approx 0.57$) wet granular systems. For a loosely or densely packed wet granular samples at $W = 0.02$, N_b is obtained to be ≈ 6 or 6.5 respectively. These values are significantly small as compared to the results of Clark and Mason [46, 47] who predicted that N_b should lie between 9 and 10 for similar liquid contents of $W \approx 0.01 - 0.04$.

Despite the progress made so far, our knowledge of the liquid contacts inside wet granulates is still limited. In the recent past, M. Scheel [39, 48, 49] has experimentally studied the liquid distribution within wet glass granulates with X-ray microtomography technique. In **fig. 2.4**, the number of fully developed capillary bridges on a bead (N_b), the number of liquid clusters on a bead (N_c) and the normalized liquid volume of largest liquid structure are plotted as a function of the liquid content (W). A liquid cluster is defined as a distinct liquid domain, connected to three or more beads. From these experimental studies [39], a fully developed capillary bridge is found to exist above a certain liquid content $W_0 \approx (6 \pm 2) \times 10^{-4}$, which readily demonstrates

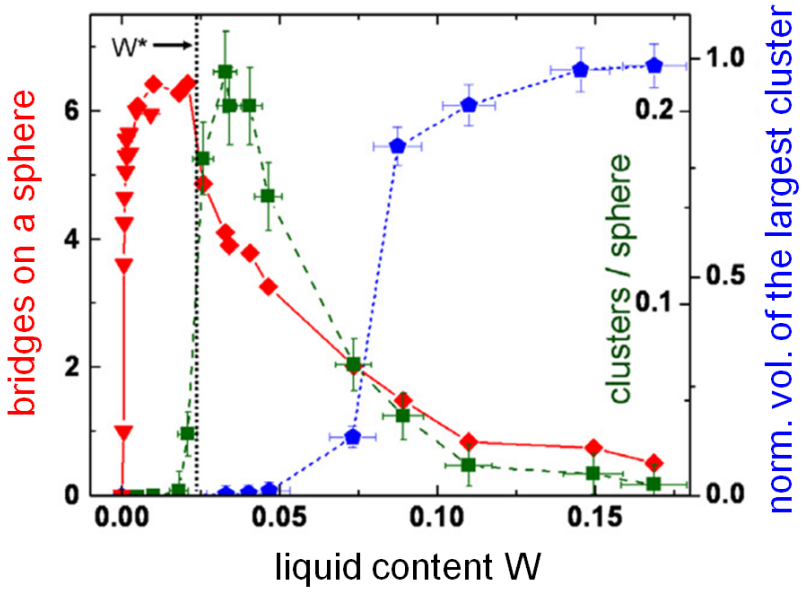

FIGURE 2.4: Number of liquid bridges on a glass bead (red symbols), number of liquid clusters on a glass bead (green symbols) and the normalized liquid volume of largest liquid clusters (blue symbols) displayed as a function of the liquid content (W). Graph taken from ref. [49].

that the corresponding liquid volume is required to saturate the microscopic crevices on the bead-surfaces. For gradually increasing liquid content, N_b sharply rises and reaches to a plateau (≈ 6.4) at about a liquid content of $W \approx 0.005$ until $W \approx 0.024$. As a result, individual liquid bridges grow in their sizes and start to coalesce at a characteristic liquid content of $W^* \approx 0.024$ [48, 49] and consequently, large liquid clusters appear within a wet bead pile. For any further increase of $W \geq W^*$, a sharp decay of N_b and N_c as seen in **fig. 2.4** results due to the fusion process of smaller liquid bridges and other liquid clusters. However, the average number of total liquid contacts on a bead is found to remain pretty much unaffected on the liquid content (W) scale. Furthermore, a percolation transition of the liquid morphologies is suggested to occur at a liquid content of $W_p \approx 0.08 - 0.11$ [25, 39, 48, 49]. At a considerably higher liquid content of $W \approx 0.17$ which is well above the percolation threshold, the largest liquid structure comprises around 95% of total liquid volumes, present in that particular wet glass granulates.

$$\frac{S}{V} = \frac{3\rho}{R(1-\rho)} \tag{2.10}$$

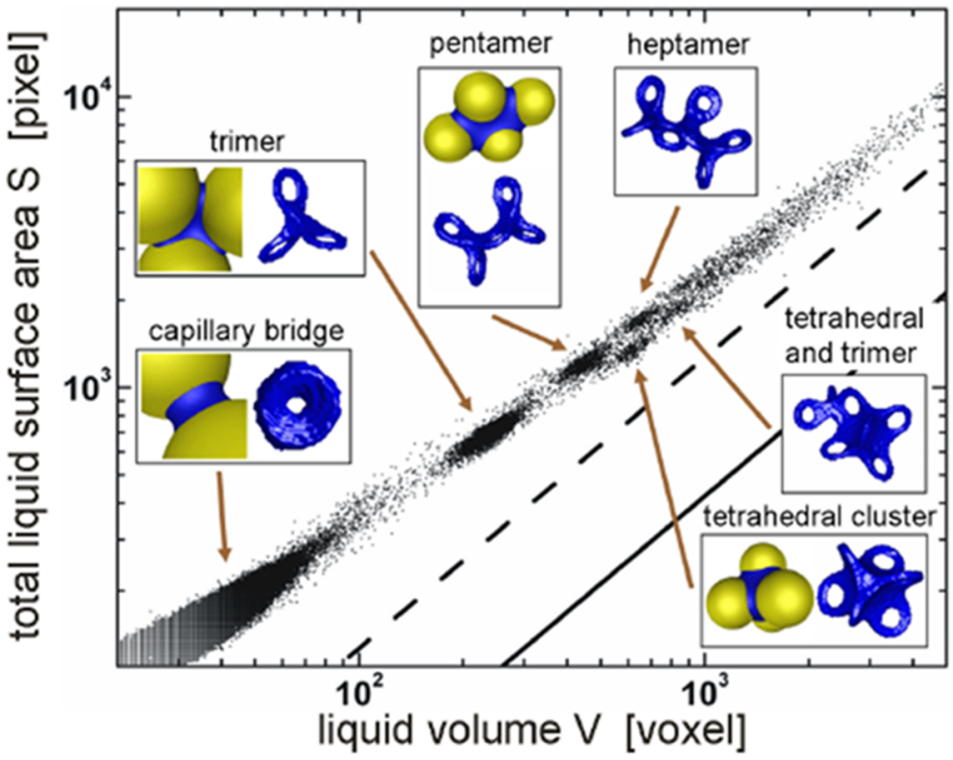

Figure 2.5: Surface-to-volume ratio for all liquid morphologies, emerging within a wet glass bead pile ($R \approx 140$ μm, $W = 0.035$). The insets reveal distinct liquid structures, independently obtained with X-ray microtomography and numerical studies. Image taken from ref. [49].

In **fig. 2.5**, the statistics of individual liquid morphologies obtained inside a wet glass bead ($R \approx 140$ μm) pack at a liquid content $W = 0.035$ is displayed by their total surface area (S) and liquid volume (V) [39, 48, 49]. Each data point in this graph presents a single liquid structure. At small V, the data cloud is due to isolated capillary bridges, and other liquid clusters are observed for large liquid volumes. The insets display different liquid morphologies, independently obtained with X-ray microtomography and numerical studies. An isolated capillary bridge is formed between two adjacent beads; a trimer is a distinct liquid domain which appears between three neighbouring beads; a pentamer is a liquid structure resulting from the fusion of five capillary bridges; a tetrahedral cluster geometry, having six wet contacts to its local bead configuration, is a distinct liquid domain formed between four neighbouring beads and a heptamer domain appears due to the fusion of seven capillary bridges. Remarkably, all data points are found to follow a single scaling curve. The solid line in **fig. 2.5** indicates the linear scaling behaviour as calculated by the expression (**2.10**) obtained for compact liquid morphologies [39, 48, 49]. It

physically demonstrates the smallest surface-to-volume ratio of liquid structures, to be resulted for a known bead packing (ρ) of monosized spherical particles (R). In **fig. 2.5**, the dashed line represents the surface-to-volume ratio of the largest liquid structure, obtained at $W = 0.11$. For this largest liquid cluster, the surface-to-volume ratio is around 2.9 times higher than that of a completely saturated wet bead pack; which certainly indicates that the wet granular assembly is governed by the open liquid morphologies.

2.2.2 Liquid equilibration within wet granular piles

In the spirit of research studies reported in ref. [18, 24, 25], the dynamics of emerging liquid morphologies within wettable glass bead assemblies is experimentally investigated with X-ray microtomography technique [39, 48, 49]. As a starting condition, a non-equilibrated liquid distribution is achieved by employing the vertical fluidization to a wet glass bead pile for a very short time. Right after stopping the fluidization, a time series of the tomograms are recorded with a finite time interval. Subsequently, the appeared liquid structures' volume distribution has been analysed as a function of the waiting time (t). **Fig. 2.6**a displays the histograms of distributed liquid volumes for a wet glass bead pack ($R \approx 280$ μm, $W = 0.02$) at different waiting times. Just after the fluidization is stopped, i.e. at $t = 0$, a continuous decaying curve indicates that the fluidization has completely destroyed all large liquid morphologies - by resulting a non-equilibrated liquid distribution. As the waiting time (t) increases, a volume re-distribution process between the individual liquid structures results the distribution curve at a time $t = 353$ s. With careful inspection, the distribution-peak is revealed to be caused for a particular type of liquid morphology: the isolated capillary bridge. At a large waiting time of $t = 1308$ s, no significant variation of the distribution is observed; which clearly demonstrates that the liquid redistribution process has already reached to an end. **Fig. 2.6**b presents the statistics of distinct bridge volumes, relaxing to an asymptotic value on the waiting time (t) [39, 49]. These tomographic results confirm the above mentioned volume-exchange mechanism, where the Laplace pressure (P_{Lap}) is the driving force of the liquid equilibration dynamics. The effective pressure difference between the individual liquid structures forces small liquid structures to receive the liquid volumes from the larger ones, and an equilibration is attained once the Laplace pressure becomes equal for all liquid structures.

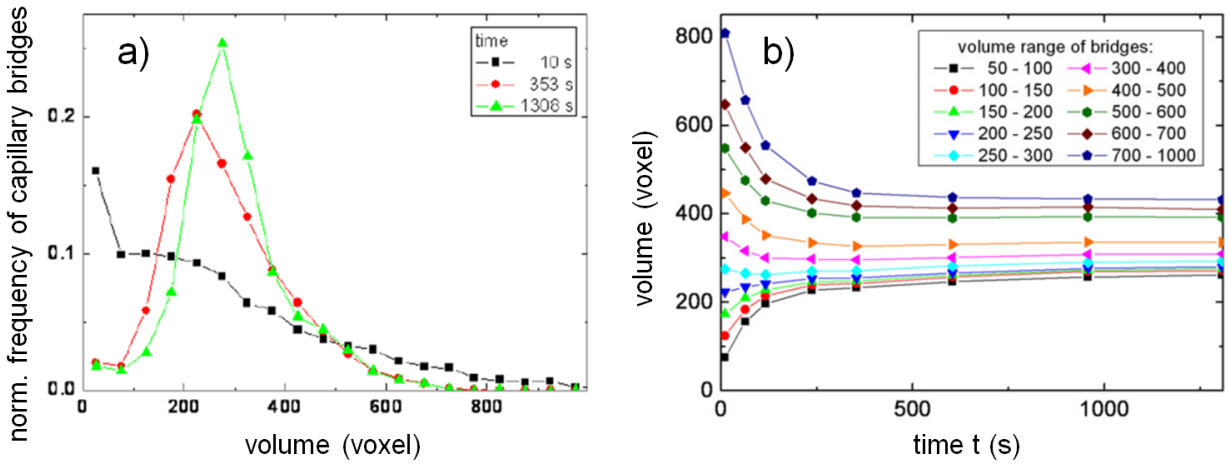

Figure 2.6: a) Histograms of distinct liquid volumes at different waiting times (t) - right after stopping the granular fluidization. b) Equilibration dynamics of individual liquid structures as a function of the waiting time (t). These results obtained for wettable glass granulates ($R \approx 280$ μm) at $W = 0.02$. Images taken from ref. [39].

The characteristic liquid equilibration time scale is found to be about 5 min [39, 48, 49].

For similar fluidization experiments, conducted with non-wettable basalt beads ($R \approx 280$ μm) at $W = 0.01$, the histograms [50] of emerging liquid volumes obtained at two different waiting times (t) are shown in **fig. 2.7**. At a time $t = 0$, a similar decaying distribution of the liquid structures is noticeable. However, this volume distribution curve, in contrast to the wettable glass granulate, does not vary with the increasing time - even after a large waiting time $t \approx 35$ min is elapsed. These experimental findings firmly indicate a non-existing liquid exchange mechanism for wet basalt bead assemblies. Furthermore, a direct comparison between these two wet granular systems, distinguished by their different wettability, suggests that the liquid redistribution process inside wettable glass bead packs is proceeding over the bead surfaces and not via the gas phase. Otherwise, a very similar liquid redistribution should occur for wet basalt bead piles as well.

In this context, it should be mentioned that the physical properties of various granular systems such as porous media are recognized to be extremely affected by the flow behaviour of liquid layers, adsorbed on the substrates [18, 51–54]. To identify such phenomena in 2-dimensional systems, Seemann *et al.* [51] has studied the equilibration dynamics of wetting layers on the substrates. In their experimental studies [51], the wave number (q) of film thickness modulation, the lateral

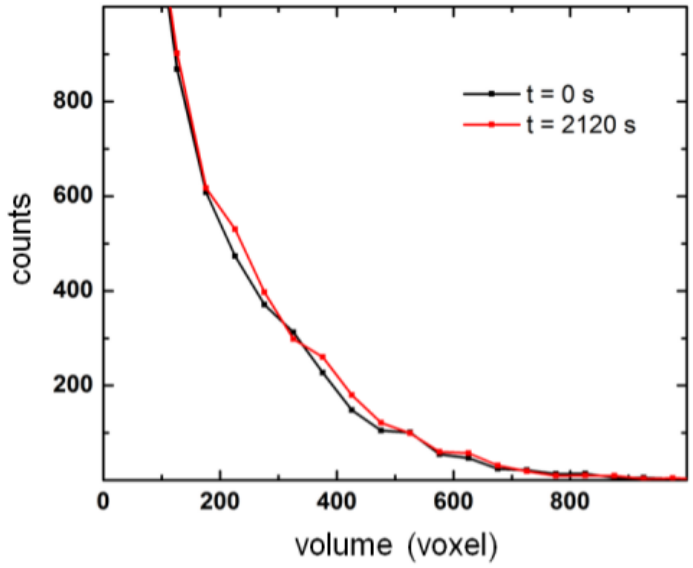

FIGURE 2.7: Histograms of emerging liquid volumes, resulted for wet basalt bead assembly ($R \approx 280$ μm, $W = 0.01$) at two different waiting times (t). Graph reproduced from ref. [50].

transport coefficient (a) and the liquid equilibration time (t_0) are found to be correlated by the following expression:

$$\frac{1}{t_0} = aq^2 = a\left(\frac{2\pi}{\lambda}\right)^2 \tag{2.11}$$

Here, λ is the lateral transport distance of the test liquid, flowing over the surfaces. It is furthermore articulated that the lateral transport coefficient (a) scales as ($1/\eta$) where η is the viscosity of the wetting fluid. For several simple liquids, like ethanol or propane, the lateral transport coefficient (a) is experimentally found to be in the order of 10^{-10} to 10^{-11} m^2/s [18, 51]. It has also been suggested that the laterally varying film thickness would considerably influence the transport mechanism if the lateral fluctuations on the surface topography are significantly smaller than one micron [51].

2.2.3 Granular fluidization

Over the past decades, the segregation phenomenon of dry granulates has been extensively investigated by means of shaking. The most prominent example of segregation process in granular mixtures is the '*brazil-nuts-effect*': when a container filled with mixed-nuts is shaken, larger brazil-nuts appear on the container-top. The size segregation dynamics of wet granulates, flowing down to an inclined plane, has been studied by Samadani and Kudrolli [55, 56]. For their experimental studies, wet granular samples are prepared with mixtures of bi-disperse spherical particles and various kind of wetting liquids, distinguished by their surface tension and viscosity. It is found that the segregation mechanism for a dry granular assembly is significantly reduced while the wetting liquid is added. The relative motion of individual particles is suppressed due to the presence of small liquid contacts between the adjacent grains. It is further observed that the segregation dynamics is greatly affected by the variation of liquid-viscosity and it completely vanishes for a large enough viscosity. Considering the liquid-lubrication, authors [55, 56] have estimated the viscous force for two moving spherical bodies, connected by a liquid bridge. It is revealed that for highly viscous liquids, the viscous force becomes comparable to the capillary bridge force. But, any viscous contribution is insignificant for liquids like water of low viscosity. Based on these calculations, it has been argued that the viscosity of test fluid must be taken into consideration in determining dynamical phenomena, such as particles' size-segregation. In this direction, the segregation dynamics has also been investigated by Geromichalos *et al.* [57] by employing horizontal vibrations to wet granulates which are prepared with spherical glass beads and ultra-pure water used as wetting liquid. Following their experimental findings [57], it has been claimed that three different liquid content regimes, named as the gaseous, intermediate and visco-plastic regimes would exist for the segregation dynamics: for increasing W, the size-segregation is observed to be enhanced in the gaseous regime; but it is suppressed in the intermediate regime, followed by no segregation in the visco-plastic regime.

Another classical scheme of granular fluidization is to apply vertical vibrations to a granular bed. For this technique, a container filled with a granular sample is vibrated using a shaker whose oscillation frequency (ω) and amplitude (A) can be well controlled. At a controlled frequency and for sufficiently high amplitudes, grains start to move in an irregular motion relative to its

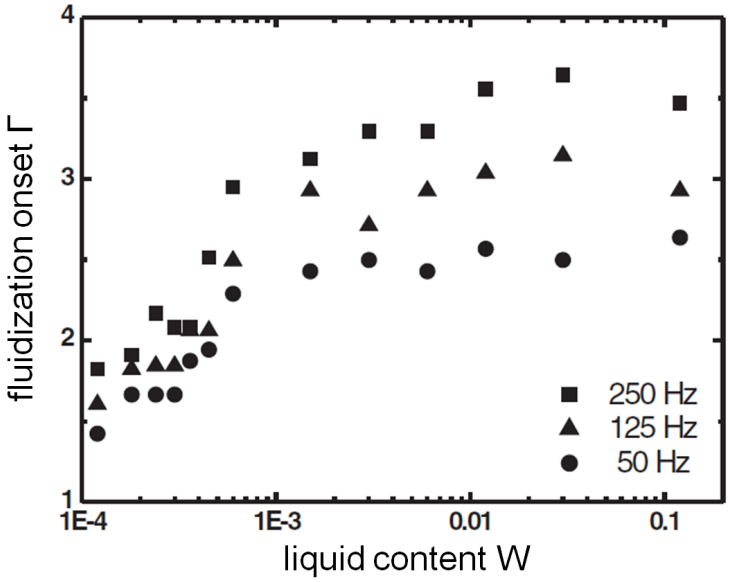

FIGURE 2.8: Dependence of granular fluidization onset (Γ) on the liquid content (W). The experimental results obtained for wettable glass granulates ($R \approx 140$ μm) at three different applied frequencies. Graph taken from ref. [25].

neighbours, accompanied by a convective flow within the sample container. This phenomenon is a manifestation of the granular fluidization. The fluidization onset parameter is characterized by a dimensionless number $\Gamma = (A\omega^2/g)$ [25] where g is the acceleration due to gravity. It is obvious that the fluidization can take place only if $A\omega^2$ is larger than g - namely, Γ must be greater than unity. Otherwise, the grains would remain at rest. With vertical vibration technique, the fluidization onset parameter is qualitatively investigated by Kohonen *et al.* [25] for a model wet granular system, prepared with spherical glass beads and controlled amount of test fluid. The fluidization onset parameter's dependence on the liquid content (W), obtained for the above mentioned wet glass bead samples at different applied frequencies, has been displayed in **fig. 2.8**. Interestingly, dry granulates are found to get fluidized at a threshold $\Gamma \approx 1.2$ [5, 25, 39]. It is also observed that Γ sharply rises for gradually increasing W and furthermore, Γ is found to stay almost constant for about two orders of magnitude on the liquid content scale above a critical liquid content W_0 which lies between 10^{-4} and 10^{-3} [18]. It is intuitively clear that the addition of liquid volumes to a dry bead pack introduces small liquid contacts between the neighbouring beads; which result in an attractive capillary bridge force. Therefore, Γ is certainly expected to be larger in wet granular systems. The gradual increase of Γ on the liquid content (W) is explained

in terms of distributed liquid bridges' growth dynamics and consequently, the effective capillary cohesion. The critical liquid content (W_0) is attributed to the liquid volumes, needed to fill the microscopic crevices on the rough bead-surfaces.

2.2.4 Shear flow and granular friction

In the past, there has been considerable attention given to understand the shear and tensile properties of different granular materials [18, 25, 39, 58–61]. The shear experiments are mostly performed either in a rotating drum or with a standard rheometer [58, 59]. It is recognized that the granular-flow behaviour, initiated by the shear stress, is quite different from an ordinary fluid-flow. In this aspect, Hartley *et al.* [60] using an annular geometry have studied the stress dynamics of slowly sheared dry granular systems, prepared of photoelastic disks or flat particles. It is pointed out in their studies [60] that two different time scales might exist for the stress relaxation dynamics: a very short time scale of about $(20 - 300)$ seconds and a much longer time scale in the order of few hours. The repetitive cyclic shear, applied to an assembly of monodisperse glass granules using a parallel plate shear cell geometry, can strongly influence the structural ordering of a granular pack [61]. Very recently, Mani *et al.* [62] have simulated the stress controlled periodic shear, applied to the wet granular media using two rough walls. They [62] have addressed that the liquid migration inside sheared wet granulates occurs due to the bridge-rupture events and consequently, the liquid redistribution process between neighbouring contacts. However, nearly all shearing techniques have some experimental difficulties. Mostly, the formation of shear cracks, fault zones or granular avalanches makes it rather difficult to maintain a homogeneous shear deformation [18].

It should be addressed that the particle-sizes can also influence the mechanical stability of wet granulates [18, 25, 39]. In this aspect, the tensile strength of a wet assembly, composed of monosized granular particles, can be estimated according to Rumpf's prediction model [63] given by the following expression:

$$\sigma_{Rumpf} \approx \frac{8}{9}\, k\, F_{bond} \approx \frac{8}{9}\frac{\rho}{\pi(2R)^2}\, k\, F_{cb} \tag{2.12}$$

Here, R, ρ, k and F_{bond} are the particle radius, packing fraction of grain assembly, grain coordination number and bonding force respectively. Since the effective bonding force (F_{bond}) between two neighbouring particles at perfect contact would simply be the capillary bridge force exerted by a liquid bridge, i.e. $F_{cb}\ (S=0) \approx 2\pi R\gamma\cos\theta$; the above eq. (**2.12**) indicates that σ_{Rumpf} inversely scales with R.

In practice, the sliding friction between two solid objects, intensively studied over the last centuries, is considerably reduced if any liquid is present between the solid bodies. This phenomenon is well known as 'liquid-lubrication'. A large number of research works on the subject of sliding friction and lubrication theory could be found in ref. [64]. The lubrication mechanism, be it either due to the film lubrication where the solid bodies are separated by a thin lubricant film, or for complete immersion of the solid bodies inside a lubricant fluid, are of potential interest to the wet granular media. However, our knowledge of frictional impacts on the wet granulates is still limited. In the recent past, the frictional dynamics of dry and wet granules, composed of smooth and spherical glass beads or rough sand grains, has been experimentally investigated by Géminard and co-workers [65–67] at low normal stress. For the dry case, experiments are conducted at a controlled relative humidity ($\approx 20\%$) to obtain reproducible results and consequently, the dynamic frictional coefficient (μ) is found to vary between 0.40 and 0.60. A somewhat similar finding with $\mu \approx 0.40$ for dry glass surfaces has earlier been articulated in ref. [20, 68]. In order to perform the experiment of wet case, the granular particles are initially immersed inside a water bath. Due to complete immersion, the stick-slip motion between the individual particles is diminished and a continuous sliding is observed. For submerged glass granulates, μ is obtained to be around 0.236 ± 0.004 [65]; which is significantly lower than that of dry granular particles at a relative humidity $\approx 20\%$. In order to understand the possible influences of liquid-viscosity on the lubrication dynamics, viscous force measurements are performed by S. Maenosono *et al.* [69] for sliding glass microspheres, confined in a thin liquid film, using pure water and water-glycerol mixtures as test fluids. From their experimental study, a reduced $\mu \approx 0.18$ is obtained. In this direction, Pitois *et al.* [70] have experimentally investigated the viscous contribution to the total attractive force that results for two moving spherical particles connected by a liquid bridge. Their experimental results [70] are claimed to be in good agreement with the lubrication theory.

To find out the comprehensive understanding of granular strength, the elastic shear modulus

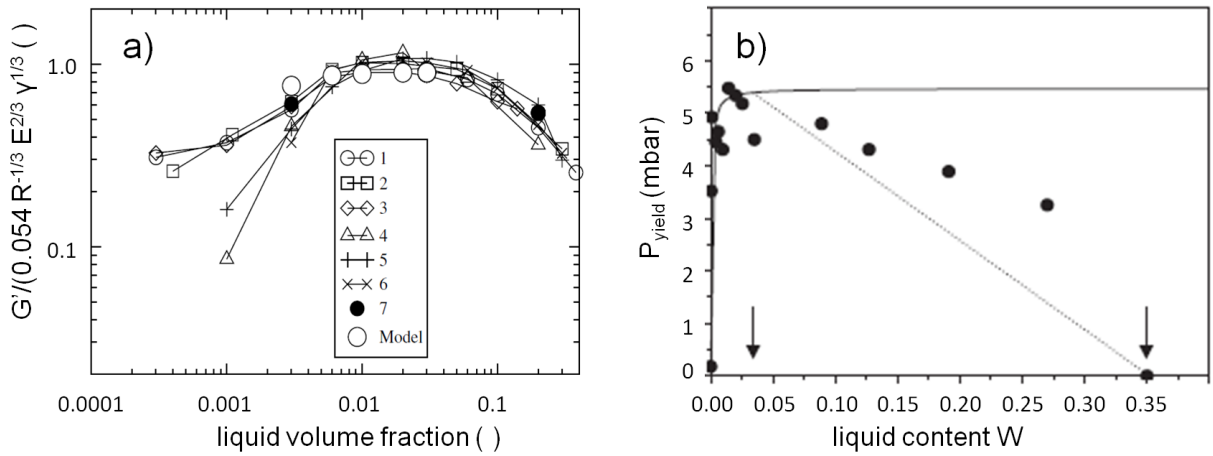

Figure 2.9: a) Rescaled elastic shear modulus (G′) of various wet granulates as a function of the liquid volume fraction. b) Yield pressure (P_{yield}) as a function of the liquid content (W) for wettable glass granulates. Images in a) and b) taken from ref. [58] and ref. [25] respectively.

(G') of partially saturated wet granulates has been investigated as a function of the liquid volume fraction (i.e. W) using a conventional rheometer [58]. For this experimental study, wet granular samples are prepared with various types of microspheres (glass beads, PMMA beads, polystyrene beads and sand grains) and two different wetting liquids (pure water and silicone oil). **Fig. 2.9**a displays the dependence of rescaled shear moduli (G') on the liquid volume fraction, for different wet granulates. The rescaled shear modulus (G') is observed to be maximized at a liquid content of $W \approx 0.01 - 0.03$. It has been furthermore stated that the granular strength has a strong dependence on the elastic modulus of individual grains with a power law. More recently, the flow properties of compact granular assemblies near to the jamming transition are experimentally studied by Fiscina *et al.* [59] using a standard rheometer, i.e. a cup-plate geometry and a very similar experimental setup as described in ref. [25]. Their wet granular samples [59] are prepared with spherical glass or polystyrene beads, wetted by deionized water or silicon oil. It has been argued [59] that the adhesion between individual particles within wet granulates decreases the flow resistance and hence, the associated energy dissipation of sheared wet bead samples is considerably smaller than that of a completely dry bead pack.

In recent past, the shear dynamics of wet glass granulates under cyclic shear deformation is experimentally investigated using a custom-made shear cell setup [18, 24, 25]. The differential

pressure, recorded *in-situ* during continuous shearing, shows a strong hysteresis loop caused by the granular-stress. From this hysteresis curve, the half of the opening-gap at zero shear is defined as the yield pressure (P_{yield}) and it has been studied by controlling various system parameters, like liquid content and shear speed. For spherical glass granulates wetted by pure water, the yield pressure (P_{yield}) obtained as a function of the liquid content (W) is shown in **fig. 2.9**b [25]. As one can observe, the characteristic behaviour of P_{yield} on the liquid content $W \lesssim 0.10$ is very similar to the fluidization-results shown earlier in **fig. 2.8**. For gradually increasing W, P_{yield} sharply rises to a plateau from its initial value at $W = 0$, i.e. a dry bead sample and is almost unchanged over a wide scale of the liquid content. Due to large experimental scatters, one expects that the maximum yield pressure (P_{yield}) is attained at a liquid content (W), somewhere between 0.005 and 0.10. But, P_{yield} becomes weak for $W \gtrsim 0.10$ and this weakening tendency can be observed to continue for increasing W. Since the liquid-air interfaces are significantly reduced at considerably large W, the effective capillary cohesion and hence, P_{yield} is expected to be smaller than its optimum value. For a complete saturation i.e. $W \approx 0.40$, the liquid-air interface should disappear as the granular particles are completely immersed into the wetting liquid. Therefore, P_{yield} of wet glass granulates becomes as soft as it is found for completely dry glass granulates. For similar aspects, the shear stiffness of various wet granular systems, distinguished by their different wettability, has also been investigated by M. Scheel and M. Sipahi [39, 71] using a very similar shear cell as mentioned in ref. [18, 25]. Surprisingly, the shear stiffness of non-wettable basalt granulates is obtained to be higher than that of wettable glass granulates. It is presumably caused due to relatively higher bead-packings and liquid-contacts inside a wet basalt bead assembly. Moreover, the maximal shear stiffness is achieved at a liquid content $W \approx 0.05 - 0.15$. In contrast to the experimental findings in ref. [25], no velocity dependence of the shear stiffness is observed for wettable glass bead assemblies in their studies [39, 71].

3

Characterization of Surface Properties of Granular Materials

Spherical glass or basalt beads of different bead radii, ranges from $R = 70$ μm to 280 μm, are chosen for our experimental studies. In order to prevent the crystallization of grain packs, these microspheres purchased from Whitehouse Scientific Ltd. (UK) have a relative polydispersity of $\frac{\delta R}{R} = 0.10-0.12$. At the microscopic level, no surface is perfectly smooth; which could arise due to chemical heterogeneities of the materials and for manufacturing defects. Surface properties of the bead materials are investigated in the following sections. Prior to all microscopic measurements, received beads are cleaned according to the following protocol: first, the beads are transferred to a cleaned glass beaker containing sufficient amount of $Millipore$ water and thereafter, sonicated for about 5 min, followed by draining away water. Using ethanol instead of water, this cleaning step is subsequently performed two times. Afterwards, these beads are thoroughly washed with

Millipore water a few times and dried in a normal drying oven.

3.1 Measurements of roughness on the particle surfaces

The surface topography of cleaned glass/basalt beads is scanned with an **A**tomic **F**orce **M**icroscope (Bruker Scientific Instruments GmbH, Germany) in its tapping mode (TM). Measurements are typically carried out for a surface area of about $1\ \mu\text{m}^2$. **Fig. 3.1** displays the AFM scanned surface topographic images, obtained for glass and basalt microspheres of $R \approx 70\ \mu$m. For basalt beads, the 'root-mean-square' roughness amplitudes are found to be around four times smaller than that of glass beads. These experimental findings also suggest that a lesser amount of wetting fluid is indeed required to saturate the topographic surface-crevices of smoother basalt microspheres as compared to glass microspheres.

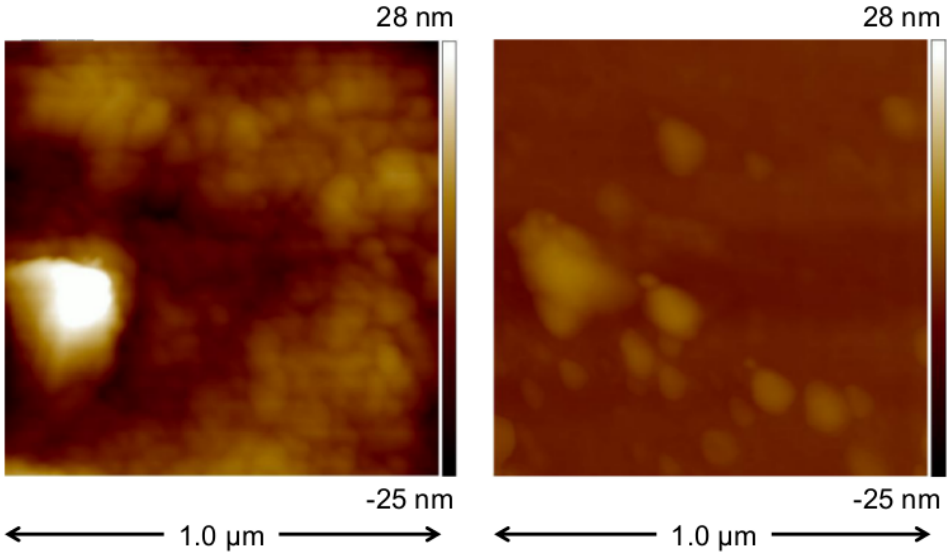

FIGURE 3.1: Surface topographic images of spherical glass (left) and basalt (right) beads ($R \approx 70$ μm). Basalt microspheres are observed to be much smoother in compared to glass granules.

3.2 Wettability study of glass surfaces

The contact angles of glass and basalt microspheres need to be experimentally quantified for obtaining the potential knowledge of their surface-wettability. As wetting liquids, we have used

FIGURE 3.2: Our experimental setup with **OCA20** instrument, used in measuring the contact angles of glass and basalt materials.

$Millipore$ water and a water-glycerol mixture ($70:30$ wt.%) having interfacial tension γ of 72 mN/m and 66.5 mN/m [72] and dynamic viscosity η of 0.89 mNs/m^2 and 2.12 mNs/m^2 [73] at room temperature. For almost wettable glass granulates with water as wetting liquid, the typical contact angle (θ) is found to be such that $\theta \in \{\theta_{rec}, \theta_{adv}\} \equiv \{5^\circ, 10^\circ\}$ [39, 48]. In the following, we measure the contact angles on a flat glass surface (assuming same wetting characteristics as of spherical glass beads) with a water-glycerol mixture ($70:30$ wt.%). Out of many experimental techniques, the widely acceptable sessile drop method is chosen, in which the injection or withdrawn of test fluid to a liquid droplet (≈ 0.7 μl), initially sitting on a horizontal flat glass surface, is subsequently conducted at a continuous flow rate of 0.03 μl/s. These steps are performed with a liquid injecting needle (made of stainless steel and having outer diameter of 0.5 mm) which is externally connected to a microliter Hamilton syringe (volume unit: 500 μl) mounted on the syringe pump of our contact angle measurement instrument: **OCA20**

(DataPhysics Instruments GmbH, Germany). The experimental setup used for this measurement purpose is shown in **fig. 3.2**. The available injecting needle, having its smallest outer diameter, is chosen so that the distortion of the drop shape can be kept as little as possible during volume expansion or contraction of the test liquid. Our experimental runs are captured by a video-recording system which consists of a CCD camera (768×576 pixel^2) mounted on a horizontal plane with a homogeneous back lighting. The video is recorded with an image acquisition rate of 5 frames/s. By analysing the optically captured 2D projection images with a commercially available image analysis toolkit, **Image Pro-Plus** (Media Cybernetics, Inc. USA), the contact angles are determined from the measured angles between tangents, drawn at the 'three-phase-contact' points. In **fig. 3.3** a & b, 2D cross-sectional images, taken from the advancing and receding contact angle measurements respectively, display the evolution dynamics of individual liquid droplets as the contact lines move on the flat glass surfaces; the experimental data are presented in **fig. 3.3**c. From all these experimental studies conducted with a water-glycerol mixture ($70 : 30$ wt.%) as test fluid, we find $\theta_{rec} \approx (18 \pm 5)^\circ$ and $\theta_{adv} \approx (36 \pm 4)^\circ$ respectively.

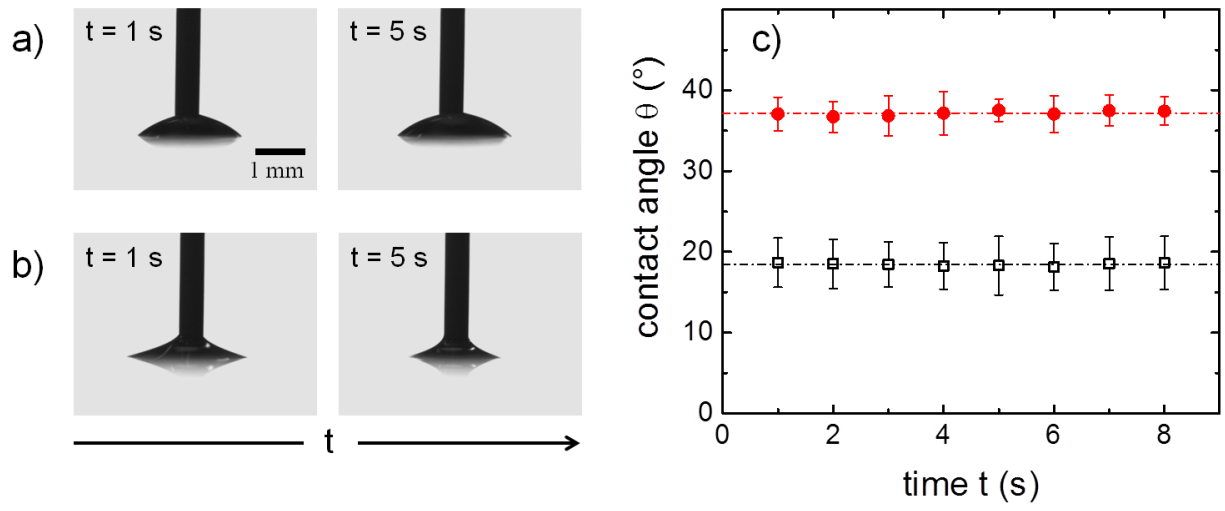

FIGURE 3.3: 2D projection images at two distinct times (t) show the movement of contact lines while the liquid volume a) advancing or b) receding on a flat glass surface. c) Advancing (filled circles) and receding (open squares) contact angles, measured on the flat glass surface with a water-glycerol mixture ($70 : 30$ wt.%) used as wetting fluid.

3.3 Wettability study of basalt surfaces

With above mentioned sessile drop method, researchers have also attempted to measure the contact angles on the structured and curved surfaces [74]. For these advanced measurements, a small liquid droplet is initially created at the apex of a structured or spherical surface. An addition or removal of controlled liquid volumes to the droplet allows one to measure the advancing and receding contact angles on that particular surface topography. In the spirit of their works [74], contact angles of spherical basalt beads using $Millipore$ water as test fluid are measured with the same measurement device, i.e. **OCA20**. In order to have an optimal experimental condition, the largest available basalt beads of $R \approx 1.1$ mm are chosen - by assuming same wetting characteristics as for small basalt microspheres. Our experiment is started by depositing a small water drop (≈ 1.0 μl) at the apex of a basalt sphere - by means of a liquid injecting needle. The deposited liquid drop's position is consequently adjusted to ensure that the liquid drop is symmetric about the central vertical axis. This adjustment is essential in order to maintain a homogeneous spreading condition while the test liquid would advance or recede over the curved surface. Following the adjustment, a maximal liquid volume of 1.7 μl is injected into this initial droplet with a continuous flow rate of 0.05 μl/s and subsequently, the liquid is withdrawn with the same flow rate. The maximum allowable liquid volume is chosen in such a way that the dimension of the liquid drop stays considerably below the capillary length of water. Therefore, we can safely disregard any influence due to gravity. The full experimental run, beginning from liquid advancing to liquid withdrawing on a spherical bead surface, is captured by the same video-recording system of **OCA20** instrument with an image acquisition rate of 25 frames/s. **Fig. 3.4** displays a series of 2-dimensional projection images at various times $t = 0$, 11 s, 34 s and 70 s; which visualizes the evolution of a liquid droplet while its volume is advancing or receding on the surface of a spherical basalt bead.

Following the schematic diagram as depicted in **fig. 3.5**a, the contact angles at 'three-phase-contact' points are determined from 2D projection images (analysed with the same software, **Image Pro-Plus**) - by assuming that R_1 and R_2 are the radii of spherical bead and liquid droplet, sitting on the top of this bead respectively; and H is the distance between their centres. By the given mathematical eq. (**3.1**), one straightforwardly obtains the contact angle (θ) attained

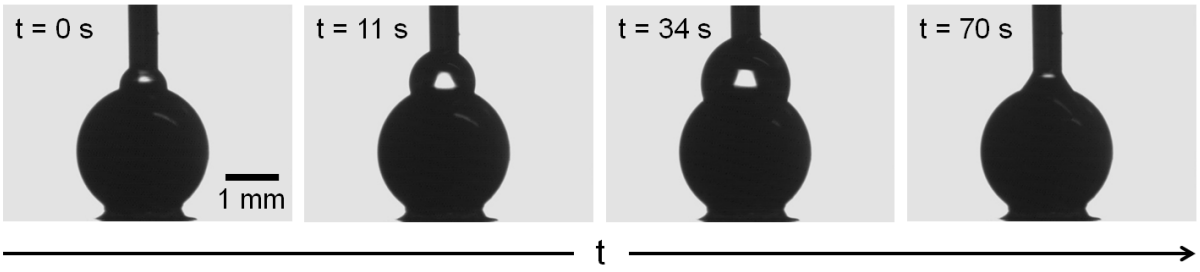

FIGURE 3.4: A sequence of 2D projection images, taken at various times (t) from a dynamic sessile drop experiment. These snapshots show the evolution of a liquid droplet as the liquid advances or recedes on a basalt sphere ($R \approx 1.1$ mm).

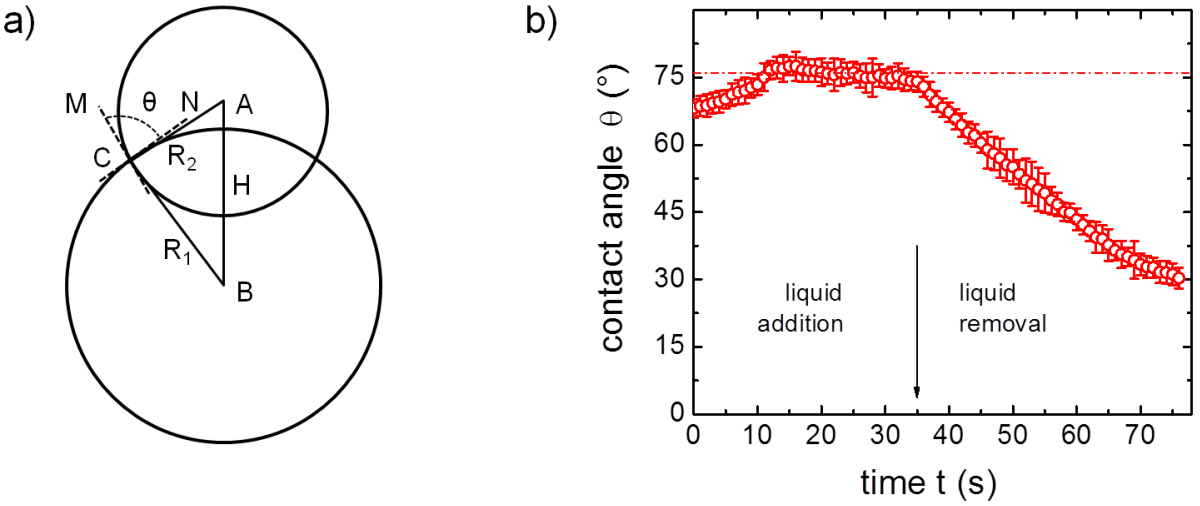

FIGURE 3.5: a) Schematic sketch to determine the contact angle (θ) at the 'three-phase-contact' point C of a liquid droplet sitting upon a spherical bead surface. b) With dynamic sessile drop technique, the measured contact angle as a function of the liquid injection/withdrawn time (t). The results are obtained for $Millipore$ water (used as liquid phase) which is advancing and subsequently contracting on a spherical basalt bead ($R \approx 1.1$ mm).

at the contact point C [75]:

$$\cos^2\theta = \frac{(R_1^2 + R_2^2 - H^2)}{4R_1^2R_2^2} \tag{3.1}$$

From a single image, the contact angle (θ) is achieved by averaging the individually determined contact angles of both image sides. In **fig. 3.5**b, the average contact angle is presented as a function of the liquid injection/withdrawn time (t). It is well observed that the contact angle

(θ) slowly increases from an initial value to a constant plateau, corresponding to the advancing contact angle (θ_{adv}) of basalt granulates. Once the advancing contact angle is reached, it does not noticeably change although the liquid volume still increases. This advancing contact angle plateau could be seen from $t = 11$ s to $t = 35$ s. With $Millipore$ water as test liquid, the advancing contact angle of basalt beads is obtained to be around $(76 \pm 4)^\circ$. Somewhat, very similar observations are addressed by M. Scheel and M. Schwamberger [39, 76]. M. Scheel has articulated that the advancing contact angle of basalt beads is about $(85 \pm 10)^\circ$ whereas M. Schwamberger has mentioned its value to be $\approx (74 \pm 4)^\circ$. Another plateau, corresponding to the receding contact angle (θ_{rec}) is also expected to reach while the liquid volume is withdrawing on the bead surface. However, such a plateau is not observed during continuous contraction of the liquid volume. Since we are dealing with very tiny amount of liquid volumes, the injection needle's wettability might have an undesirable influence to the liquid shapes - more specifically, while the liquid is retreating on the spherical bead surface. Presumably, this is why, we could not reach to the receding contact angle plateau for less-wettable basalt granulates.

Conceptually, the sessile drop technique is believed to be a simple experimental approach to measure the contact angles on any spherical surface. But, the major experimental challenges need to be addressed. (i) Instead of a horizontal flat surface, we have employed this dynamic sessile drop technique to a spherical bead surface whose dimension is in the range of a few millimetres; which itself imposes a great challenge to control the experiments. (ii) The second problem is the tendency of a liquid droplet to move off axis on the basalt beads' surfaces due to its non-wetting characteristic features. As the liquid volume dispenses in, it is more difficult to control the drop-spreading homogeneously on the spherical bead surface by maintaining the vertical symmetry. After deposing a liquid droplet on the bead surface, a drop shape readjustment is therefore required to be performed. In parallel, the distance between the needle tip and bead surface is also to be adjusted so that the symmetry-deviation can be kept at a tolerable minimum. It should be mentioned that many experimental attempts are carried out to achieve a single acceptable experimental run.

The liquid evaporation method has been employed to rule out the drawbacks of previous method in measuring the receding contact angles (θ_{rec}) of spherical basalt microspheres. For this experimental approach, a single bead layer of basalt microspheres is initially prepared on

a microscope slide and thereafter, the fluid phase (i.e. $Millipore$ water) using a microliter syringe is injected to the bead matrix for creating liquid bridges at the bead-contacts. The liquid, in a temperature controlled atmosphere, subsequently starts to evaporate as the time evolves. Hence, it initiates the movements of 'three-phase-contact' lines on the bead surfaces, by maintaining a certain contact angle. The temporal evolution of liquid-interfaces is captured with a **Zeiss AxioVert** microscope and a high speed camera, **Photron Fastcam** (Model: $SA3-120K$, resolution: 1024×1024 pixel^2) with a recording speed of 50 frames/s. The evolution dynamics,

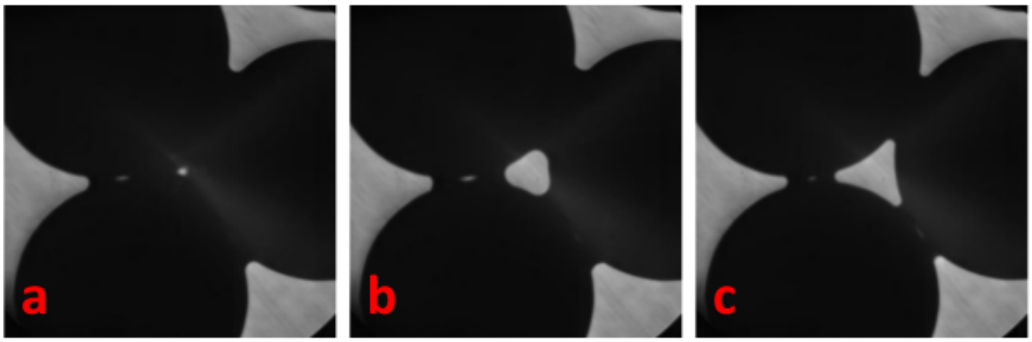

FIGURE 3.6: Evolution dynamics of individual liquid profiles, captured with liquid evaporation technique. a) A liquid domain, just before breaking into three liquid bridges, is connected to three individual basalt beads ($2R \approx 463$ μm). b) Right after breaking into three distinct liquid bridges at a time $t = 1$ s. c) Liquid shapes as seen at a later time $t = 5$ s.

resulted for a wet basalt bead layer ($2R \approx 463$ μm) is displayed in **fig. 3.6**. From these captured images, it is observed that a liquid domain, connected to three different basalt microspheres, breaks into three individual capillary bridges and their liquid volumes reduce with a stable contact angle (namely θ_{rec}) as the liquid evaporates. In **fig. 3.7**a, the receding contact angle (θ_{rec}) as a function of the liquid evaporation time (t) is shown for the same experimental run as in **fig. 3.6**. Within our experimental scatters, the receding contact angle (θ_{rec}) is obtained to be about $(30 \pm 5)^\circ$. It should be mentioned that each data point in this plot is generated by averaging all contact angles, measured for three distinct capillary bridges.

With this evaporation technique, the receding contact angle, obtained for different bead radii of the basalt microspheres are presented in **fig. 3.7**b. From these experimental findings, the receding

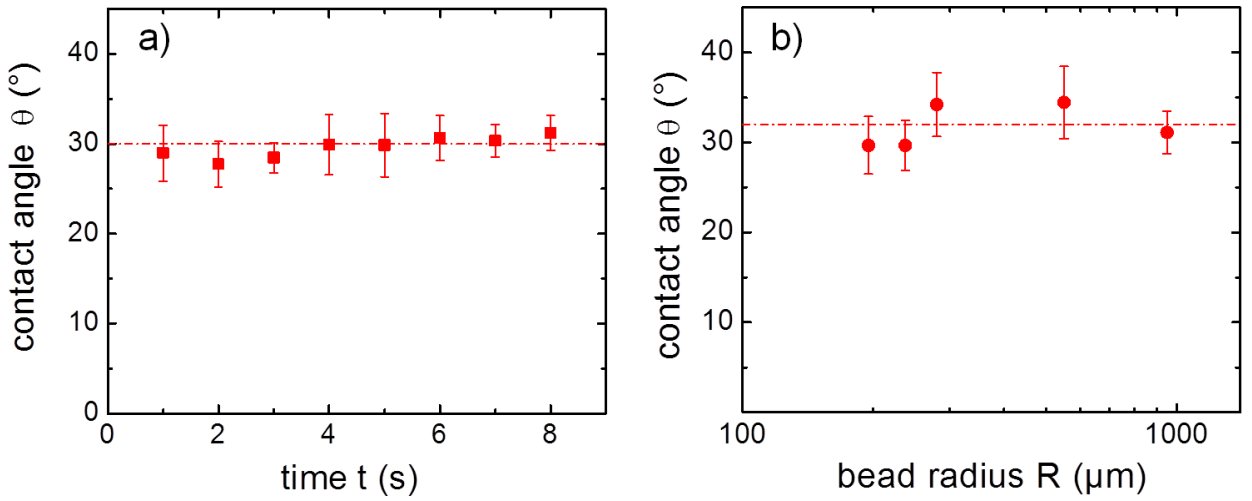

FIGURE 3.7: a) Contact angle (θ) plotted as a function of the liquid evaporation time (t), obtained for basalt beads ($2R \approx 463$ μm) with liquid evaporation technique. b) Measured contact angle (θ) as a function of the bead radius (R), from similar studies with different bead-sizes of the basalt microspheres. For all these experiments, $Millipore$ water is used as test liquid.

contact angle (θ_{rec}) of non-wetting basalt microspheres with $Millipore$ water as fluid phase is observed to be about $(32 \pm 6)^\circ$. For the discussion later on, we will accept this value as a reliable receding contact angle (θ_{rec}) of the basalt microspheres since (i) it is nearly constant over the broad spectrum of bead radius (R); so any influence which could arise due to different sample-batches or bead sizes, are over-ruled. (ii) Moreover, the liquid injecting needle's undesirable influences (as mentioned for the previous technique) can safely be disregarded. (iii) And, the liquid evaporation technique as compared to the sessile drop method allows a minimal rate of the volume-changes.

3.4 Measurements of friction coefficient for glass surfaces

It is fairly known from the textbook knowledge of solid-solid friction that an object of mass m, resting on an inclined plane, starts to slide under its own weight at a critical tilt angle (α) while the downward tangential force F_t ($= mg \sin\alpha$) overcomes the frictional force F_f ($= \mu mg \cos\alpha$); see the schematic representation in **fig. 3.8**a (top). By precisely measuring the critical tilt angle, one finds the sliding friction coefficient $\mu = (F_t/F_f) = \tan^{-1}\alpha$. The determination of the critical tilt angle is independent of loaded mass (m) and total surface area in physical contact.

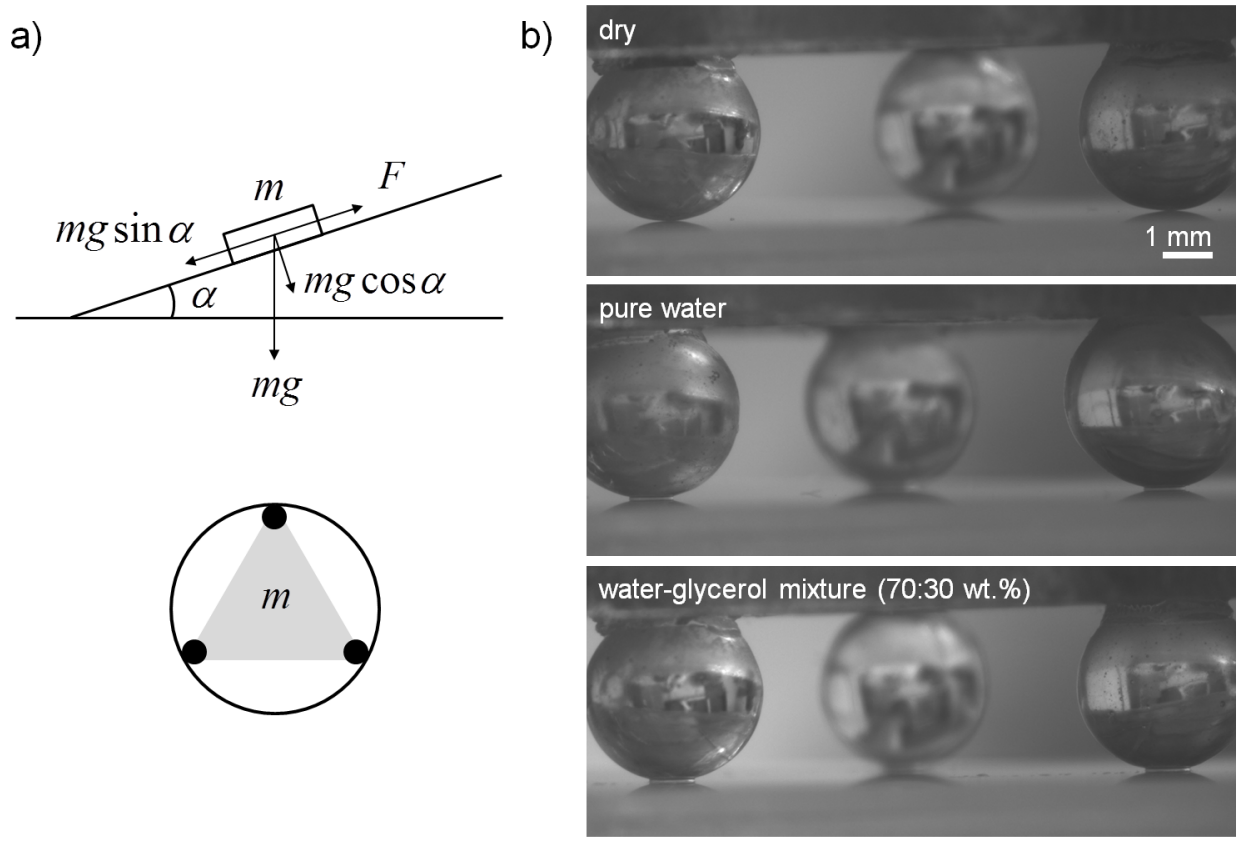

FIGURE 3.8: a) (top) Schematic illustration of a solid block residing on a tilted plane at an angle α. (bottom) Sketch of three spherical glass beads which are fixed at the centres of an equilateral triangle drawn upon a circular object of mass m. b) Images taken from the friction measurements, conducted for glass-on-glass surfaces - either dry or wetted by two distinct wetting liquids: $Millipore$ water and a water-glycerol mixture ($70:30$ wt.%).

Inspired by this simple idea, we attempt to experimentally quantify the sliding friction coefficient (μ) for glass-on-glass surfaces. At first, three glass spheres of diameter $2R \approx 3.76$ mm are glued at the centres of an equilateral triangle on a circular object of mass $m = 20.6$ g /35.6 g; see the schematic sketch in **fig. 3.8**a (bottom). Thereafter, the object is gently placed over a flat glass plate (dimension: $76 \times 26 \times 1$ mm^3) initially fixed on a horizontal plane. Following the positional adjustment, the tilt angle (α) between the glass plate and horizontal axis is gradually increased at a constant speed of 0.1 deg/s using the computer controlled motor of an Ellipsometer (Optrel Miltiskop, Optrel GbR, Germany). At some definite tilt angle, the beads slide over the inclined glass plate and consequently, the dynamic event allows us to determine the sliding friction coefficient (μ). The full experimental run is recorded with a high resolution (1392×1024 pixel^2)

CCD camera, Pixelfly-QE (from PCO AG, Germany) mounted on the same plane over which the glass plate is attached. For dry glass-on-glass surfaces (top image in **fig. 3.8**b) at room temperature, typically $(22.5 \pm 0.5)^{\circ}$C and relative air humidity, around $(30 \pm 4)\%$ we obtain the sliding friction coefficient $\mu \approx (0.29 \pm 0.05)$. At the microscopic label, the presence of adsorbed water molecules on the glass surfaces due to humidity effects can not be ruled out. Presumably this is why, a smaller dry friction coefficient is obtained as compared to the literature-values discussed in **section 2.2.4**.

In case of the wet-friction, three minute capillary bridges are initially created at the bead-plate contacts. As a result, there will be an attractive capillary cohesion. Therefore, the modified force equation of similar sliding dynamics can be rewritten as follows:

$$mg \sin\theta = \mu mg \cos\theta + F_{bs}^{tot} \tag{3.2}$$

Assuming a small contact angle θ, the total capillary force F_{bs}^{tot} $(= 3 \times 4\pi R\gamma \cos\theta)$ between the glass surfaces at zero separation $(S = 0)$ can be estimated from eq. (**2.7**) given in **section 2.1.1**. Using $Millipore$ water as test fluid, the frictional coefficient (μ) for glass-on-glass surfaces (middle image in **fig. 3.8**b) is measured about (0.25 ± 0.04), around 14% lower than that of completely dry glass surfaces. The formation of small water bridges ensures the existence of thin liquid films on the glass surfaces at their mutual contacts; hence, the liquid-lubrication dynamics is expected to diminish the frictional impacts between glass surfaces. For similar study with a relatively high viscous fluid, a water-glycerol mixture $(70 : 30$ wt.%), we observe a further reduction of the friction coefficient where $\mu \approx (0.23 \pm 0.04)$ is obtained; see the bottom image in **fig. 3.8**b. It indicates that the viscosity of wetting fluid has an additional influence to the wet-friction between the sliding glass surfaces.

4

Characterization of Mechanical Properties of Granular Assemblies

4.1 Experimental setups and techniques

4.1.1 Determination of the tensile strength

Using a simple centrifuge setup [39, 49], the tensile strength (σ_t) of a wet granular assembly can be quantified as follows: wet granulates contained in a cylindrical tube is rotating at an angular frequency (ω) around a fixed vertical axis of a centrifuge; see **fig. 4.1**a (top). For gradually increasing angular frequency (ω), the intensified centrifugal force within this wet granular pile gives rise to the tensile strength. At a critical frequency (ω_c), the centrifugal force (F_{centri}) exceeds the total tensile force ($F_{tensile}$) plus the frictional force (F_{fric}) of wet granules at the

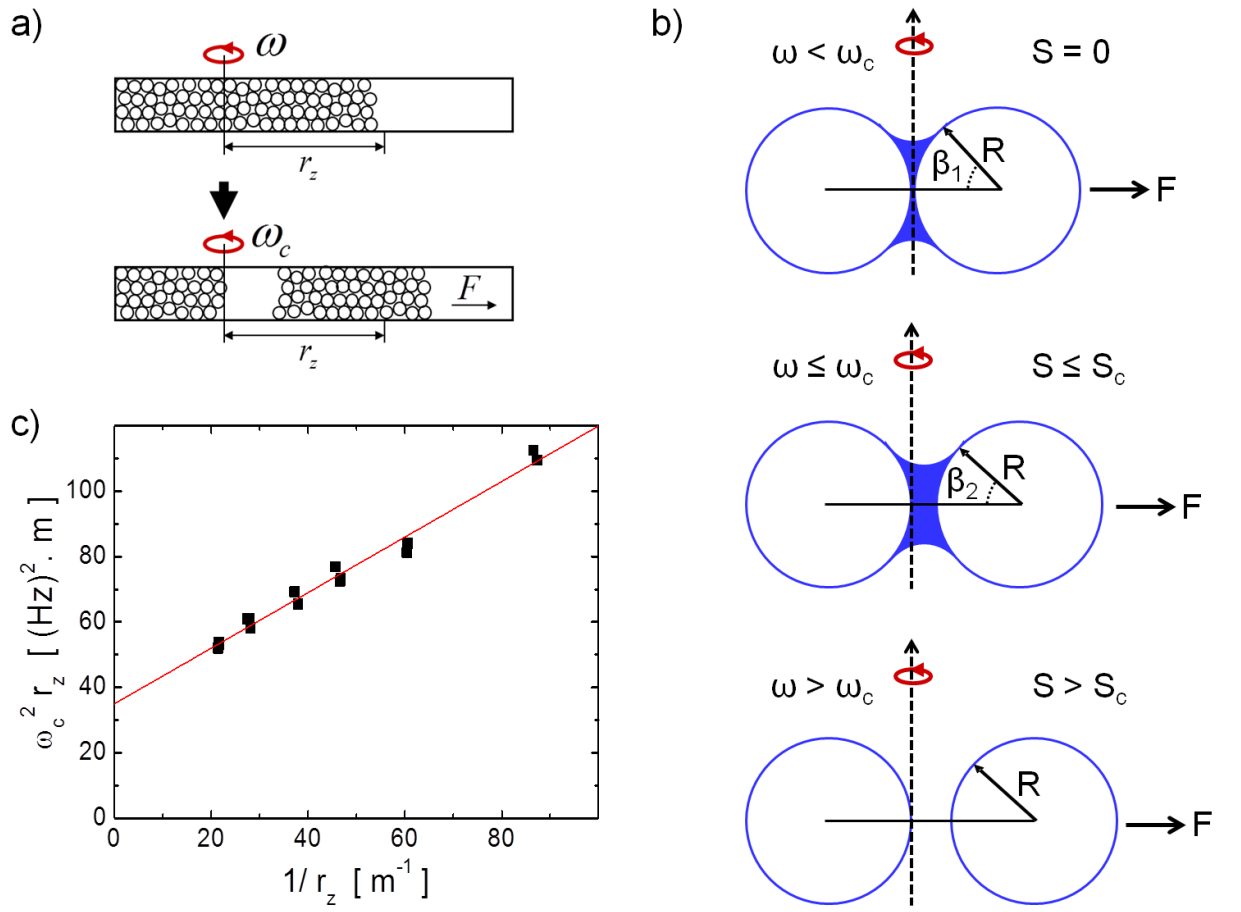

FIGURE 4.1: a) Schematic sketch for measuring the tensile strength with a centrifuge setup: a cylindrical tube filled with test granulates rotates at an angular frequency (ω) and the granular column ruptures at a critical angular frequency ($\omega \approx \omega_c$). b) Schematic diagrams illustrating, how a liquid bridge existing between two identical spheres of radius R is being ruptured at a critical angular frequency. c) Dependence of ($\omega_c^2 r_z$) on the ($1/r_z$) axis as obtained for wet glass granulates ($R \approx 70$ μm, $W = 0.05$).

tube-surfaces and consequently, the wet granular pile ruptures; see **fig. 4.1**a (bottom). Hence, the corresponding 'force balance' expression can be written as:

$$F_{centri} = F_{tensile} + F_{fric} \tag{4.1}$$

At the critical angular frequency (ω_c), the effective centrifugal force can be estimated as $F_{centri} = \int_0^{r_z} \rho_s A \omega_c^2 x dx = (\rho_s A \omega_c^2 r_z^2)/2$, where $\rho_s = (\rho \times \rho_m)$ is the packing fraction times the mass density of granulates. The parameter $A = \pi r'^2$ is the cross-sectional area of the cylindrical tube with r' as its inner radius and r_z is termed as the 'granular column length'. The associated

tensile force is given by $F_{tensile} = A\sigma_t$ i.e. the cylindrical tube's cross-sectional area (A) times the tensile strength (σ_t) of wet granulates. The frictional force F_{fric} is given by the following expression:

$$F_{fric} = \mu\rho_{2d}O_s F_{cb-wall} \tag{4.2}$$

For a hexagonal close-packing geometry, 2-dimensional density (ρ_{2d}) of liquid bridges, formed between the tube-surfaces and the granulates, is estimated to be about $\left(\frac{0.29}{R^2}\right)$ [25]. The term μ is the friction coefficient for granulates on the tube-surfaces. Considering the eq. (**2.7**), the 'bridge wall' force ($F_{cb-wall}$) at $S = 0$ can be approximated as $F_{cb-wall} \approx F_{bs} \approx 4\pi R\gamma\cos\theta$ and the total surface area of all liquid bridges would simply be $O_s = 2r^{'}\pi r_z$. By plugging all these expressions into the 'force balance' eq. (**4.1**), one finally obtains the expression (**4.3**). Therefore, the tensile strength (σ_t) of a wet granular pile can be experimentally determined with the measured slope of a rupture plot, i.e. the dependence of $(\omega_c^2 r_z)$ on the $(1/r_z)$ scale.

$$\omega_c^2 r_z = \frac{2\sigma_t}{\rho_s r_z} + 4.64\mu\frac{\pi\gamma\cos\theta}{r^{'}R\rho_s} \tag{4.3}$$

What follows, we describe the experimental technique: a plastic syringe tube, made of polyethylene material with smooth surfaces and having an inner diameter of 20 mm, is initially filled with dry beads of sample volume ≈ 20 ml. For achieving a desired liquid content (W), a defined amount of the wetting liquid (in our case, $Millipore$ water) is subsequently added to the dry bead assembly and a homogeneous liquid distribution is thereafter obtained by vigorously mixing this wet granular sample. Afterwards, the tube's open-end is closed with a syringe piston and the wet bead sample is compactified by pressing the piston with a pressure of about (50 ± 10) kPa, which ensures a reproducible bead-packing. A circular rotation with an angular frequency (ω) is subsequently applied to the tube, horizontally mounted on a centrifuge (cf. **fig. 4.1**a). At a critical angular frequency (ω_c), the granular column ruptures. How a single liquid bridge being ruptured, is schematically shown by the sequence of images in **fig. 4.1**b. Let us consider, two equal sized spherical beads (R) are initially connected by a liquid bridge at zero bead separation

($S = 0$) such that the contact angle $\theta \in \{\theta_{rec}, \theta_{adv}\}$ and the bridge angle $\beta = \beta_1$ (say). For slowly increasing angular frequency (ω), the force (F) acting outwards becomes more strengthen and the contact angle (θ) finally attains its receding limit at a threshold surface separation. Any further increase of the angular frequency (for which S increases) would cause the 'three-phase-contact' lines to move inwards over the bead surfaces; which will result in a lower bridge angle $\beta_2 < \beta_1$. At a critical angular frequency (ω_c), the bead separation (S) reaches its maximum limit above which no liquid bridge can sustain any more. Therefore, the centrifugal force at $\omega \approx \omega_c$ overcomes the attractive capillary bridge force and the liquid bridge ruptures. To obtain the rupture plot, the experiment has been repeated for different granular column lengths (r_z). In **fig. 4.1**c, the experimental data achieved for a wet glass bead assembly ($R \approx 70$ μm, $W = 0.05$) are displayed. Using eq. (**4.3**) mentioned above, the tensile strength (σ_t) of wet granulates is straightforwardly determined.

4.1.2 Determination of the shear stiffness

To determine the shear properties of dry and wet granulates, we use a unique custom-made shear cell which is very similar design as described in ref. [18, 24, 25, 39, 71]. The experimental setup is sketched in **fig. 4.2**. The central part of our shear cell is a cylindrical rim (inner radius $r = 15$ mm, height $H = 10$ mm) made of polycarbonate material. Adjacent to this rim, there are two water reservoirs whose open-ends are separately closed by two latex membranes of thickness ≈ 310 μm each. Here, the red curved lines are the latex membranes, received from HUMBOLDT MGF CO. (USA). The water reservoirs are directly connected to precision microliter syringes (Hamilton-1002 TLL) through PTFE-tubes (inner and outer diameters $= 1.6$ mm and 3.2 mm respectively), coupling threads and fitting grippers. Movements of these syringes' pistons and thus, liquid volumes of the water reservoirs can precisely be regulated by two computer controlled syringe pumps with a home-written Labview program. Note that, the cylindrical rim has a small opening to allow air exchange. By increasing the liquid volume of only one reservoir while reducing the same volume from the other reservoir, the granulates filled into this cylindrical rim can be sheared. The elastic tension of each latex membrane ensures a roughly parabolic shear profile which is very similar to the '$Poiseuille\ flow$' [18, 25]. Hence, such a shearing technique allows

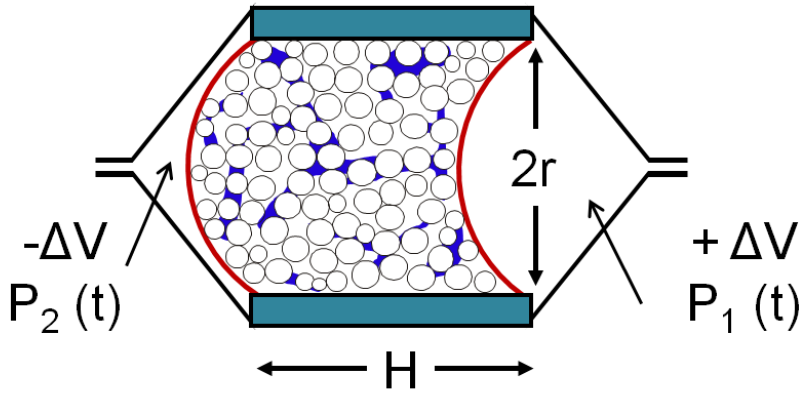

Figure 4.2: Schematic of the shear cell; $r = 15$ mm is the inner radius of cylindrical core and $H = 10$ mm its height. Latex membranes shown as red curved lines separate the granular sample from adjacent liquid reservoirs. During a shear experiment, liquid volumes $\Delta V_1 = -\Delta V_2$ are pushed into one reservoir respectively withdrawn from the other reservoir at a constant volume rate. P_1 and P_2 are the pressures inside these liquid reservoirs at an instantaneous shear time (t).

a homogeneous shear deformation, by keeping the granular avalanches or arching at a tolerable minimum.

To monitor pressures during continuous shearing, three pressure transducers $(24 - PCD$, sensitivity $= 11$ mV per psi) received from RS Components GmbH (Germany) are connected to the water reservoirs. Transducers S_1 and S_2 independently measure the pressures P_1 and P_2 of each water reservoir against the ambient pressure whereas the third transducer S_3 directly records the differential pressure ΔP $(= P_1 - P_2)$. Pressures are recorded as voltage signals using a measurement-card (model: $DAQPAD - 6015$, National Instruments, USA) and a 'Labview Signal Express' program. Prior to connect with the experimental setup, these pressure transducers are separately calibrated using the following protocol. Initially, a pressure sensor is attached to a partially water-filled syringe tube of inner diameter d and subsequently, a known pressure P $(= 4mg/\pi d^2)$ is applied for a short time by placing a known mass (m) on the syringe piston. Here 'g' is the acceleration due to gravity. Recorded output voltage signals are thereafter converted into pressure signals by multiplying with the sensor-sensitivity. For these different pressure transducers, the measured pressure data as plotted against the applied pressure is shown in **fig. 4.3**a. The linear dependence of measured pressure on the applied pressure scale is found to deviate around 10% from the expected pressure data, illustrated as a dotted black line. Therefore, for obtaining

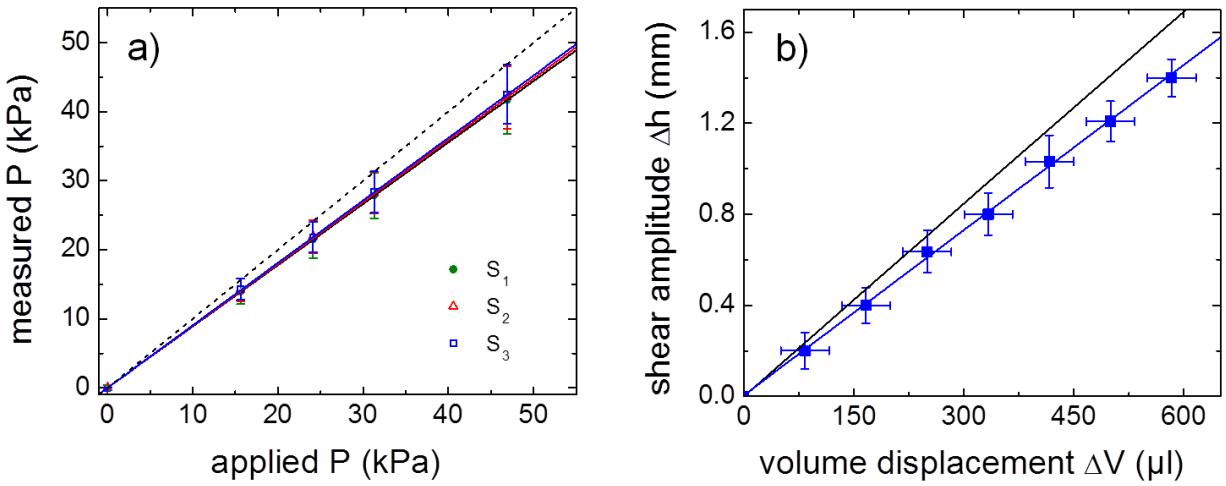

FIGURE 4.3: a) Pressure-calibration data for three pressure transducers (S_1, S_2 and S_3): the measured pressures as plotted for various applied pressures. The dotted line is to be obtained for an ideal pressure system. b) Average shear amplitude (Δh) as a function of the liquid volume (ΔV) dispensed into two water reservoirs. The solid line is the expected shear amplitude as calculated assuming the 'spherical-cap-geometry' shape of the deformed membrane.

the calibrated pressure, the raw pressure signal has to be divided by the slope of respective pressure transducer.

Before starting an elaborate description of the data acquisition technique, it is important to determine the maximum allowable shear amplitude at which a test granular sample is to be continuously shear deformed. The term, shear amplitude (Δh) is defined as the deformation height, measured at the central axis of these attached membranes while the liquid volumes inside its adjacent water reservoirs are varied. The shear amplitudes of two latex membranes are separately measured by controlling liquid volumes of two water reservoirs and in **fig. 4.3**b, the average shear amplitude is plotted as a function of the dispensed liquid volume (ΔV). The black straight line is the expected amplitude, calculated assuming the '*spherical-cap-geometry*' shape. However, the observed deviation of measured Δh from the expected line as more liquid dispenses in is presumably due to the divergence from an ideal '*spherical-cap-geometry*' shape. In order to ensure a considerable shear deformation and the irreversible particle-motion, the maximum shear amplitude should be chosen large enough in compared to the grain sizes. If not specifically mentioned later on, the maximum shear amplitude (Δh_{max}) in all our experiments is kept at

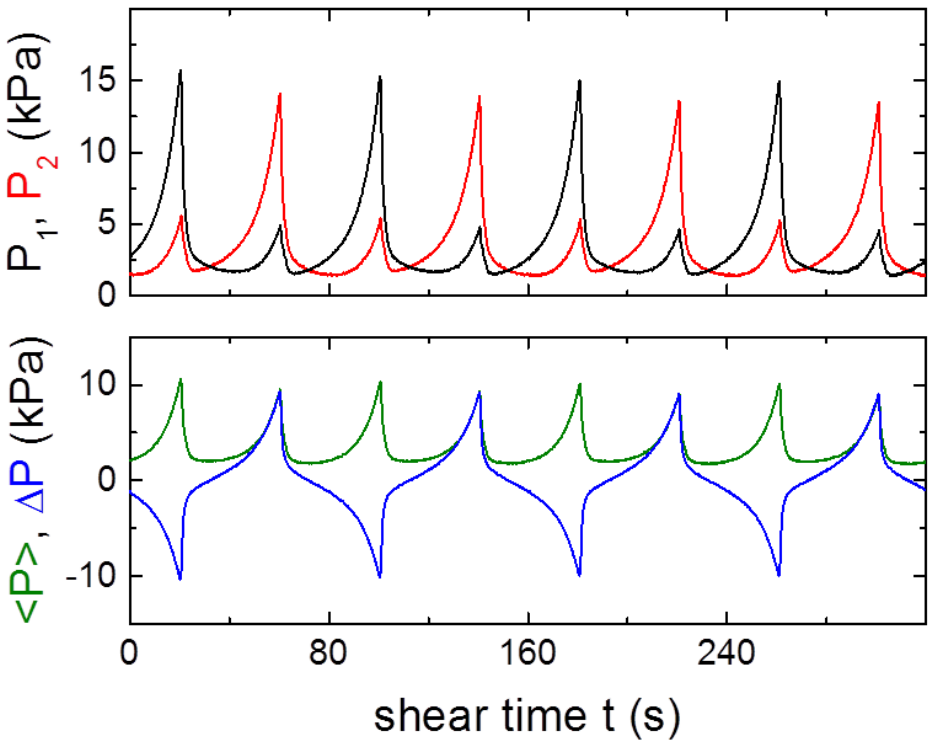

Figure 4.4: (Color online) top) During four consecutive shear cycles, recorded pressures P_1 and P_2 plotted as a function of the shear time (t) for both liquid reservoirs. bottom) Average pressure $< P > = \frac{1}{2}(P_1 + P_2)$ and differential pressure $\Delta P = (P_1 - P_2)$ as a function of the shear time (t). The shear periodicity $T \approx 80$ s.

about 0.8 mm, around (2-6) times the bead diameter.

Prior to start of an experiment, a wet granular sample is prepared by adding the wetting fluid ($Millipore$ water) to dry glass or basalt granules and thereafter, it is vigorously mixed for obtaining a homogeneous wet granular assembly. According to this preparation procedure, the liquid content (W) is defined as the ratio of added liquid-volume to total assembly-volume. Thereafter, thus prepared wet granulates are filled in the cylindrical rim and sealed by the water reservoirs. In the following, initial and absolute pressures are adjusted by controlling liquid volumes inside the water reservoirs and a pre-shearing is performed to obtain reproducible results. By the definition, an initial pressure (P_{int}) is obtained by averaging pressure signals P_1 and P_2, recorded at a time $t = 0$ of a shear cycle and an absolute pressure (P_{abs}) is determined by averaging pressure signals P_1 and P_2, measured over an entire shear cycle. Potentially if needed, P_{int}

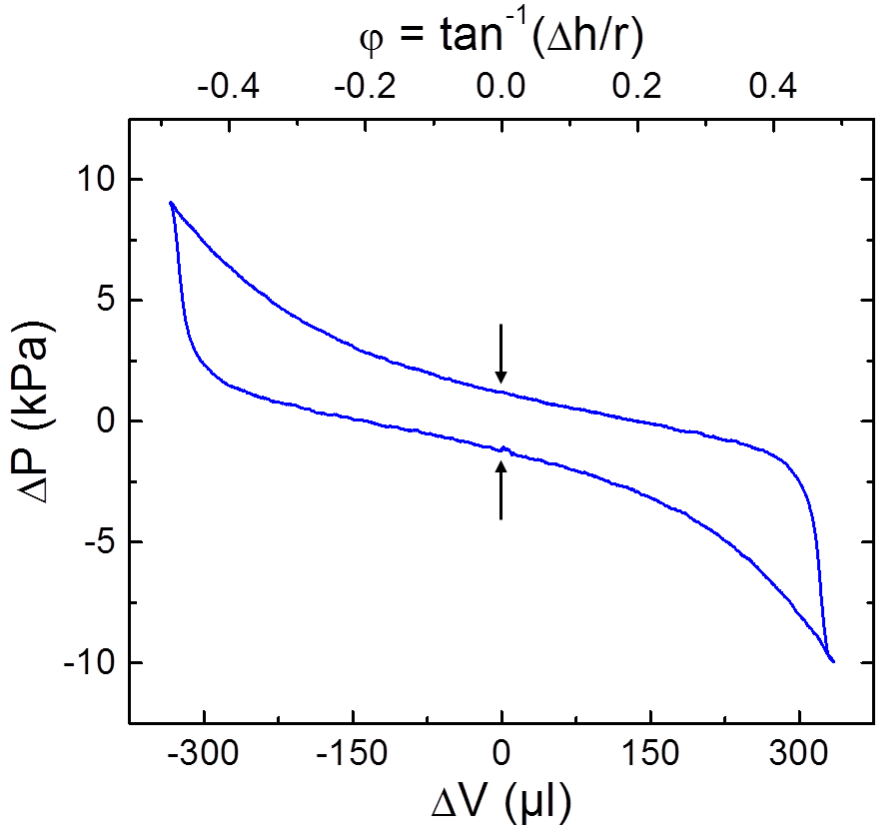

FIGURE 4.5: Differential pressure (ΔP) of a single cycle replotted as a function of the shear angle (φ) and the volume displacement (ΔV) shows a characteristic hysteresis loop. The shear angle is determined as $\varphi = \tan^{-1}(\Delta h/r)$. The difference of ΔP at $\Delta V = 0$ and $\varphi = 0$ is the measure of shear stiffening (P_{sp}). Data taken from the above **fig. 4.4** (bottom panel).

and P_{abs} are readjusted. And finally, the pressure signals are recorded *in-situ* during continuous shearing at a defined shear rate (γ') which is determined as follows: while two syringe pistons move at a same speed but in opposite directions to each other, the liquid volumes inside two water reservoirs continuously change. As a result, the granular sample filled into the cylindrical core is deformed at a constant volume rate of $\left(\frac{\Delta V}{t}\right)$. Hence, the corresponding height-deformation rate will simply be $\left(\frac{\Delta h}{t}\right)$. Therefore, the shear rate of an applied shear profile is straightforwardly obtained as $\gamma' = \frac{1}{r}\left(\frac{\Delta h}{t}\right)$ where r is the radius of the cylindrical rim.

During four consecutive shear cycles of periodicity $T \approx 80$ s, the recorded pressure signals P_1 (black curve) and P_2 (red curve) plotted as a function of the shear time (t) is shown in **fig. 4.4** (top panel); these pressure data are obtained of wet glass granulates ($R \approx 70$ μm, $W = 0.01$)

for $\gamma' \approx 2.66 \times 10^{-3}\ s^{-1}$ at $P_{int} \approx 2.1$ kPa and $P_{abs} \approx 3.5$ kPa. In **fig. 4.4** (bottom panel), the green and blue curves display the extracted average pressure $\langle P \rangle = \frac{1}{2}(P_1 + P_2)$ and differential pressure $\Delta P = (P_1 - P_2)$ respectively. In **fig. 4.5**, the differential pressure data (ΔP) are re-plotted as a function of the volume displacement ΔV and the shear angle $\varphi = \tan^{-1}(\Delta h/r)$. The characteristic hysteresis loop in **fig. 4.5** is presumbly resulted for the granular stiffness opposing the applied shear deformation, whereas the slopes of two branches are caused due to restoring forces of the latex membranes [18, 25]. The stiffening pressure (P_{sp}) is determined by the opening of hysteresis curve at zero volume displacement, i.e. $\Delta V = 0$. To eliminate the undesirable signal-noise of membranes alone, the same cyclic shear profile is also applied to the closed shear cell, but without filling test granulates in the cylindrical rim and the pressures are recorded. Subsequently, a small 'opening pressure' ≈ 0.4 kPa, measured at $\Delta V = 0$ for very similar data plotting (not shown here) as in **fig. 4.5**, is subtracted from the raw stiffening pressure data to achieve the normalized stiffening pressure.

4.2 Experimental results and discussion

4.2.1 Dependence of mechanical stability on the liquid content

For wettable glass granulates of radius $R \approx 70$ μm, the mechanical stability under tensile stress has been investigated with our centrifuge setup and the corresponding tensile strength data (σ_t) as a function of the liquid content (W) is displayed in **fig. 4.6**a. These experimental findings exhibit the same characteristic features what have been observed in ref. [39, 49]. As the liquid content W gradually increases, the tensile strength sharply reaches a plateau ≈ 700 N/m^2 at around $W \approx 0.005$. However, in case of higher liquid contents (W) for $0.005 \lesssim W \lesssim 0.15$ (approximately), the tensile strength remains largely independent on the liquid content (W) scale.

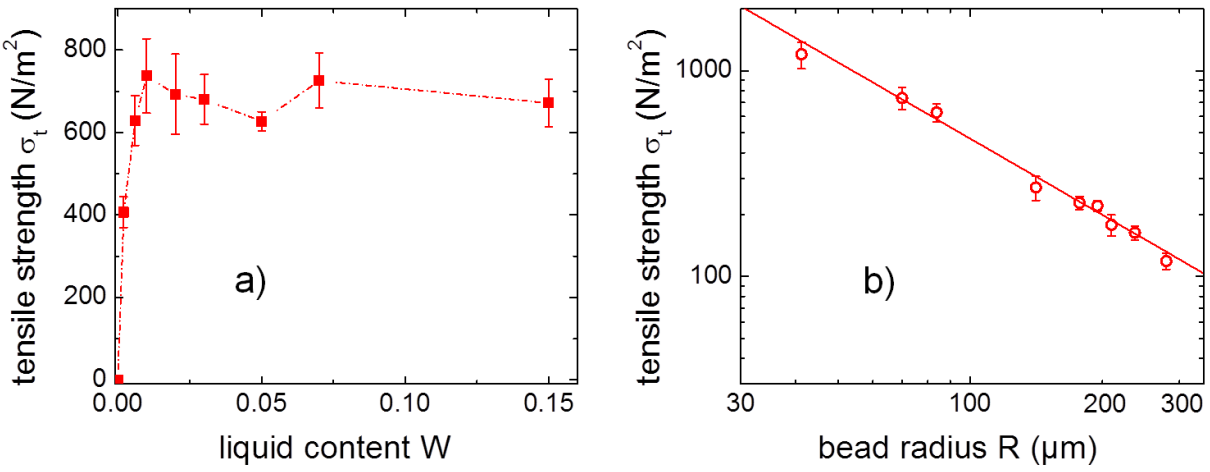

FIGURE 4.6: a) Tensile strength (σ_t) as a function of the liquid content (W) for wet glass granulates ($R \approx 70$ μm). b) Dependence of tensile strength (σ_t) on the bead radius (R) for same glass granulates at a defined liquid content of $W = 0.01$, as plotted on a log-log scale.

It is fairly understood from the discussion in **section 2.1.2** that for gradually increasing W, added liquid volumes first saturate the local roughness on the bead-surfaces. Consequently, ideal capillary bridges appear between neighbouring glass beads at their mutual contacts by resulting around 6.4 wet contacts per bead [39, 48, 49]. At a high liquid content $W \gtrsim 0.024$, individual capillary bridges will merge to form large liquid clusters; however, the Laplace pressures of large liquid structures are shown to be smaller than the Laplace pressure of a largest capillary bridge

[39, 48, 49]. As a result, the attractive capillary forces and hence, the tensile strength (σ_t) of a wet bead pile is expected to remain approximately constant up to a large liquid content, well beyond the 'bridge force dominated' regime. However, a possible 'liquid drainage' due to the applied centrifugal force might account for large experimental scatters.

In order to find the dependence of granular strength for variable bead sizes, the tensile strength (σ_t) is investigated as a function of the bead radius (R) for same wettable glass granulates at a defined liquid content of $W = 0.01$. The experimental data, presented on a log-log scale in **fig. 4.6**b, reveal that the tensile strength (σ_t) inversely scales with the bead radius (R) where the corresponding slope is obtained to be about 1.2. The qualitative behaviour of the tensile strength (σ_t) on the grain sizes is in good agreement with the theoretical prediction as derived by H. Rumpf [63].

In **fig. 4.7**, the stiffening pressure P_{sp} of wettable glass granulates (filled squares) and less-wettable basalt granulates (filled circles) is plotted as a function of the liquid content W. Bead sizes of $R \approx 70$ μm, absolute pressure of $P_{abs} \approx 4$ kPa and shear rate of $\gamma' \approx 2.66 \times 10^{-3}$ s^{-1} are identical for both bead assemblies. Although no attractive capillary cohesion is present for dry granulates, i.e. at $W = 0$, a small stiffening pressure $P_{sp} \approx 0.30 - 0.40$ kPa is measured for both dry granular packs. As W gradually increases, P_{sp} sharply raises reaching a plateau for $0.005 \lesssim W \lesssim 0.15$; where the mechanical stiffness i.e. P_{sp} is fairly independent on the liquid content. But, the stiffening pressure at larger liquid contents $W \gtrsim 0.20$ are observed to decrease about linearly with the increasing liquid content.

For wettable glass granulates, the qualitative behaviour of the stiffening pressure on the liquid content is in good agreement with the characteristic results as published in ref. [25, 39, 48] and will only be discussed to the extent, needed for the further comparison. A finite stiffening pressure at $W = 0$ might result from the unavoidable friction between sheared granulates and/or minute liquid necks formed due to capillary condensation at the touching-asperities of microscopically rough bead-surfaces. As the liquid content increases, the wetting fluid must saturate the roughness on the bead-surfaces and consequently, ideal capillary bridges will appear at direct contacts of neighbouring beads. The increasing shear stiffness due to the gradual formation of capillary bridges [24] can be approximated by the following expression:

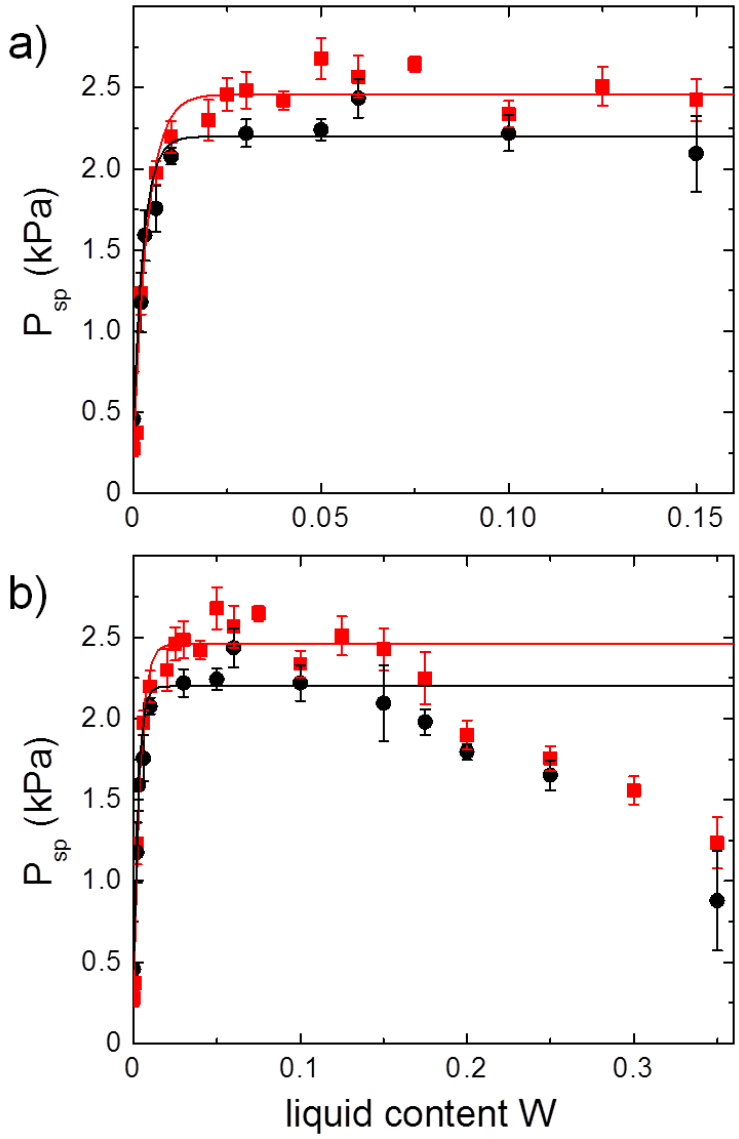

FIGURE 4.7: a) Stiffening pressure (P_{sp}) as a function of the liquid content (W) for wettable glass (filled squares) and less-wettable basalt (filled circles) granulates. b) Sample data as shown in a) but for an extended liquid content W. A weakening tendency of P_{sp} can be observed at a liquid content above $W = 0.15$. For both wet granulates, beads' sieve fraction: $125 - 150$ μm, $R \approx 70$ μm, $\gamma \approx 2.66 \times 10^{-3}$ s^{-1} and $P_{abs} \approx 4$ kPa.

$$P_{sp} = P_{sp}(0) + P_m \left(1 - e^{\frac{-W}{W_0}} \right) \tag{4.4}$$

Here, $P_{sp}(0)$ is the stiffening pressure for completely dry granulates. Using this formulae, the plateau value of the stiffening pressure (i.e. $P_{m,glass}$) for wettable glass granulates is obtained to be (2.18 ± 0.05) kPa and the characteristic liquid content $W_0 \approx 0.003$ corresponds to the liquid volume, required to saturate the microscopic crevices on the bead-surfaces. At higher liquid contents $W \gtrsim 0.024$, isolated capillary bridges merge to form large liquid clusters whereas the effective Laplace pressures of liquid morphologies and hence, the capillary force per bead-contact remains almost constant up to a liquid content of about $W \approx 0.15$ [48, 49] as shown for wettable glass granulates. Therefore, the stiffening pressure P_{sp} stays nearly unaffected within a large liquid content regime for $0.005 \lesssim W \lesssim 0.15$. But, the stiffening pressure is reduced at significantly higher liquid contents, much larger than the percolation threshold of liquid clusters. A percolation transition is suggested to be occurred at a liquid content, ranged between $W \approx 0.08$ and $W \approx 0.11$ [25, 48, 49]. At a considerably high $W = 0.35$ (that means, around 90% of available pore volume are saturated with the wetting fluid), individual glass granulates are almost immersed into water and consequently, a weak capillary cohesion is resulted. Hence, the wet glass bead pile experiences a small stiffening pressure.

For less-wettable basalt granulates, the dependence of stiffening pressure on the liquid content is very similar to the results of wettable glass granulates as seen earlier; which is even expected for the same type of capillary forces. But, the corresponding height of the plateau value, i.e. $P_{m,basalt} = (1.74 \pm 0.05)$ kPa is just 20% smaller than the plateau value obtained for glass bead sample, i.e. $P_{m,glass} = (2.18 \pm 0.05)$ kPa. This is unexpected when one compares the capillary bridge forces between the pairs of glass and basalt beads at zero separation (i.e. $S = 0$) - by assuming the advancing contact angle θ_{adv} of water on the glass and basalt surfaces. In that case, the bridge force between two basalt beads is estimated to be only about 25% of the bridge force between two glass granules, as calculated by eq. (**2.3**). However, when two neighbouring beads move relative to each other by resulting a finite surface separation $S > 0$, the receding contact angle θ_{rec} on the glass and basalt bead surfaces and hence, the contact angle hysteresis

becomes more relevant in describing the attractive capillary cohesion.

To explain the spatial evolution of a capillary bridge existing between two identical beads (R) at zero surface separation, let us assume that the local contact angle (θ) everywhere on the contact lines is close to the stable advancing contact angle (θ_{adv}). Due to the relative motion of shearing beads, the surface separation S might be increased. Consequently, the capillary bridge is stretched and the contact angle (θ) gradually decreases until $\theta = \theta_{rec}$ (stable receding contact angle). However, the contact lines would start to slide on the bead-surfaces for any further increase of the bead separation. This process will continue until the liquid bridge becomes unstable and pinches off at a maximum separation $S = S_c$. To account for the contact angle hysteresis, numerical studies driven by the minimization of interfacial energies for liquid surfaces are conducted by Ciro Semprebon and Martin Brinkmann from MPI-DS, Göttingen (Germany) using a program, called 'Surface Evolver' [77]. As the contact angles are well below $90°$, it is assumed that a capillary bridge between two identical beads of radius R is symmetric with respect to the line joining their centres, and the local contact angle (θ) satisfies the inequality: $\theta_{rec} \leq \theta \leq {}_{adv}$ for gradually increasing surface separation S. In **fig. 4.8**a, the capillary bridge

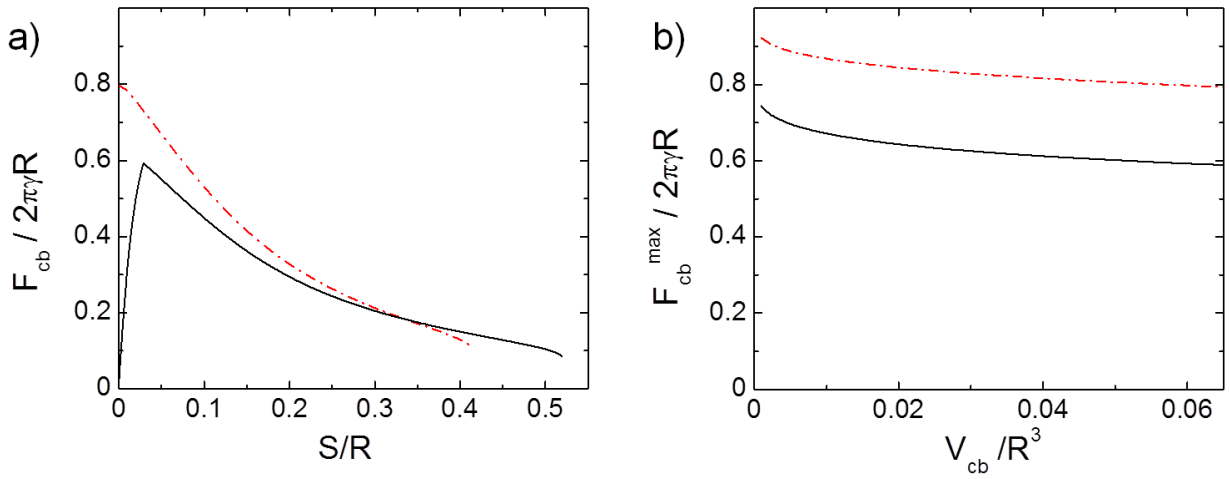

FIGURE 4.8: a) Capillary bridge force ($F_{cb}/2\pi\gamma R$) as a function of the surface separation (S/R) for a fixed liquid volume of $V/R^3 = 0.06$ with wettable glass (dash-dotted curve) and less-wettable basalt (solid curves) spheres. b) For same bead types, the maximum capillary bridge force ($F_{cb}^{max}/2\pi\gamma R$) plotted as a function of the liquid volume (V/R^3). Here, R = bead radius and γ = interfacial tension. These results provided by Ciro Semprebon and Martin Brinkmann from MPI-DS, Göttingen (Germany).

force F_{cb} as a function of the surface separation S is shown for glass beads (dash-dotted curve) with $\theta_{rec} = 5^{\circ}$, $\theta_{adv} = 10^{\circ}$ and for basalt beads (solid curve) with $\theta_{rec} = 32^{\circ}$, $\theta_{adv} = 76^{\circ}$. In both cases, the liquid volume is set to $V = 0.06R^3$ which corresponds to a largest possible capillary bridge to be found at a liquid content $W \gtrsim 0.024$ [48, 49]. **Fig. 4.8**b shows the dependence of maximum capillary bridge force F_{cb}^{max} on the liquid volume V, obtained for wettable glass beads (dash-dotted curve) and less-wettable basalt beads (solid curve). As can be seen in **fig. 4.8**, the ratio of maximum bridge forces corresponding to the basalt and glass granules at a normalized liquid volume $V/R^3 = 0.06$ is about 0.75; which is reasonably comparable to the ratio of maximum stiffening pressures, i.e. $(P_{m,basalt}/P_{m,glass}) = 0.80$. Thus, we conclude that the mechanical properties of sheared wet granulates are determined by the receding contact angle (θ_{rec}) on the bead-surfaces. However, a small discrepancy (around 5%) between these two independent ratios might be resulted due to large experimental scatters of the stiffening pressure data.

4.2.2 Dependence of shear stiffness on the shear rate

For various liquid contents, the stiffening pressure P_{sp} of wettable glass granulates at an absolute pressure of $P_{abs} \approx 4$ kPa has been studied as a function of the shear rate (γ') and the experimental data are displayed in **fig. 4.9**a. At an extremely small liquid content $W = 0.002$, the stiffening pressure $P_{sp} \approx 1$ kPa (open squares) is almost independent on the applied shear rate. The stiffening pressures obtained at higher liquid contents of $W = 0.01$, 0.03 and 0.05 are displayed by distinct symbols, labelled as filled squares, filled circles and open diamonds respectively; for these wet glass bead samples, the stiffening pressure noticeably depends on the shear rate scale. Such an observation is very similar to the characteristic behaviour of the yield pressure data as found for wet glass granulates [18, 25]. The stiffening pressure P_{sp} (filled triangles) of a wet glass bead pile, prepared for a significantly large liquid content of $W = 0.20$, is around 30% small in compared to the stiffening pressure data as obtained for $0.01 \leq W \leq 0.05$ earlier. Within large experimental scatters, the stiffening pressure data of this particular wet bead assembly of $W = 0.20$ exhibits no shear rate dependence. To directly compare, the experimental results of similar shear experiments performed with less-wettable basalt granulates are shown in **fig. 4.9**b.

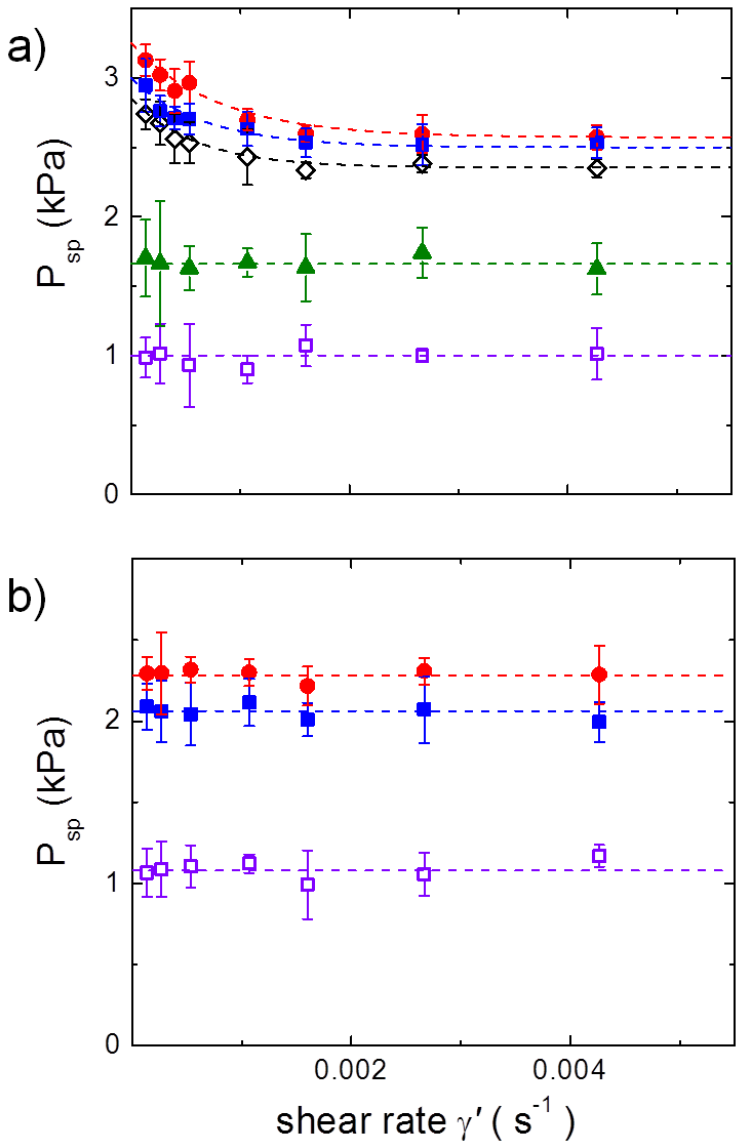

FIGURE 4.9: (Color online) Stiffening pressure (P_{sp}) plotted as a function of the shear rate (γ') for a) wettable glass and b) less-wettable basalt granulates. These experimental data are obtained for various liquid contents of $W = 0.002$ (open squares), 0.01 (filled squares), 0.03 (filled circles), 0.05 (open diamonds) and 0.20 (filled triangles). For both wet granulates, the bead sizes and absolute pressure are the same as in **fig. 4.7**.

Alike wettable glass beads, P_{sp} of wet basalt granulates at $W = 0.002$ is fairly constant on the shear rate scale. More interestingly, the stiffening pressure data of less-wettable basalt granulates as compared to wettable glass granules are found to be largely insensitive on the applied shear rate for same liquid contents, i.e. $W = 0.01 - 0.03$.

For a wet (glass or basalt) bead assembly at $W = 0.002$, a small stiffening pressure is not very surprising; since minute liquid volumes trapped around particle-particle contacts will contribute an attractive cohesion (see **section 2.1.2**), the wet granular pile is expected to experience a small shear stiffening of $P_{sp} \approx 1$ kPa. At a higher liquid content, ranged between $W = 0.01$ and $W = 0.05$, fully developed capillary bridges and small liquid clusters significantly dominate inside a wet glass pile (see **section 2.2.1**) and consequently, a higher stiffening pressure should prevail for strong capillary forces within these wet bead assemblies at $W = 0.01 - 0.05$. A certain rate dependence of the stiffening pressure data (i.e. P_{sp}) might be attributed for the temporal evolution of capillary bridges and/or small liquid structures [24] within wettable glass granulates. These experimental results also suggest that the applied shear dynamics can itself account for the 'shear thinning effect' [18, 25]; which physically explains that the 'flow resistance' of wet granulates might be decreased for increasing shear rate (γ') and vanished at/above a threshold shear rate - like any other viscous fluid. The stiffening pressure data of these particular wet glass granulates for $0.01 \leq W \leq 0.05$ are found to be well described by the following equation:

$$P_{sp} = C_1 + C_2 \left(e^{\frac{-\gamma'}{\gamma'_0}} \right) \tag{4.5}$$

Here, C_1 and C_2 are constants. The notation γ'_0 denotes the characteristic shear rate and consequently, the characteristic equilibration time t_0 $(= 1/\gamma'_0)$ is obtained to be about (24 ± 4) min. For less-wettable basalt granules of $W = 0.01 - 0.03$, the insensitivity of shear stiffness (i.e. P_{sp}) on the shear rate (γ') might be caused due to the non-existing evolution dynamics of distributed liquid structures. In addition, the 'liquid flow' within wettable glass bead packs might proceed over the bead-surfaces, not via the vapour phase. Otherwise, a similar shear rate dependence is also expected to occur for wet basalt bead assemblies of similar liquid contents. At a significantly higher liquid content of $W = 0.20$ (i.e. around 50% of available pore volume being

filled with the wetting fluid), large liquid structures are expected to predominate inside a wet glass bead assembly since the average number of isolated liquid bridges and small liquid clusters will substantially drop down. As a consequence, the reduced capillary cohesion might account for its smaller stiffening pressure of $P_{sp} \approx 1.6$ kPa. Moreover, as the percolation transition of liquid morphologies is indicated to start at a threshold liquid content $W_p \approx 0.08 - 0.11$ [25, 48, 49], the 'liquid flow' through percolated liquid morphologies should be much faster than the 'liquid exchange' occurring between individual capillary bridges and/or small liquid clusters via thin liquid films, adsorbed on the glass bead-surfaces. Hence, the shear rate dependence of P_{sp} is expected to disappear for this particular wet glass granulates of liquid content $W = 0.20$, well above the percolation threshold.

In search for the liquid equilibration process within wettable granulates, let us consider a static configuration of three monosized glass spheres (R) in mutual contact, as schematically shown in **fig. 4.10**a. We further assume that these glass spheres are connected by three isolated capillary bridges of different liquid volumes. As evident from the local packing configuration, these individual spheres have an angle of 60° to each others. Nevertheless, a volume-exchange process will occur due to pressure differences between these liquid bridges; where small capillary bridges are expected to receive liquid volumes from the larger one [39, 48, 49]. Therefore, for such an equilibration dynamics to come at an end, the liquid might travel a maximum transport distance $\lambda = \left(\frac{2\pi R}{6}\right)$ on the bead-surfaces, since $2\pi R$ is the circumference of a circle. Assuming a similar equilibration dynamics as described in ref. [51] and ignoring the possible influences of contact angle hysteresis, we expect for a (strictly) 2D model system that the lateral transport distance (λ) and the corresponding equilibration time (t_0) are associated by the following expression:

$$\frac{1}{t_0} = a\left(\frac{2\pi}{\lambda}\right)^2 = a\left(\frac{6}{R}\right)^2 \tag{4.6}$$

It has been pointed out [18, 24] that the equilibration time (t_0) should scale as $\left(\frac{\eta}{\gamma}\right)$ where γ and η are the interfacial tension and viscosity of the test fluid. Therefore, the above expression (**4.6**) of liquid equilibration dynamics takes the simplified form:

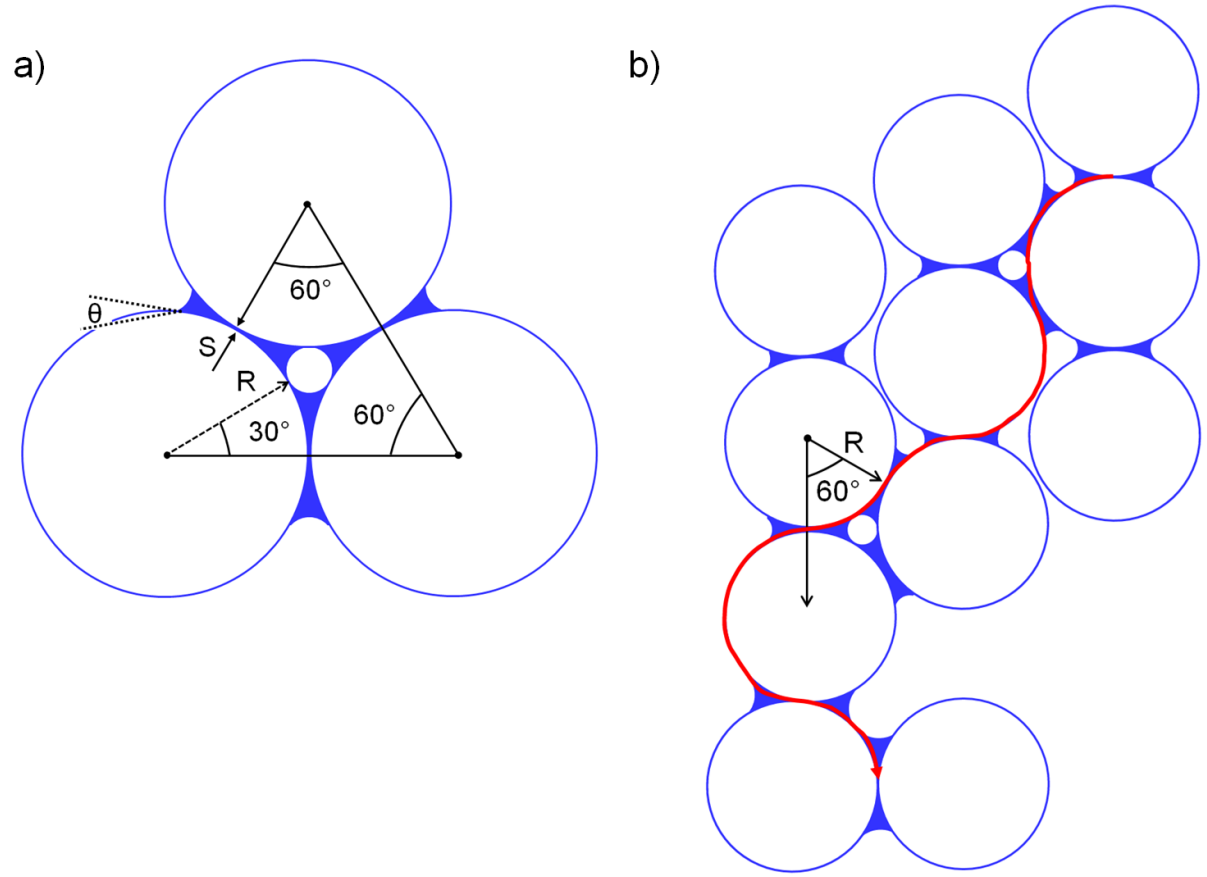

Figure 4.10: a) Schematic sketch of a local grain-configuration: three identical beads (R) at their mutual contacts are connected by three isolated capillary bridges. b) Schematic illustration describing a long distance liquid transport mechanism: the liquid might flow a large distance via thin liquid films, covered on the bead-surfaces.

$$\frac{1}{t_0} \propto \left(\frac{\gamma}{\eta R^2}\right) \tag{4.7}$$

To evaluate the proposed model, the experimentally obtained equilibration time should be compared with the expected equilibration time from above eq. (**4.7**). In this aspect, we consider the liquid equilibration time, experimentally found for various wet glass granulates with X-ray microtomography by Mario Scheel and Marc Schaber [39, 50]. For their tomographic studies, different wet bead samples are prepared with monosized glass microspheres and various kind of wetting liquids, distinguished by the surface tension (γ) and viscosity (η). The corresponding

liquid equilibration times (t_0) are presented in **table 4.1** (top). Here, the wet granular samples as labelled with IDs: A, B, C and D respectively, are sorted out according to the bead radius (R), surface tension (γ) and viscosity (η). The theoretical description of the liquid equilibration in 2D model system is found to be a good approximation, while comparing different equilibration times as shown in **table 4.1** (bottom). Nevertheless, it should be addressed that the liquid inside (any) real wet granulates has an equal probability to distribute in all directions. However, a

Wet Glass Bead Samples[1]				
Sample ID	R (μm)	γ (mN/m^2)	η (mNs/m^2)	$t_{0,X}$ (s)
A	280	75	1	100 ± 30
B	280	50	1	130 ± 30
C	390	75	2	300 ± 100
D	195	72	2	115 ± 10

Comparison		
	From Above Panel	Approx. Ratio
$t_{0,B}/t_{0,A}$	1.3 ± 0.2	1.5
$t_{0,C}/t_{0,A}$	3.0 ± 0.2	3.8
$t_{0,D}/t_{0,A}$	1.2 ± 0.3	1.0

Table 4.1: Top panel: Liquid equilibration times (t_0) as obtained with X-ray microtomography for various wet glass bead assemblies. Bottom panel: A direct comparison between the experimentally measured and theoretically calculated equilibration times.

large characteristic time of $t_0 \approx 24$ min as obtained for sheared wet glass granulates indicates a slow equilibration dynamics as compared to the liquid redistribution process in a local bead configuration. Accordingly, the resultant liquid transport distance (λ) is estimated to be around ($2.5 \times 2\pi R$). It suggests a long distance liquid transport mechanism leading to an equilibration in a sheared wet glass bead pile. A schematic sketch as drawn in **fig. 4.10**b describes that the

[1]Samples A-C : studied by Mario Scheel [39]; Sample D : studied by Marc Schaber

liquid might travels a large distance on the bead-surfaces. Further studies are needed to clarify this slow equilibration process for wettable glass granulates, continuously shearing.

4.2.3 Dependence of shear stiffness on the compressive stress

To explore the dependence of granular strength on the applied compressive stress, shear experiments are conducted for varying initial pressure (P_{int}); where we have restricted to wettable glass granulates of same bead sizes and for the same shearing rate as in the previous experiments. The stiffening pressure P_{sp} as a function of the initial pressure P_{int} is plotted in **fig. 4.11**, for dry glass beads (open squares) and two distinct wet glass granulates, prepared by $Millipore$ water (open circles) and a water-glycerol mixture (open triangle) at a defined liquid content, $W = 0.03$. For the later case, a water-glycerol mixture ($70 : 30$ wt.%) is freshly prepared with pure glycerol and $Millipore$ water, before adding the wetting fluid to dry granulates.

In case of dry granulates, the stiffening pressure of $P_{sp} \approx 0.40$ kPa is roughly constant up to an initial pressure $P_{int} \lesssim 1$ kPa and it is identical with the value as obtained at zero liquid content in **fig. 4.7**. At large initial pressures $P_{int} \gtrsim 2$ kPa, the stiffening pressure rises almost linearly for increasing initial pressure with a slope of 0.83. In contrast, the stiffening pressure of water-wetted glass granulates is significantly large at minute initial pressures, and slowly increases with a slope of 0.66 up to an initial pressure $P_{int} \lesssim 10$ kPa; but, the linear rise in large initial pressure regime, i.e. above $P_{int} \approx 10$ kPa becomes relatively steep by resulting a higher slope about 0.70. It is however remarkable that the stiffening pressure of water-wetted glass granulates is small in compared to a dry glass bead pack, for very similar initial pressures $P_{int} \gtrsim 10$ kPa. This means that a dry granular pile which is very soft at small compressive stress (i.e. P_{int}) with an almost fluid like behaviour, becomes mechanically more stiffer than a wet granular assembly at sufficiently large initial pressures.

To unravel the origin of the shear stiffening, the packing fraction (ρ) as a function of the initial pressure (P_{int}) is displayed in **fig. 4.12** for dry glass granules (open squares) and a water-wetted glass bead pile (open circles) prepared of a liquid content $W = 0.03$. These data are obtained for similar shear experiments conducted of same glass bead sizes and for the same shear rate as in **fig. 4.11**. Here, the packing fraction of a (dry or wet) bead assembly is straightforwardly

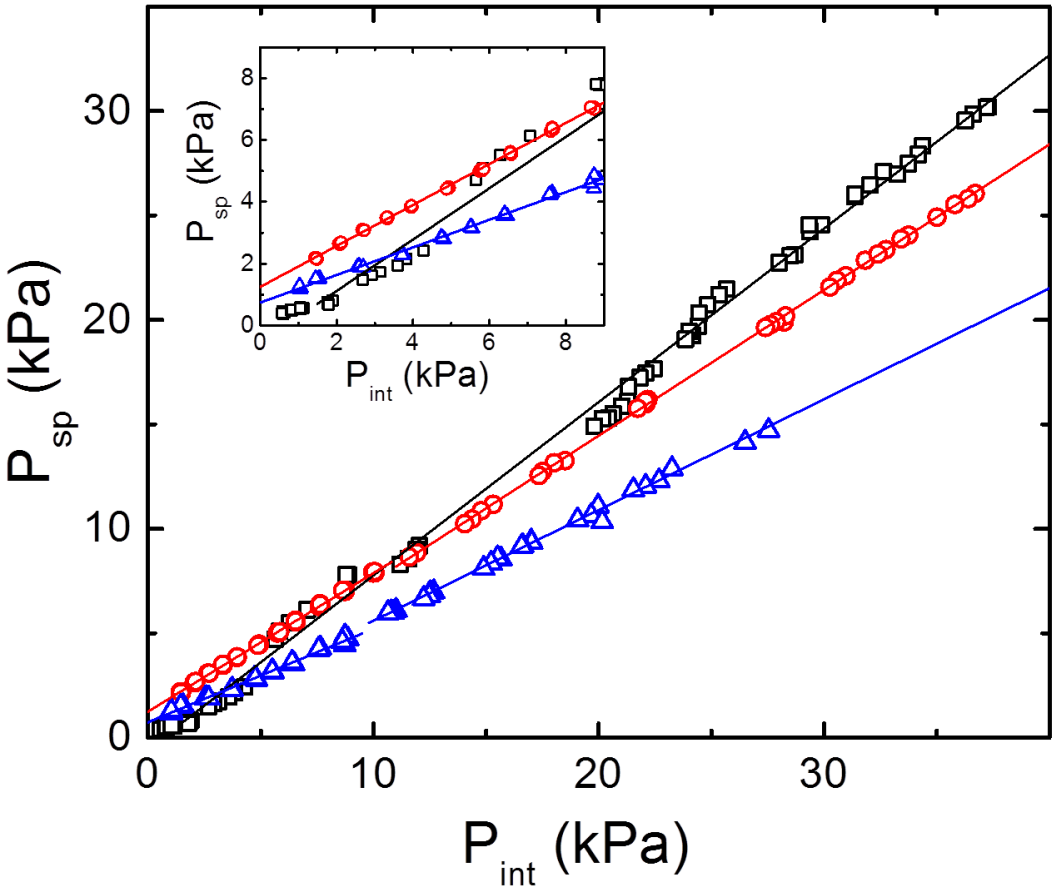

FIGURE 4.11: Stiffening pressure (P_{sp}) as a function of the initial pressure (P_{int}) for dry glass granulates (open squares), a water-wetted glass bead sample (open circles) and a pile of glass beads, wetted by a water-glycerol mixture ($70:30$ wt.%) (open triangles). Both wet granulates are prepared for a liquid content of $W = 0.03$. Bead sizes and applied shear rate are identical of the shear runs as shown in **fig. 4.7**. The inset displays the same measurement data, but zoomed into a smaller scale of the initial pressure for $0 \leq P_{int} \leq 9$ kPa.

obtained as $\rho = \left(\frac{V_b}{V_{cy}-2\Delta V}\right)$ where ΔV = volume displacement into each water reservoir, V_b = total volume of the beads and V_{cy} = volume of the cylindrical core. For dry granulates consisting of spherical glass beads, the packing fraction (ρ) at close to vanishing P_{int} is obtained to be about 0.60; which, for gradually increasing initial pressure, further increases slowly and a higher packing fraction $\rho \approx 0.615$ is resulted at $P_{int} \approx 30$ kPa (cf. **fig. 4.12**). However, the packing density of real glass beads having finite surface roughness is relatively smaller than the theoretical limit of 64% [29] to be achieved for a randomly close-packed assembly of frictionless spheres. On the force

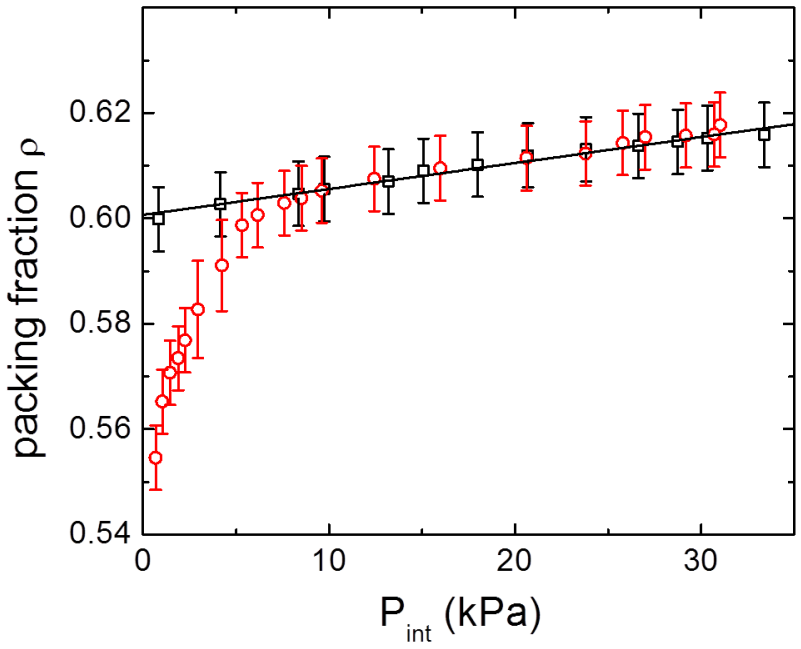

Figure 4.12: Packing fraction (ρ) of bead matrix as a function of the initial pressure (P_{int}) for a dry assembly of glass beads (open squares) and a wet pile ($W = 0.03$) of glass granulates, wetted by $Millipore$ water (open circles). Experimental parameters are kept same as of the shear experiments displayed in **fig. 4.9**. Both bead packs have similar packing densities above a certain threshold, i.e. $P_{int} \gtrsim 10$ kPa.

scale, we can safely neglect any interaction between individual (perfectly) dry granulates except the frictional forces, since individual beads are moved relative to each other during continuous shearing. Therefore, the resultant stiffening pressure at small initial pressures $P_{int} \lesssim 1$ kPa can be understood in terms of the unavoidable friction between granulates hindering their movement. But, at higher initial pressures above a certain threshold, i.e. $P_{int} \gtrsim 2$ kPa in our case, it can be assumed that the movement of individual beads experiences a stronger geometrical hindrance due to almost compact bead assembly. As a result, the frictional force is expected to be intensified and hence, the stiffening pressure P_{sp} of dry granulates increases strongly for any further rise of the initial pressure above $P_{int} \gtrsim 2$ kPa.

From **fig. 4.12**, the packing fraction (ρ) of water-wetted glass granulates at nearly vanishing P_{int} is found to be around 55.5%. A similar packing density of static wet glass granulates as independently determined by X-ray microtomography is mentioned in ref. [39, 48, 49]. For gradually increasing initial pressure, the packing fraction of water-wetted granulates sharply rises

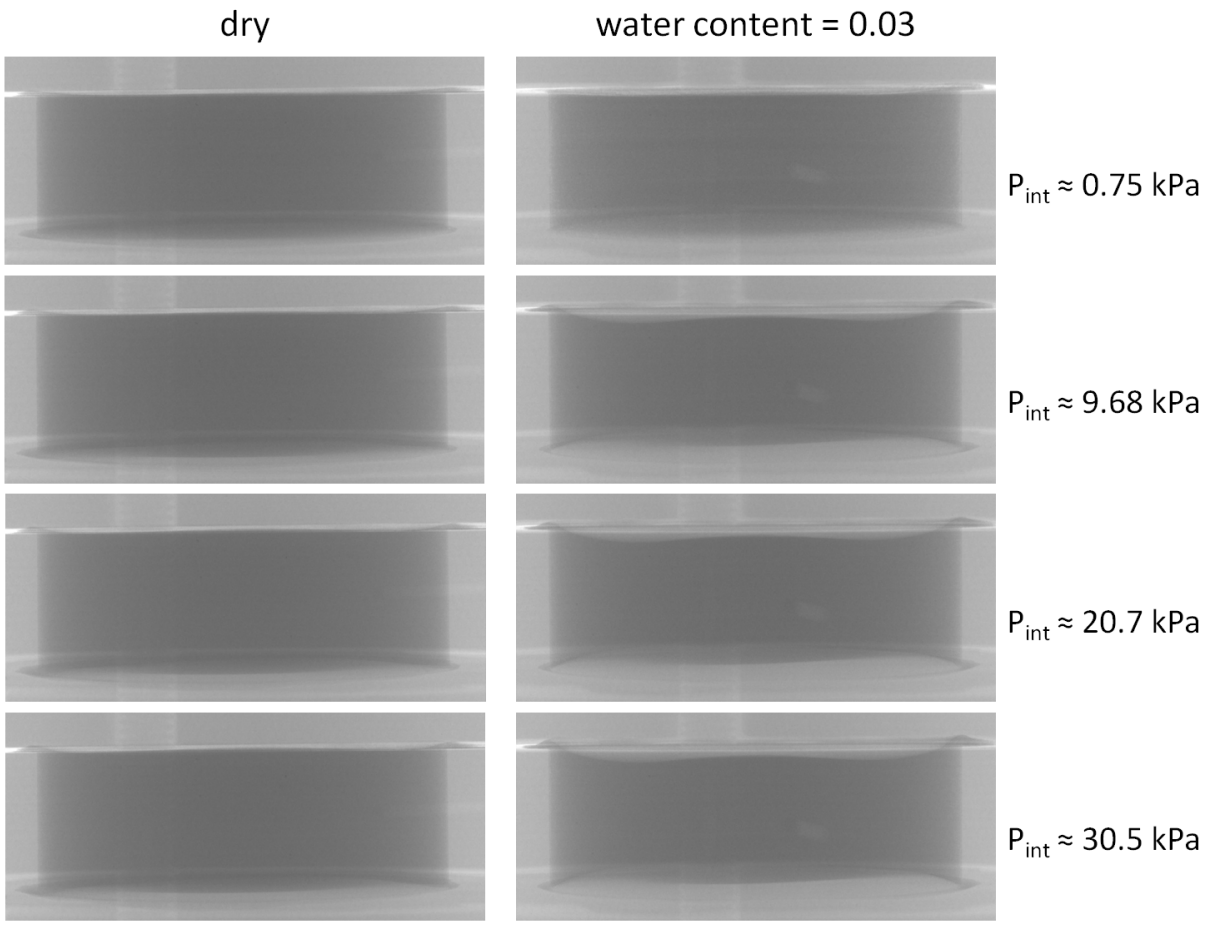

FIGURE 4.13: X-ray radiographic images for different initial pressures (P_{int}), applied to a test (dry or wet) granular sample. Left column: dry glass granulates (beads' sieve fraction: $125 - 150$ μm, $R \approx 70$ μm). Right column: same glass beads, wetted by $Millipore$ water at a defined liquid content $W = 0.03$.

and attains very similar packing densities as of a completely dry glass bead pile above $P_{int} \gtrsim 10$ kPa. It is obvious that the internal cohesion due to emerging capillary bridges and other liquid structures is able to stabilize a wet granular assembly with a significantly lower packing density. Therefore, the relative difference between the stiffening pressures of dry and wet glass granulates at vanishing initial pressure should correspond to the capillary cohesion in wet bead assembly. In small initial pressure scale, i.e. $0 \lesssim P_{int} \lesssim 10$ kPa, the stiffening pressure of water-wetted granulates continuously increases due to the strong raise of the bead packing, since a sheared wet granular pile is highly 'compressible' as compared to dry granulates. At a sufficiently large

initial pressure $P_{int} \gtrsim 10$ kPa, it can be assumed that the externally applied stress (i.e. P_{int}) which increases the frictional impact between neighbouring glass granules, weakens the attractive internal cohesion due to capillary forces. Accordingly, the stiffening pressure P_{sp} is expected to increase linearly in the regime of large initial pressures, i.e. $P_{int} \gtrsim 10$ kPa. **Fig. 4.13** displays the X-ray radiographic images, captured of same dry and wet glass granulates as in **fig. 4.12** at different initial pressures. Experimental details of radiographic image acquisition are given in **section 5.2.1**. It is revealed from these radiographs that a wet bead pack as compared to its dry assembly can significantly be compactified for increasing granular stress (i.e. P_{int}) and consequently, it corroborates the positive correlation between the shear stiffness and packing density of the bead assemblies as found in **fig. 4.12**.

Qualitatively comparing individual slopes of the stiffening pressure data (P_{sp}) as obtained for dry glass granulates and water-wetted glass granulates in the regime of large initial pressure ($P_{int} \gtrsim 10$ kPa), it is revealed that the wet-friction is lowered around 16% as compared to the dry-friction; which is in good agreement with the expectation when we consider the relative difference between the friction coefficients of $\mu \approx 0.29$ and 0.25 (see **section 3.4**) found for dry glass surfaces and $Millipore$ water-wetted glass surfaces respectively. These experimental findings also suggest that liquid layers present on the bead-surfaces might be acting as a 'liquid lubricant' by diminishing the surface-friction at hard bead-bead contacts inside a sheared wet granulates.

For another wet glass bead pile, prepared by a water-glycerol mixture ($70:30$ wt.%) of surface tension $\gamma \approx 66.5$ mN/m [72] at room temperature, the qualitative behaviour of the stiffening pressure P_{sp} (cf. **fig. 4.11**) is very similar to the results of water-wetted glass granulates. Because of this particular wetting fluid's low surface tension and higher contact angles (see **section 3.2**) in compared to pure water, the effective capillary forces will be weak inside this wet glass granulates, wetted by the water-glycerol mixture ($70:30$ wt.%) and hence, its stiffening pressure is expected to be considerably small for very similar initial pressures. In the regime of small and large initial pressures, the slopes corresponding to P_{sp} data are obtained to be about 0.45 and 0.53 respectively. Comparing individual slopes of two distinct wet glass granulates, we find that the wet-friction in case of the wetting fluid: water-glycerol mixture ($70:30$ wt.%) is furthermore reduced around 24% than $Millipore$ water-wetted glass granulates; which suggests

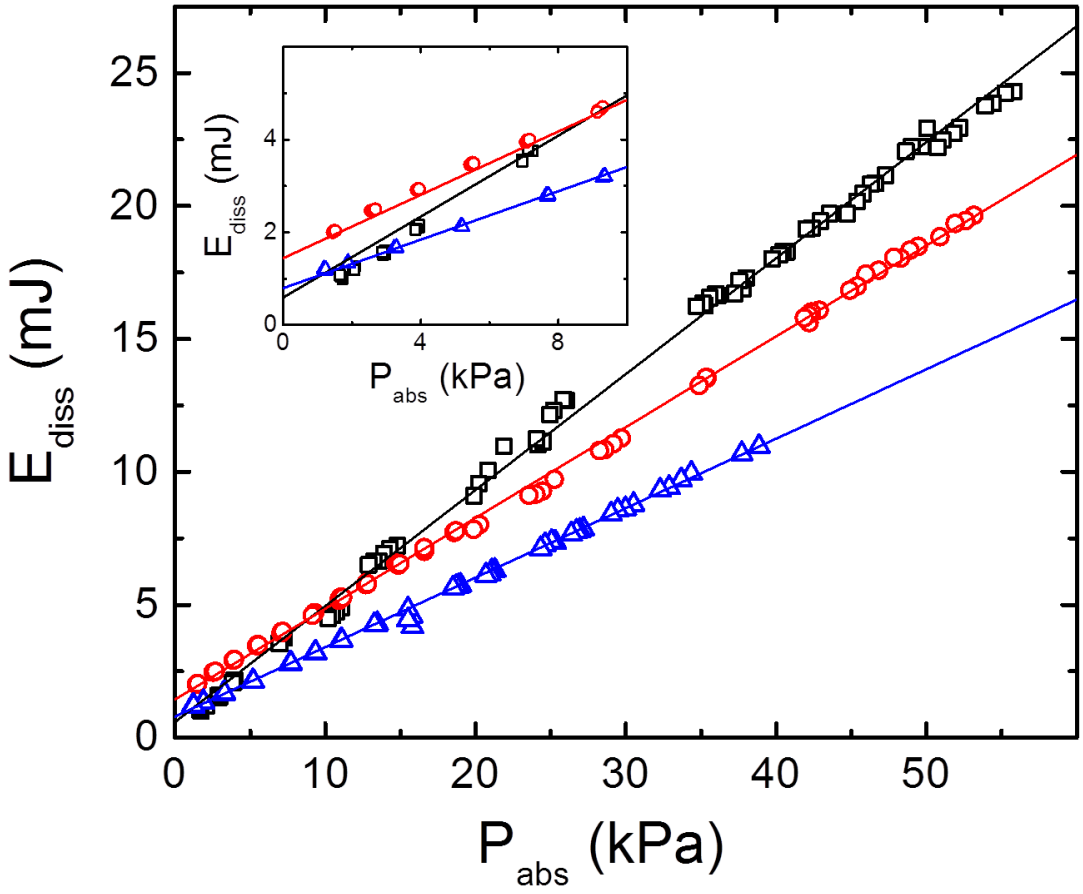

FIGURE 4.14: Energy dissipation (E_{diss}) during a complete shear cycle plotted as a function of the absolute pressure (P_{abs}) for dry glass granulates (open squares), a water-wetted glass bead assembly (open circles) and a glass bead pile, wetted by a water-glycerol mixture ($70:30$ wt.%) (open triangles). Inset: Same experimental data, but zoomed into a smaller absolute pressure scale for $0 \leq P_{abs} \leq 10$ kPa. Both wet granular samples prepared of a defined liquid content $W = 0.03$. Data obtained of same shear experiments as shown in **fig. 4.11**.

that the water-glycerol mixture ($70:30$ wt.%) of viscosity $\eta \approx 2.12$ mNs/m^2 [73] is a better lubricant. A smaller friction coefficient of $\mu \approx 0.23$ (see **section 3.4**) obtained for glass surfaces, wetted by a water-glycerol mixture ($70:30$ wt.%) also supports these experimental findings.

The energy dissipated during a full shear cycle should be proportional to the total area enclosed by the hysteresis loop, i.e. the characteristic Lissajous curve [59, 78] of differential pressure (ΔP) vs. volume displacement (ΔV) (cf. **fig. 4.5**). To account for the dissipated work-done, the energy dissipation (E_{diss}) as a function of the absolute pressure (P_{abs}) has been plotted in **fig.**

4.14 for dry glass bead pile and for two distinct wet glass granulates; which are obtained of same shear experiments as shown in **fig. 4.11**. It is interestingly observed that the dissipated energy (E_{diss}) increases linearly for gradually increasing absolute pressure (P_{abs}) for completely dry glass granulates (open squares) and two other wet granulates, i.e. a water-wetted glass bead assembly (open circles) and a glass bead pile, wetted by a water-glycerol mixture ($70 : 30$ wt.%) (open triangles). It is furthermore revealed (cf. **fig. 4.14**) that at almost vanishing absolute pressure (P_{abs}), the dissipated energy of water-wetted glass bead pile is relatively higher as compared to dry granulates. It possibly comes from the strong influences of the bridge-networks inside wet granulates. However, a gradual increase of the absolute pressure will result higher friction forces between shearing glass beads. As a result, a transition from 'capillary-force-dominated' regime to 'friction-force-dominated' regime is very much expected to be occurred. Comparing individual slopes of 0.44 (dry glass beads) and 0.34 (water-wetted glass beads), the dissipated energy (E_{diss}) associated with the water-wetted granulates is found to be around 23% smaller than that of a completely dry granular pile. In case of the water-glycerol mixture-wetted glass granulates, the corresponding slope is obtained to be about 0.26. Presumably, the wet-friction between glass granulates is significantly reduced for the higher viscosity (around 2.4 times more than pure water) of this particular wetting fluid and consequently, its energy dissipation is small as compared to that of water-wetted glass granulates for very similar absolute pressures.

5

X-ray Tomography Investigation of Sheared Wet Granulates

In recent days, 3D imaging of non-transparent materials with magnetic resonance imaging (known as MRI) or X-ray microtomography (also known as computed tomography) technique has created a great interest within various scientific communities. These techniques are mainly used for research and industrial purposes in different fields including medical science, geo-sciences, material science and also for basic scientific understandings. As standard optical techniques, such as particle image velocimetry (PIV), are not applicable in determining 3D flow behaviour of optically opaque grains, we will use the X-ray microtomography technique as a tool to explore the dynamic re-arrangement of granules and liquid re-distribution process for continuously sheared wet granular piles. The main advantage of X-ray microtomography is the high penetration of X-rays through the bulk materials. Moreover, the recent developments, in particular with high energy X-rays

at synchrotron radiation sources, allows in capturing 3-dimensional images with sufficiently high spatial and temporal resolutions. Potentially, the microtomographic results will provide us a better knowledge of the sheared wet granules, specifically on the pore level.

5.1 Experimental details

5.1.1 Radiographic imaging at micro-CT facility

X-ray radiographic experiments are conducted at our in-house μCT facility, equipped with '$CT-ALPHA$' machine from Procon-X-rays GmbH (Germany). A simple sketch of the experimental setup is shown in **fig. 5.1**. The diverging polychromatic X-ray beam, generated from a conventional X-ray tube of type: '$XWT-160-TC$' (from X-RAY-WorX GmbH, Germany) with

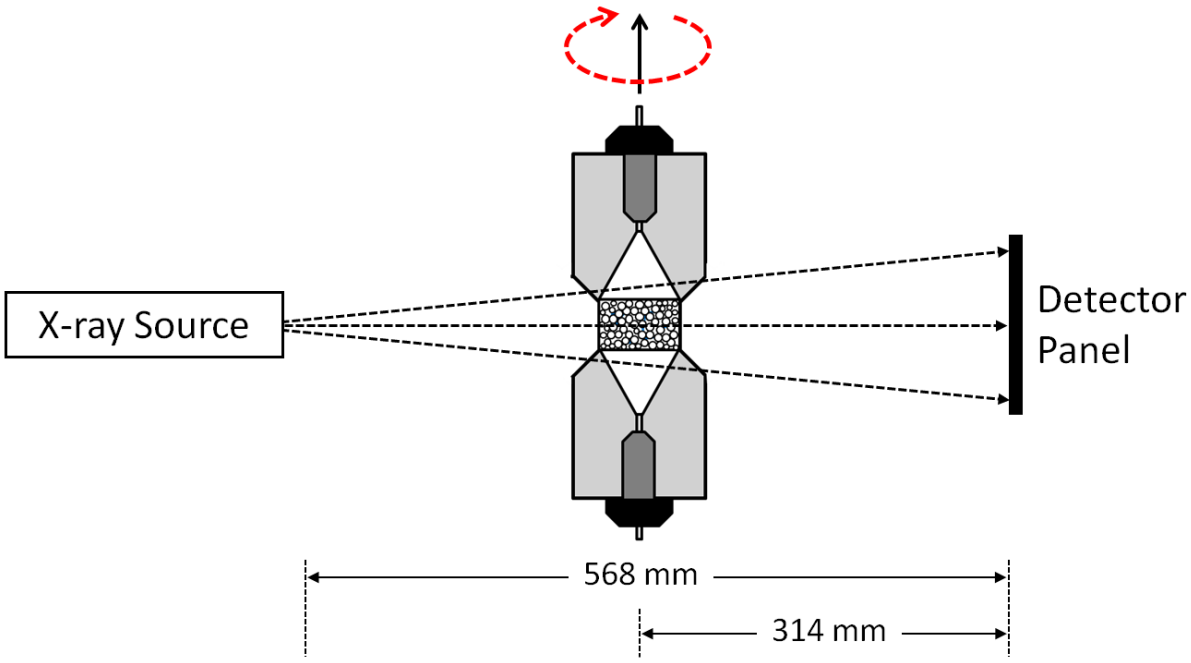

Figure 5.1: Schematic representation of our experimental setup, used for the X-ray radiographic imaging of dry and wet granulates. The diverging X-ray beam passes through the shear cell mounted on the rotation stage and subsequently, the attenuated X-rays are collected by a detector panel, placed behind the cell.

tungsten as an anode, penetrates through the shear cell, placed in the beam path and subsequently, the attenuated X-rays are collected with a detector panel, mounted behind the shear cell. The best material contrast with sufficiently large photon flux is achieved for an accelerating voltage ≈ 160 kV and the tube current ≈ 139 mA. The detector panel is a 12-bit CMOS camera (Model: $C7942SK-25$, Hamamatsu Photonics Corporation, Japan) combined with an efficient scintillator screen (gadolinium oxysulfide). The scintillating material converts the attenuated X-rays into visible light before it reaches to the camera. Due to conical shape of the beam profile, the geometric magnification of the shear cell can be adjusted. Following the same operating principle as explained in **section 4.1.2**, an initial pressure (P_{int}) is externally applied to the test granulates filled into the shear cell ($r = 15$ mm, $H = 10$ mm) and we thereafter capture a radiograph with an exposure time $t = 1000$ ms. The spatial resolution of the radiograph is about 14 μm/pixel. Thus, we have acquired the radiographic images of dry and wet glass granulates at different initial pressures; bead-sizes, wetting fluid and liquid content are the same as in **fig. 4.12**. A few selective rediographs are displayed in **fig. 4.13** earlier.

5.1.2 Tomographic imaging at synchrotron radiation source

X-ray microtomographic experiments are carried out at high energy X-ray beamline ID-15A, European Synchrotron Radiation Facility (ESRF), Grenoble (France). Our experimental setup at beamline ID-15A, ESRF is schematically shown in **fig. 5.2** (top). From an undulator source, the monochromatic parallel X-ray beam (energy ≈ 53.2 keV, beam width ≈ 8 mm) passes through the sample, mounted on a rotational stage in the X-ray beam. It should be mentioned that X-ray energies at around 53 keV are found to have (i) the best material contrast at minimum sample damage and (ii) sufficient photon flux. The rotational stage can continuously be rotated around the vertical Z-axis with high precision. The attenuated radiation from the sample is thereafter collected by an imaging system placed behind it. The imaging system consists of a scintillator screen, optics and a camera. The attenuated X-rays are converted into visible light by a high efficiency scintillator screen, LuAG: Ce (received from Crytur, Czech Republic) of thickness ≈ 250 μm. Subsequently, the light is focused to a camera by a magnifying $2\times-$optics. For our experimental needs, a PCO-Dimax camera (12 bit SCMOS camera system having full resolution:

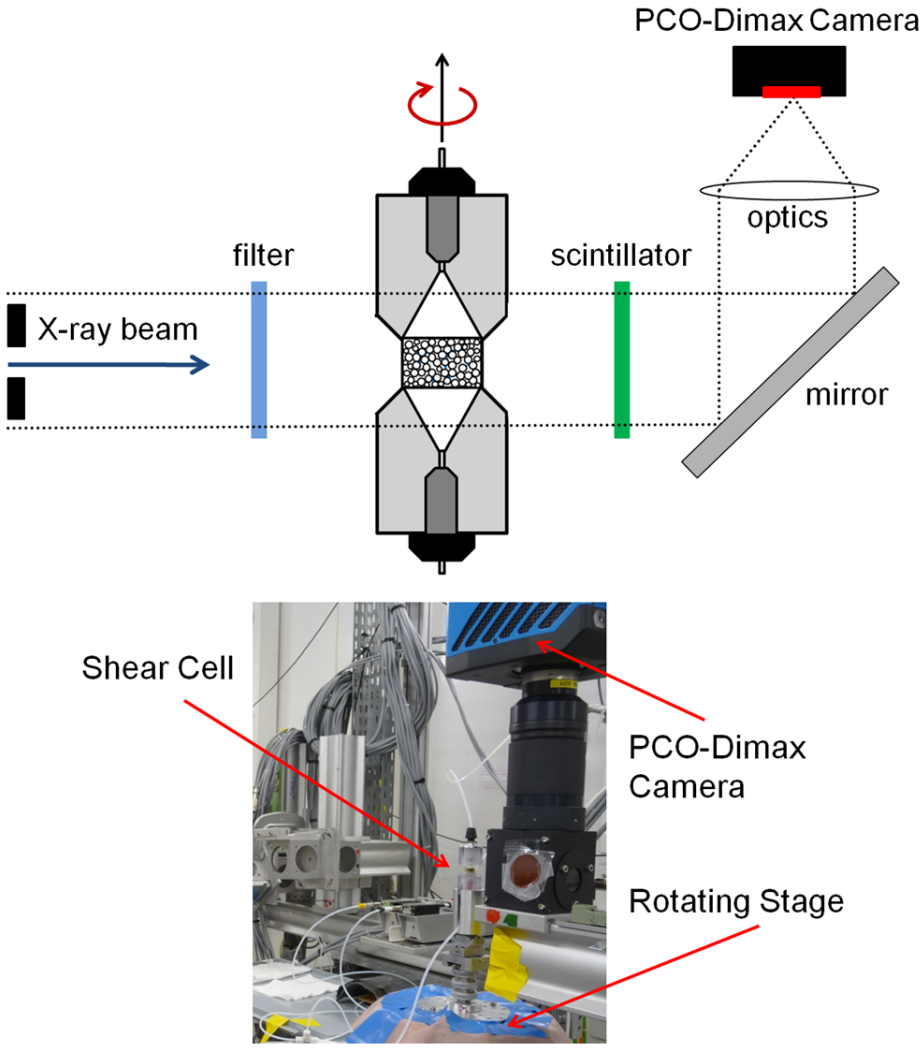

FIGURE 5.2: Schematic representation (top) and our actual setup (bottom) of the X-ray microtomography experiments at beamline ID-15A, ESRF, Grenoble (France).

2016×2016 pixel^2) is used to capture the tomographic images. This combination provides us a spatial resolution of 5.5 μm/pixel. In order to optimize the imaging time and photon counts, i.e. the signal-to-noise ratio, a PMMA block (acting as a filter) is placed in the X-ray beam before it reaches to the sample cell.

At first, wet granular samples are prepared with glass or basalt granulates (beads' sieve fraction: $250 - 300$ μm, $R \approx 141$ μm) and highly concentrated aqueous ZnI_2 solutions. Instead of pure water, an aqueous ZnI_2 solution is used as wetting fluid to increase the X-ray absorption. Hence, we are able to detect the minute liquid morphologies, appearing inside wet granulates.

In the following, image contrast experiments are extensively carried out by varying the solution-concentration over a wide range. The best images are obtained for an aqueous ZnI_2 solution of density $\approx 1.9-2.0$ g/ml, while different phases are well distinguished from each others. Therefore, these particular solution-concentrations are selected for our microtomographic experiments to be described in the following.

Our experimental setup at ID-15A, ESRF is displayed in **fig. 5.2** (bottom). The shear cell of this tomographic study is very similar to that one, used for the mechanical tests as mentioned in **section 4.1.2**. But, the size of this particular shear cell is reduced to fit to the dimension of the X-ray beam available at ID-15A, ESRF. At first, this small cell (inner radius $r = 4.0$ mm and height $H = 4.5$ mm) is loaded with test granulates, prepared of a well defined W and sealed at the opening ends. Subsequently, it is mounted on the rotational stage of the tomography-setup and a micro-positional sample alignment is performed in order to guarantee that the sample always stays in the beam during its continuous rotation. The operating principle of the shear deformation is the same as explained in **section 4.1.2** with $\Delta V_{max} \approx 33$ μl and $\Delta h_{max} \approx 621$ μm. Thereafter, 3D tomograms are recorded in successive time intervals *in-situ* during continuous shearing. With this ultrafast imaging technique, we are able to capture a full 3D tomogram within 3 or 6 seconds by capturing 2000 and 4000 projection images respectively while the shear cell is rotated by $180°$. It needs to be mentioned that the numbers of projections are selected by considering the required temporal resolution.

5.2 Tomographic image processing

5.2.1 Tomogram reconstruction and noise filtering

In the data-processing step, the tomographic reconstruction is performed by stacking 2D projection images into a 3D tomogram using a filtered back projection algorithm. In order to gain the computational resources and time, the reconstruction has been carried out at Linux based clusters of the ESRF, Grenoble. The typical reconstruction time of a single tomogram (volume size: $1485 \times 1485 \times 1100$ voxels) is about nine hours. A single reconstructed tomogram obtained as a gray scale image is about 9 GB. Afterwards, the noise-reduction treatment is applied to improve

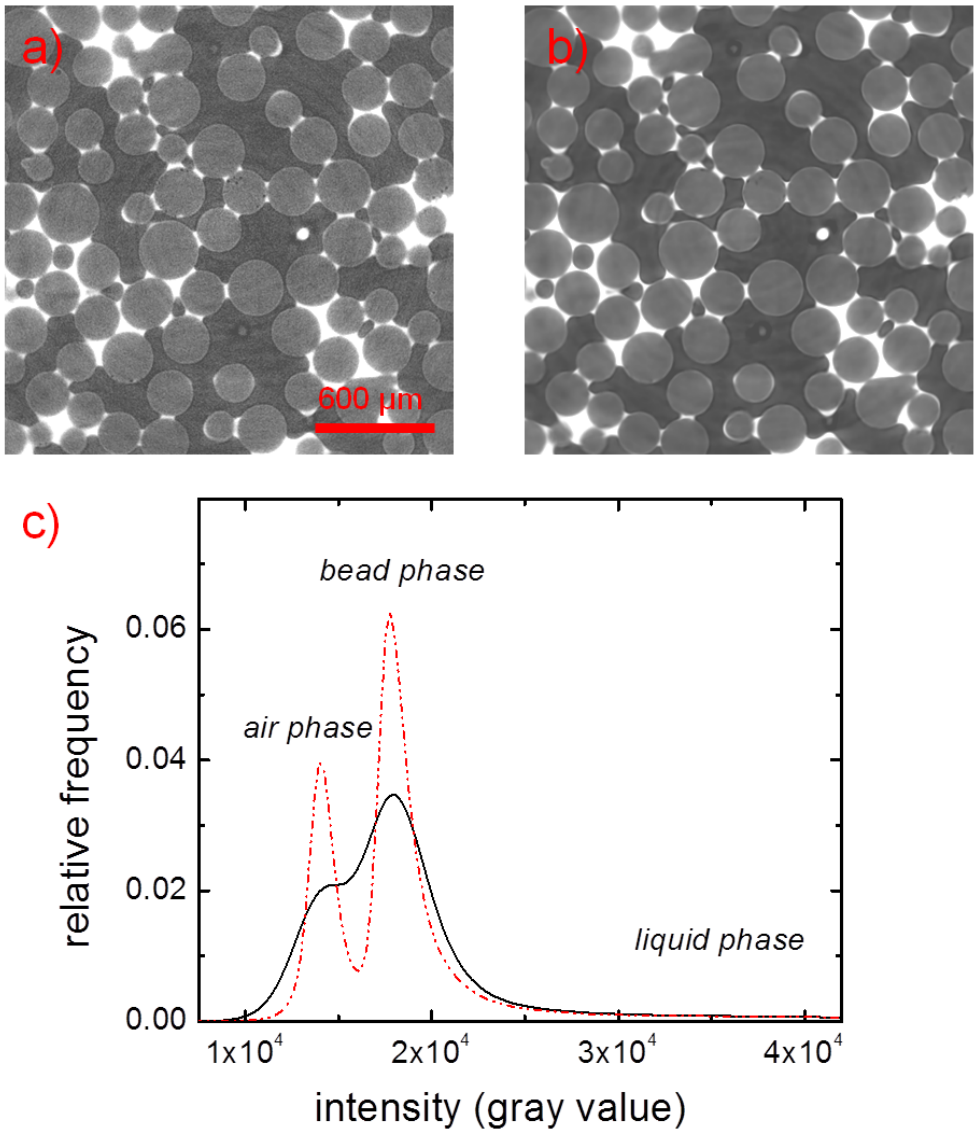

FIGURE 5.3: a) Raw and b) AD filtered images taken of a 3D tomogram. These 2D cross-sectional images are obtained for a wet granular sample, prepared with spherical glass beads (beads' sieve fraction: $250 - 300$ μm) and an aqueous ZnI_2 solution (seen as bright areas) at $W = 0.05$. c) Intensity histograms taken of the Raw (solid) and AD-filtered (dash dot) tomograms. It demonstrates that the SNR is significantly improved by applying the AD-filter routine to a Raw tomogram.

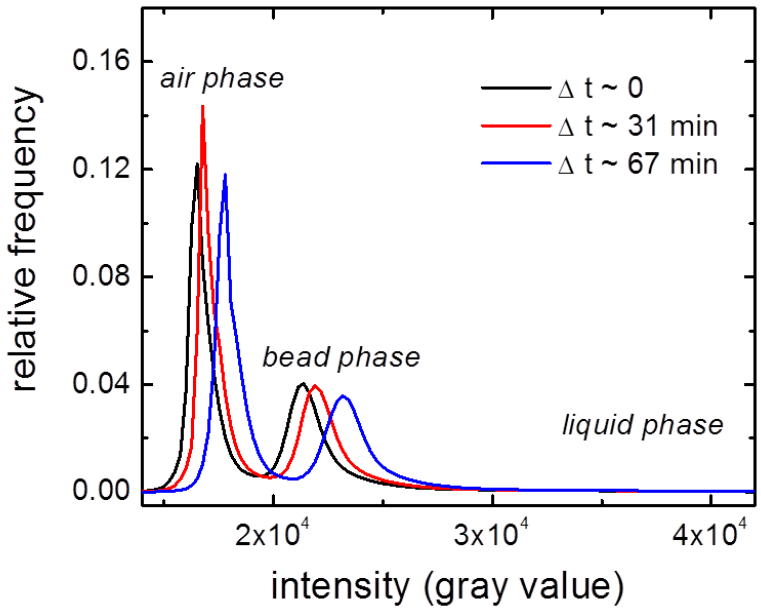

FIGURE 5.4: (Color online) Intensity histograms, obtained at different elapsed times (Δt) for individual AD filtered tomograms of wet basalt granulates. Bead-sizes, liquid content and wetting fluid are the same as in **fig. 5.3**.

the signal-to-noise ratio (SNR) of tomographic images. For edge-preserving image enhancement treatment, the anisotropic diffusion (AD) filter has emerged as a powerful tool in 3D signal processing than the wavelet transform filter [79]. Therefore, the 'AD-filtering' is employed for denoising the acquired 3-dimensional tomographic data. The post image processing treatments, staring from AD-filtering to segmentation of different phases, are performed with a software packages, called Mango [80]. The AD-filtering smoothes different phases of a gray scale tomographic image while the phase edges are well preserved. To select the best AD-filtering parameters, a small subset from a full tomogram is first taken and subsequently, the AD filter routine is applied. Once the satisfying image conditions are achieved, the full tomogram is processed by the AD filter routine with these selected parameters. Due to this large volumetric dataset, the AD-filtering of a full tomogram typically needs around seven hours. In **fig. 5.3** a & b, 2D cross-sectional images display a reconstructed (i.e. Raw) and its AD filtered tomograms respectively. These particular images are taken from a captured tomogram of wet glass bead assembly (beads' sieve fraction: $250 - 300$ μm, $W = 0.05$) where the wetting liquid, an aqueous ZnI_2 solution, is seen

as white areas. In **fig. 5.3**c, the corresponding intensity histograms illustrate different phases assigned by distinct gray values. It can be observed that the SNR is significantly improved to the AD filtered tomogram. It is also important to mention that the intensity fluctuation of the X-ray beam (resulted due to varying electron density and electron distribution in the synchrotron storage ring) is observed over the elapsed time scale. In **fig. 5.4**, the intensity histograms of AD filtered tomograms at different times (Δt) demonstrate this intensity fluctuation; these results are obtained of basalt granulates, wetted by an aqueous ZnI_2 solution at $W = 0.05$.

5.2.2 Phase segmentation and qualitative data analysis

For the qualitative data analysis, the phase segmentation of an AD filtered tomogram is particularly needed. The segmentation method is to classify a gray scale tomographic image into distinct binary images which are assigned to different phases in accordance with the X-ray absorption. In the context of phase segmentation, the 'converging active contour' (CAC) approach, watershed transform and traditional 3-phase segmentation filter routines are considered as the most popular methods [79, 81]. In order to segment bead, air and liquid phases from each others, we have employed a two-stepped CAC filter routine which is intrinsically faster and less noise sensitive. At first, the liquid phase is separated, followed by the bead phase from air phase.

Prior to apply segmentation routines, the 'geometric mask' (GM) filter is first applied to the AD filtered tomogram; which cuts out undesirable cylindrical boundaries to make its influences insensitive to further image processing steps. Subsequently, the best CAC threshold parameters are optimized using a small subset of the AD filtered tomogram. This means that the voxels having higher intensity values than the threshold will be assigned as liquid phase whereas the voxels having lower values than the threshold will remain as rest, containing air and bead phases together. Once the liquid-phase-segmentation parameters are selected; a second CAC filter routine is applied to segment the bead phase from air. When the best bead-phase-segmentation parameters are obtained from our segmentation tests, these selected parameters are implemented into the segmentation filter routines for segmenting the full tomographic image. A careful selection of the thresholding parameters is of a great importance, because a small-changes in selecting the segmentation parameters may lead to erroneous segmented results and consequently, some

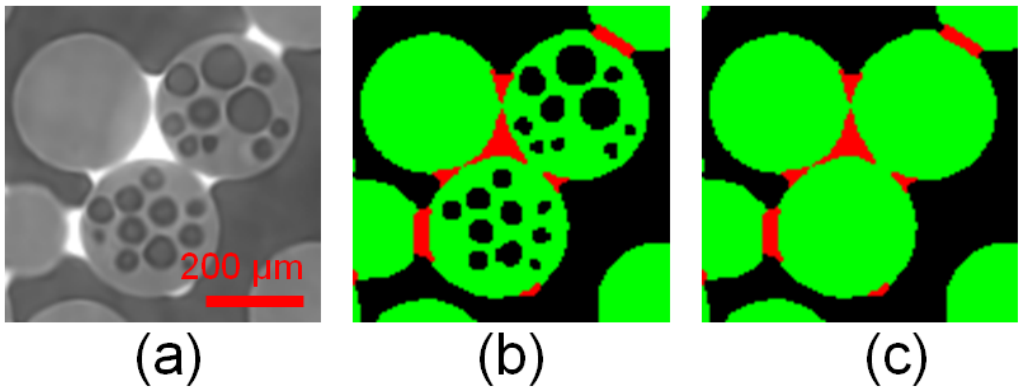

Figure 5.5: (Color online) a) Gray scale AD filtered image; b) segmented image: liquid, bead and air phases are seen as red, green and black coloured areas respectively; bead-cavities are also assigned as air phase. c) Corrected segmented image: bead-cavities which have been initially segmented as air phase, are removed and properly assigned as bead phase. Scale bar applies to all three images.

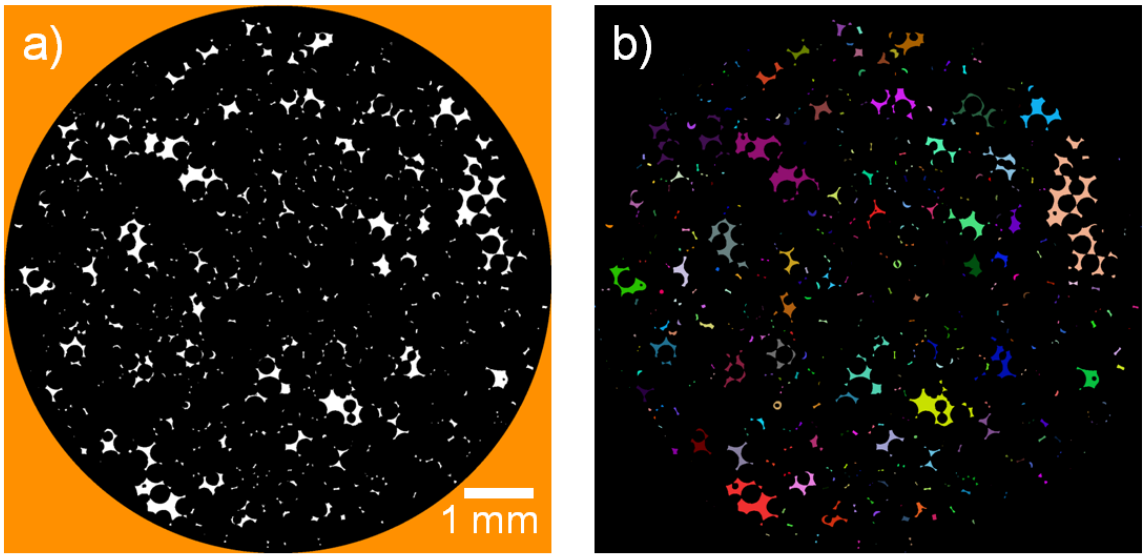

Figure 5.6: (Color online) a) Segmented liquid phase (seen as bright areas) and b) individual liquid structures (labelled with different colours) as obtained from the segmented tomogram. Scale bar applies to both images.

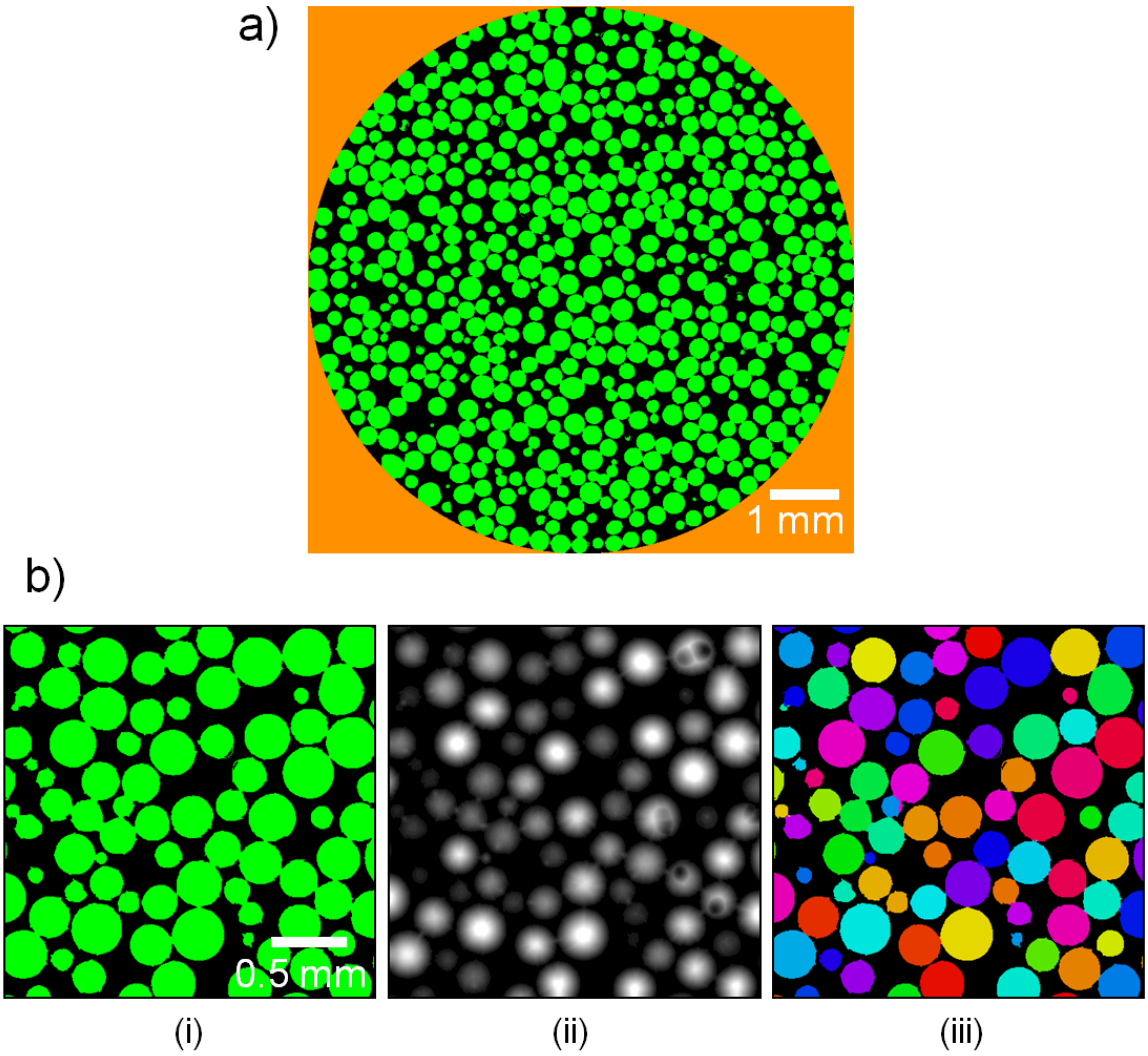

Figure 5.7: (Color online) a) Segmented bead phase shown as green coloured circles. Black area contains liquid and air phases together. b) A series of images demonstrating the image processing steps, used for separating individual beads. In images (i) & (ii), the segmented bead phase and its 'euclidean distance map' are shown. The image (iii) depicts the separated beads, labelled with distinct coloured circles. Scale bar applies to all three images.

microscopic features could significantly be lost. As articulated in the previous section, the varied intensity-profile of consecutive tomograms sometimes made it much difficult to achieve the proper segmentation parameters. It should be addressed that there is no universality in selecting the threshold parameters. For the best possible segmentation, the threshold parameters are decided as accurate as possible. Some particular beads, having holes or cavities, made it difficult to

properly segment the bead phase. More specifically, the bead-cavities are considered as air phase due to its low X-ray absorption. The major challenge is to improve the segmented bead phase; which is performed with a combination of multiple image treatment steps. In the following, the bead-cavities, initially assigned as the air phase, are finally obtained as bead phase. The above description is visualized in **fig. 5.5**. The gray scale AD filtered image and its segmented phases are shown in **fig. 5.5** a & b, where the red, green and black colours are assigned to the liquid, bead and air phases respectively. The image in **fig. 5.5**c displays the segmentation tomogram in which the bead-cavities are corrected and properly assigned as bead phase. In **fig. 5.6**a, 2D cross-sectional image, obtained by following the above mentioned image processing steps, depicts a fully segmented liquid phase, and distinct liquid structures labelled with different colours are displayed in **fig. 5.6**b. Similarly, a fully segmented bead phase is displayed in **fig. 5.7**a. To identify individual beads and their positional information, the segmented bead phase tomogram is further treated with different analyzing filters, provided by the software packages of Mango toolkit. For this reason, the 'euclidean distance map' routine, followed by the 'distance map

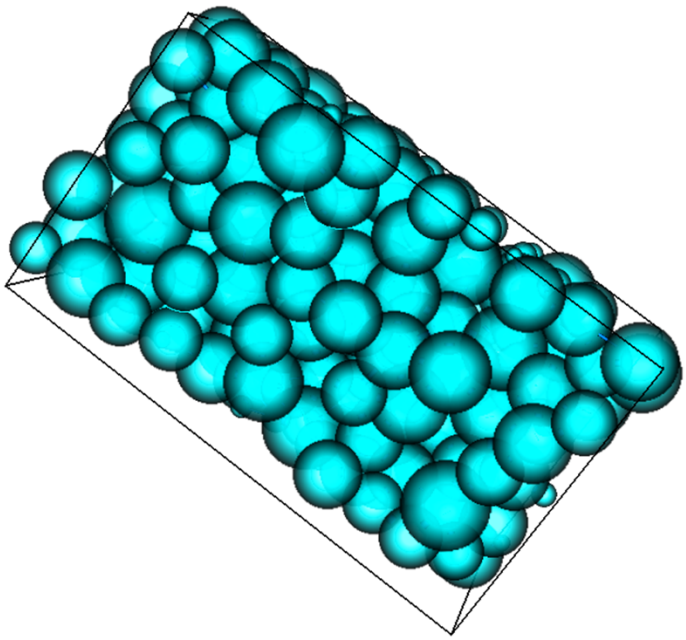

FIGURE 5.8: Local grain-geometry inside a wet glass bead pile (beads' sieve fraction: $250-300$ μm, $R \approx 141$ μm, $W = 0.05$).

watershed' and 'region merging' routines, is subsequently applied to the segmented bead phase tomogram.The images in **fig. 5.7**b visually explain this description: a segmented bead phase and its euclidean distance map are shown in **fig. 5.7**b (i) & (ii) respectively, whereas the coloured circles as seen in **fig. 5.7**b (iii) display individual beads. All further analyses of these segmented tomograms are performed with various inbuilt algorithms of the Mango software and the custom made Matlab^{TM} programs. In such a way, we obtain the statistics of emerging liquid structures' volume and surface area as well as the packing fraction (ρ) of bead assemblies. In addition, a 3D volume rendering software, called 'Drishti' [82] is used to visualize distinct liquid morphologies, found inside wet bead assemblies. **Fig. 5.8** visualizes the contact network of spheres within a wet glass bead assembly (beads' sieve fraction: $250 - 300$ μm, $R \approx 141$ μm, $W = 0.05$).

5.3 Experimental results and discussion

5.3.1 Liquid distribution inside static wet bead assemblies

In **fig. 5.9** a & b, 2D cross-sectional images are taken from 3D tomograms, recorded of wet glass and basalt bead assemblies (bead diameter: $250 - 300$ μm) at a liquid content of $W = 0.05$. The wetting fluid, an aqueous ZnI_2 solution, is seen as bright areas in these gray scale images. With careful inspection of tomographic images, it is found that the liquid and air phases quite homogeneously coexist within a wet glass bead pack by forming delicate liquid geometries. In contrast to wettable glass granules, the liquid inside a wet basalt bead assembly prefers to stay in large liquid structures due to its low wettability. For similar type of data analysis as presented in

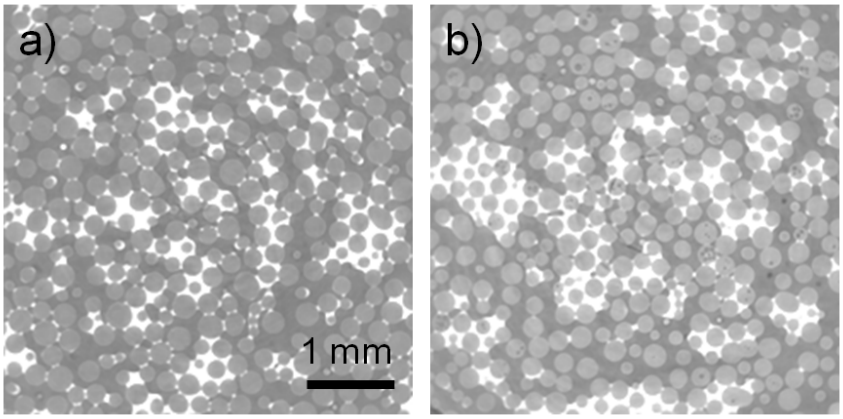

Figure 5.9: 2D cross-sectional images taken from 3D tomograms of a) wet glass and b) wet basalt bead assemblies (bead diameter: $250 - 300$ μm, $W = 0.05$). Air and bead phases are displayed as black areas and grey circles respectively, while the liquid phase (aqueous ZnI_2 solution) is seen as white areas. Scale bar applies to both images.

ref. [39, 48, 49], individual liquid structures are found to be characterized by their total surface area and liquid volume. It is also revealed that our wet granulates are governed by the open liquid morphologies as discussed in **section 2.2.1**. In **fig. 5.10**, different liquid structures which are experimentally found within a wet glass bead pile, are very identical to distinct liquid shapes as displayed in **fig. 2.5** earlier. In **fig. 5.10**, the images visualize a capillary bridge, trimer, pentamer, tetrahedral domain, heptamer and other liquid structures, appearing due to the fusion process of capillary bridges and small liquid clusters.

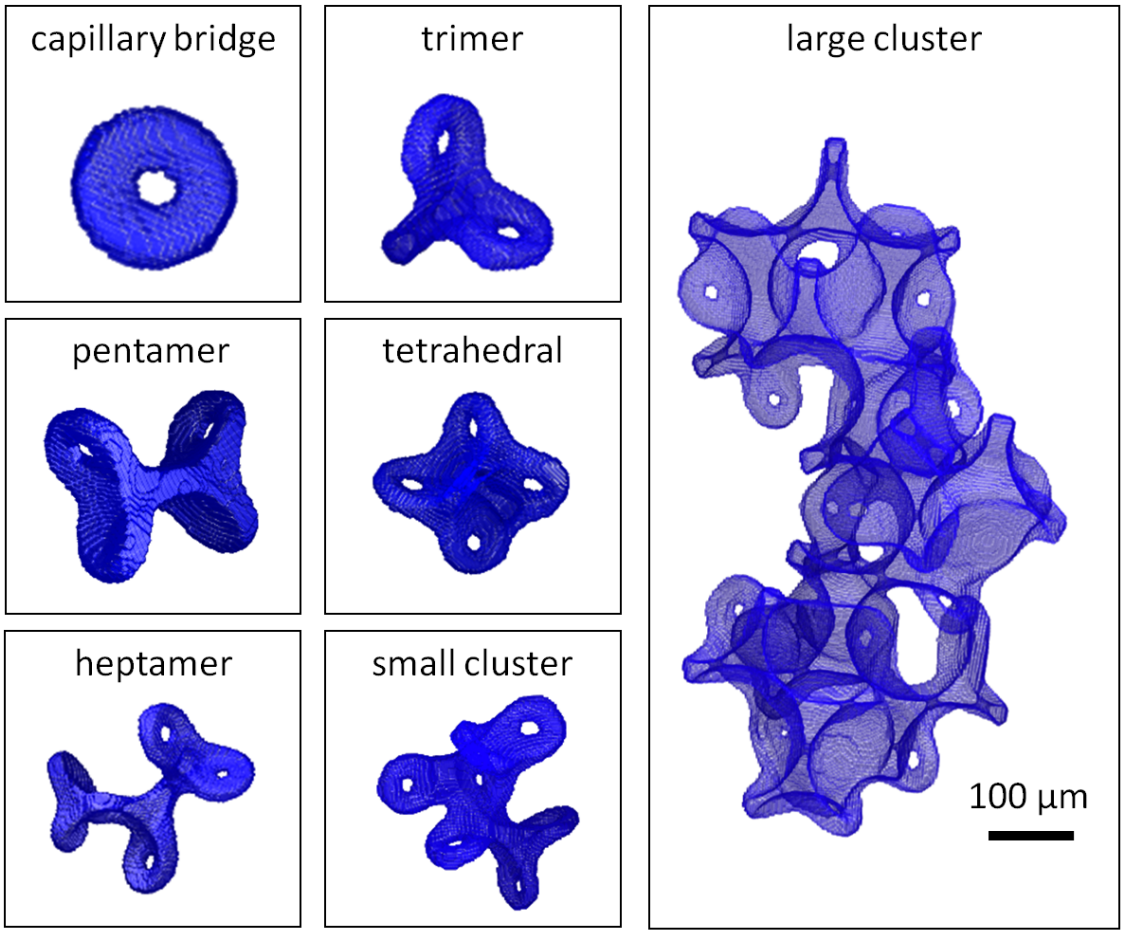

FIGURE 5.10: Different liquid structures as found within a wet glass bead pile (beads' sieve fraction: $250 - 300$ μm, $W = 0.05$) with X-ray microtomography. In these images, a capillary bridge, trimer, pentamer, tetrahedral cluster and heptamer and other liquid morphologies are displayed. A large liquid cluster is comprised of capillary bridges and small liquid clusters.

5.3.2 Dynamic aspects of sheared wet granulates

In order to understand the mechanical findings as discussed in **section 4.2.2**, the shear process with wettable glass granulates is recorded by the time resolved ultrafast X-ray microtomography at two different shear rates of $\gamma' \approx 0.5 \times 10^{-4}\ s^{-1}$ and $2.5 \times 10^{-4}\ s^{-1}$ respectively. The faster shear run has a periodicity of $T \approx 42$ min whereas for the slower run, approx. 222 min are needed to complete a full shear cycle. Keeping all other parameters constant, similar shear experiments have also been conducted for less-wettable basalt granulates. Some 2D cross-sections from 3D tomograms at distinct positions of an entire shear cycle are displayed in **fig. 5.11**, for a fast shear run of wettable glass granulates at an absolute pressure of $P_{abs} \approx 6$ kPa. As can be seen,

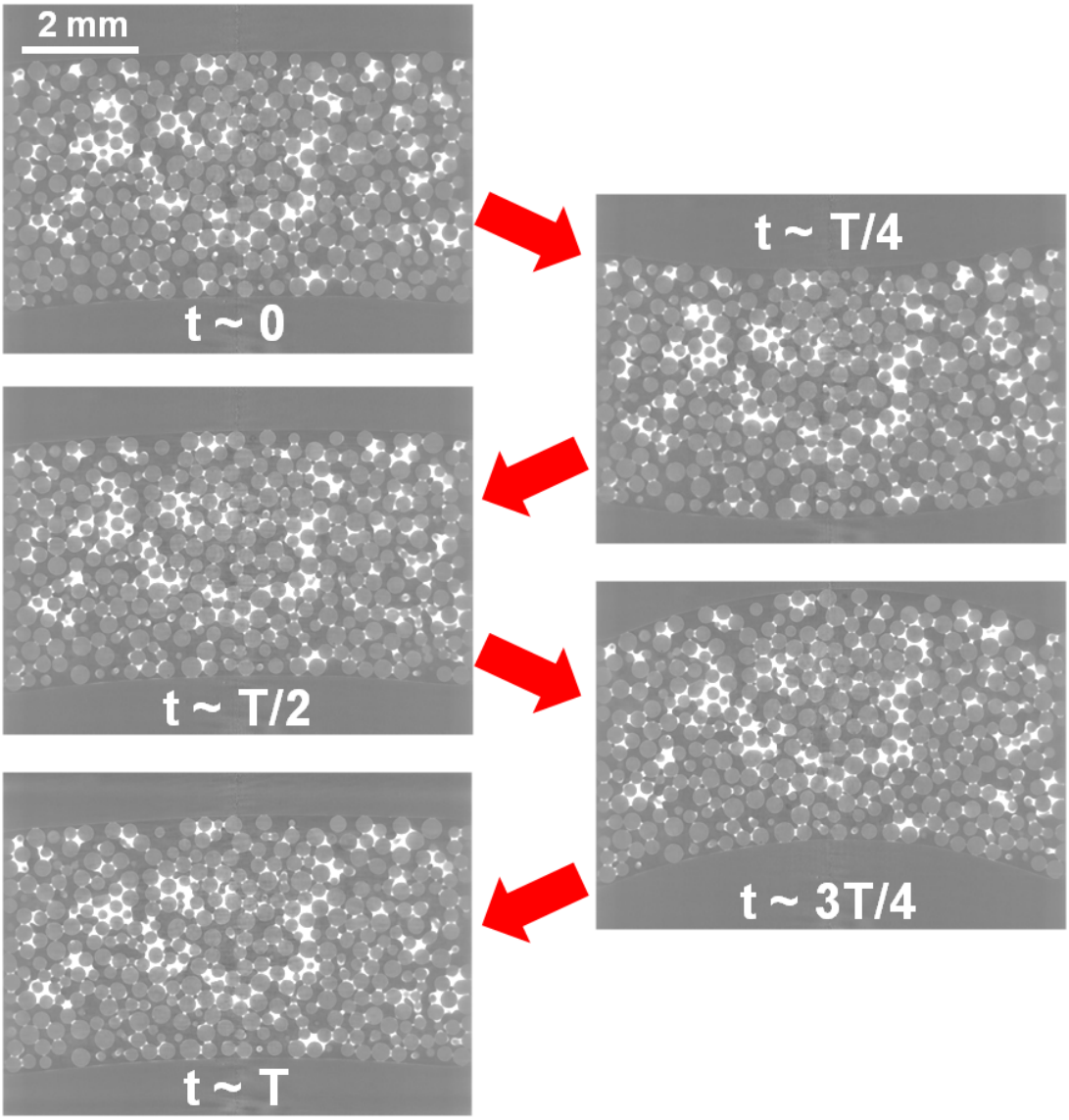

Figure 5.11: 2D cross-sectional images taken from 3D tomograms at distinct positions of a full shear cycle for wet glass granulates (beads' sieve fraction: $250 - 300$ μm, $W = 0.05$). The shear periodicity $T \approx 42$ min and the corresponding shear rate $\gamma' \approx 2.5 \times 10^{-4}$ s^{-1}.

individual beads have larger spatial displacements in the central region of the cylindrical cell due to parabolic shear profile. To resolve the 'grain reorganization process', the position of individual beads and their relative displacements for continuous shearing are determined by tracking the bead-centres from consecutive 3D tomograms. In **fig. 5.12**a, colour coded azimuthally averaged bead-velocities are obtained for the same shear experiment as shown in **fig. 5.11** above. The

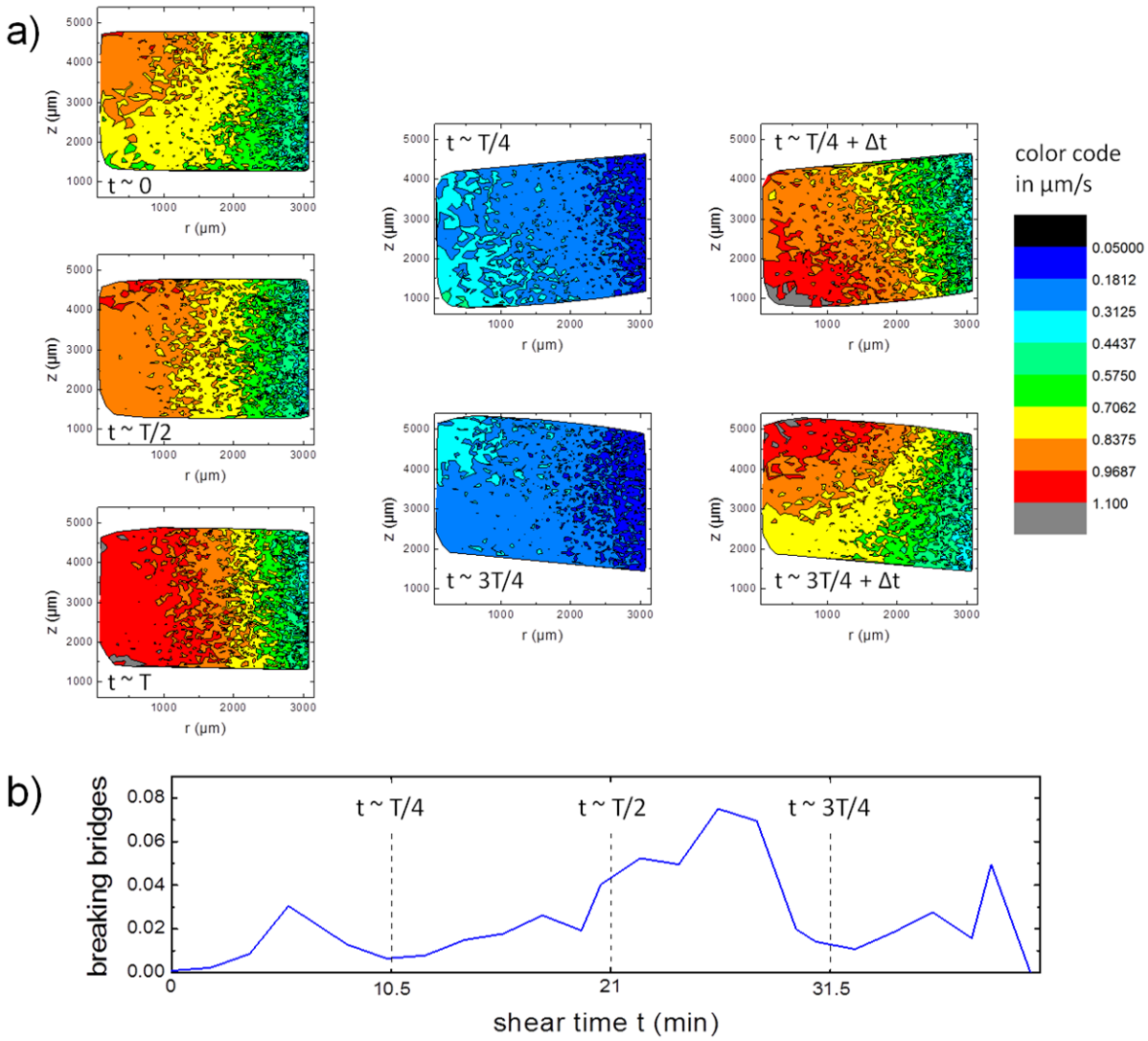

FIGURE 5.12: a) Color coded velocity profile of sheared glass beads at distinct shear positions, extracted of same tomographic experiments as shown in **fig. 5.11**; here $\Delta t = 1.86$ min. b) Average number of ruptured liquid bridges per bead as a function of the shear time (t) for the same shear run. Data prepared by Anna-Lena Hippler together with Marc Schaber.

left and right sides of each panel correspond to the centre and outer boundary of the cylindrical shear cell. One certainly observes in **fig. 5.12**a that individual beads at turning points, i.e. at $t \approx T/4$ and $3T/4$, have almost zero velocities as expected. In addition to these findings, a certain compressibility of the granulates is interestingly observed, right after the inversion of the shear direction, i.e. at $t \approx T/4 + \Delta t$ and $3T/4 + \Delta t$ where $\Delta t = 1.86$ min. While wet granulates

are cyclically shearing, individual beads continuously change their positions. Therefore, one would also expect that some of the capillary bridges and other liquid clusters might break and/or reform in later time. Since an isolated liquid bridge cannot sustain for a maximum bead separation, larger than the critical rupture distance (S_c), the effective separation between the reference bead and its nearest neighbours has been analysed. From **fig. 5.12**b which displays the average number of breaking bridges per bead as a function of the shear time (t), it is interestingly revealed that a few percentages (less than 8%) of the liquid bridges only break during continuous fast shearing.

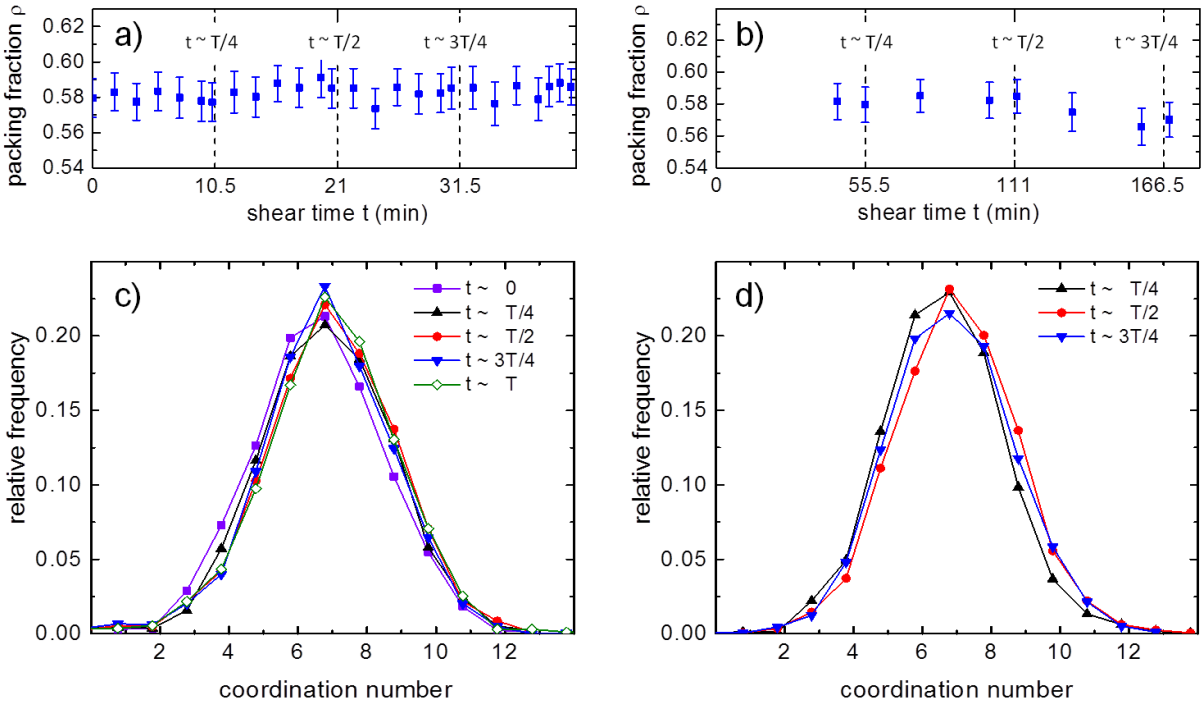

FIGURE 5.13: (Color online) Packing fraction (ρ) of spherical glass bead matrix, plotted as a function of the shear time (t) for a) fast and b) slow shear runs respectively. Distribution of the coordination number pre bead, corresponding to same c) fast and d) slow shear runs. Distinct shear positions are indicated in terms of the periodicity T.

To find out the correlation between the local bead-arrangements and global packing, the packing fraction of spherical glass granulates has been studied. As can be seen in **fig. 5.13** a & b, the average packing fraction (ρ) plotted as a function of the shear time (t) is around (0.58 ± 0.02) for both shear runs. For the slow shearing, a small drop of the packing fraction at a time $t \approx 3T/4$ is due to certain experimental failures. Nonetheless, the resulting bead-packing

is noticeably small in compared to the random close packing limit (≈ 0.64 [29]) which is the largest possible random packing fraction of frictionless spheres. Such a low packing density for wet glass bead packs is most likely attained due to the presence of delicate liquid structures between the individual beads. Within large experimental scatters, the packing fraction ρ (itself slightly varying over the shear time) however does not proof the granular compressibility as seen in **fig. 5.12**a. In the following, the coordination number (i.e. the average number of neighbouring beads in contact with the reference bead) has been estimated. For fast and slow shear runs, the coordination number is obtained to be about 6.8; it can be observed in the statistical distributions of the coordination number as displayed in **fig. 5.13** c & d. All these findings are independent on the precise choice of the shear position. A certain width of the distributions and such a higher bead-coordination might be attributed due to the bead-asphericity (≈ 1.02) and poly-dispersity (i.e. $\frac{\delta R}{R} \approx 10\%$) of the glass microspheres. However, the resultant coordination number is much small as compared to the highest achievable theoretical limit, i.e. 12 neighbours in physical contacts for a compact assembly of monosized frictionless spheres [37, 40].

Since the liquid bridges hardly break during continuous shear deformation (cf. **fig. 5.12**b), distinct liquid morphologies are presumed to change their volumes and sizes for adopting equilibrium shapes of lowest free surface energies. To unravel this analogy, we have studied the distribution of emerging liquid structures' volumes, normalized by R^3. In **fig. 5.14** a & b, histograms of normalized liquid volumes are displayed for wettable glass beads at two different shear runs. In case of the slow shearing, histograms in **fig. 5.14**a resemble the equilibrated liquid distribution as discussed in **section 2.2.2**. With careful observation, it is recognized that distribution-peaks are maximized at a normalized liquid volume $V/R^3 \approx 0.58 - 0.06$; which is in good agreement with the theoretical prediction for a largest possible capillary bridge's maximum liquid volume [39, 48, 49]. Unlike the slower run, histograms of normalized liquid volumes (cf. **fig. 5.14**b) have a continuous decaying distribution for a fast shearing, conducted with same wet glass granulates. Such histograms are very similar to the liquid distribution as observed for a wet glass bead assembly - right after stopping the fluidization (cf. **fig. 2.6**a). In both shear cases, a volume redistribution process, occurring between individual liquid morphologies, is noticed while closely inspecting these resultant histograms, obtained at different shear positions of the individual shear cycle. Clearly, the volume redistribution process which is strongly influenced by the applied shear

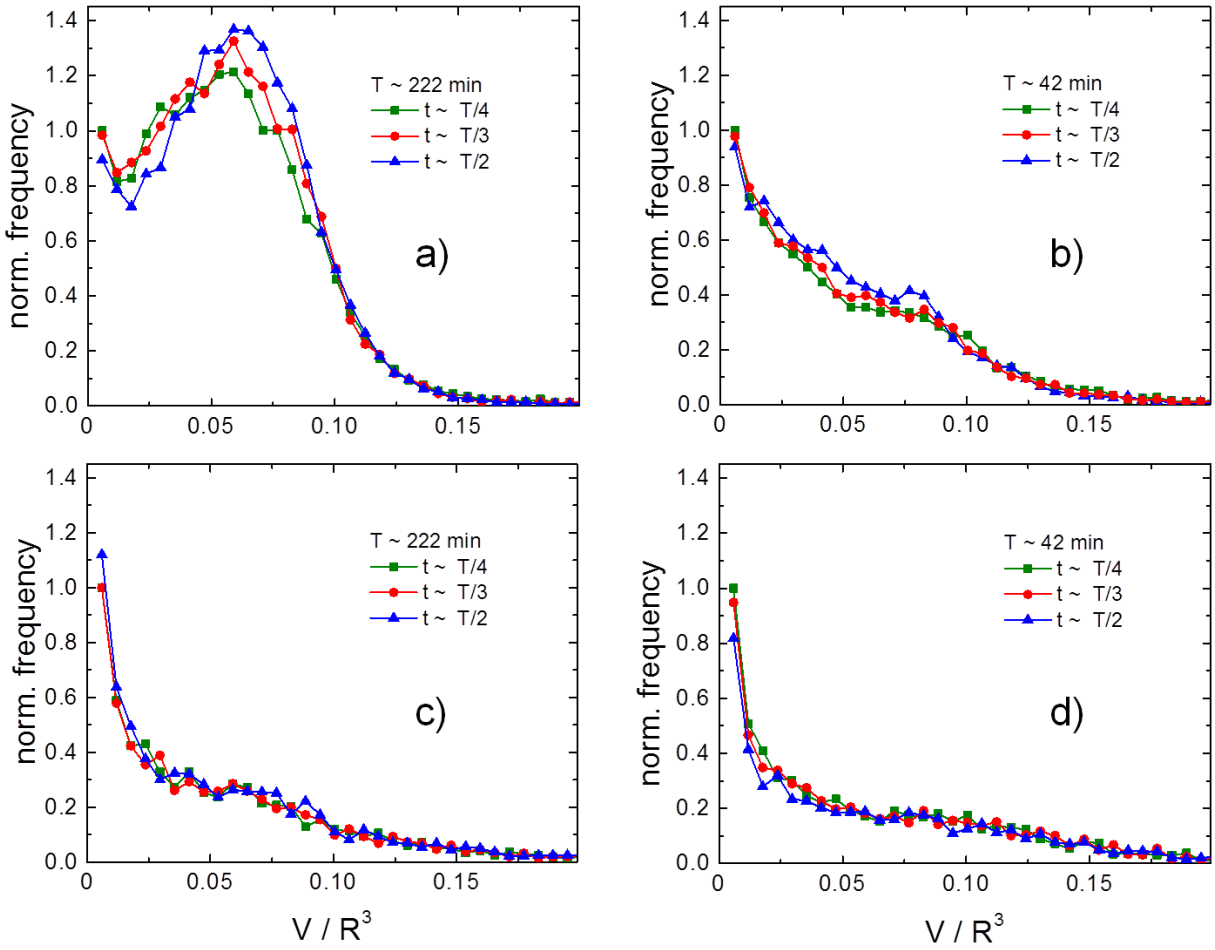

FIGURE 5.14: (Color online) Histograms of emerging liquid structures' volumes obtained at distinct positions for sheared wet bead assemblies (beads' sieve fraction: $250 - 300$ μm, wetted by aqueous ZnI_2 solution at $W = 0.05$). Graphs in a) and b) are resulted for slow and fast shearing of wettable glass granulates. Graphs in c) and d) are obtained with less-wettable basalt granulates for slow and fast shear runs. The notation T denotes the periodicity of respective shear cycle.

rate, will affect the temporal evolution of individual liquid structures. Presumably this is why, the shear rate dependence of stiffening pressure (P_{sp}) has been observed for wet glass bead assemblies (cf. **fig. 4.9**a). For very similar type of data analysis, histograms of normalized liquid volumes at distinct shear positions are shown in **fig. 5.14** c & d, for slow and fast shear runs of less-wettable basalt granulates respectively. In both cases, distribution curves are very similar to the histograms of emerging liquid volumes what have been found in the fluidization experiments, conducted with wet basalt granulates (cf. **fig. 2.7**). In strong contrast to wettable glass beads,

the distribution curves of liquid volumes for wet basalt bead packs do not vary at different shear positions - neither for the slow nor for the fast shear run; which firmly denotes that there is no temporal evolution of appeared liquid structures inside sheared wet basalt granulates. A direct comparison between these two distinct wet granular systems of different wettability unravels that the wetting fluid inside a sheared wet glass bead pile advances through thin liquid films covered on the bead-surfaces, not via the gas phase. Otherwise, a similar liquid redistribution must have resulted for wet basalt bead assemblies. Based on these qualitative analyses, we assume that for less-wettable basalt granulates, the non-existing liquid exchange process governs the resulting mechanical stiffness (i.e. P_{sp}), almost unchanged on the applied shear rate scale (cf. **fig. 4.9**b).

6

Summary

In summary, different mechanical properties of dry and wet granulates are investigated during the course of my research work. In this thesis, we have reported a series experiments, performed to capture the comprehensive description of granular-flow under continuous shear deformation. By characterizing surface properties of granular materials, we have found that basalt microspheres have a large contact angle hysteresis as compared to wettable glass granulates and exhibit non-wetting characteristic features.

From our mechanical results of wettable glass and non-wettable basalt granulates, the characteristic dependence of shear stiffening (P_{sp}) as obtained for various liquid contents (W) is demonstrated in terms of effective capillary bridge forces as exerted by liquid-contacts present between the neighbouring spherical particles; which is also in good agreement with other mechanical properties like yield stress or critical acceleration as published in ref. [25, 48]. However, the mechanical stiffness of a sheared wet granular assembly is determined by the receding contact

angle of wetting liquid on the material-surfaces.

For increasing applied stress (i.e. P_{int}), a sheared wet granular assembly is found to be more compressible than a dry granular pile. However, the bead-packing either in dry or wet granulates acquires almost similar values above a certain threshold of the initial pressure, externally applied on these distinct bead samples. We have also verified this compaction dynamics by visualizing the test granulates with X-ray radiographic imaging. At a significantly large applied stress, the shear stiffness and dissipated energy of a sheared wet granular assembly are found to be comparatively small with respect to its dry granular pack. These phenomena have occurred due to the presence of wetting fluids which might act as a 'liquid lubricant' by diminishing the frictional impact at hard bead-contacts in wet granulates.

At various liquid contents (W) for $0.01 \leq W \leq 0.05$, the shear stiffening of wettable glass granulates is observed to depend noticeably on the applied shear rate. In contrast to wettable glass bead samples, the shear stiffening of non-wettable basalt granulates is largely insensitive on the shear rate scale, for very similar liquid contents. To resolve this, the shear process of wet (glass or basalt) granulates has been recorded with ultrafast X-ray microtomography *in-situ* during continuous shearing. The dynamic behaviour of liquid structures and bead-packing as a function of the shear time (t) are characterized by analyzing the captured tomograms. It is revealed that there is a liquid exchange process, occurring between distinct liquid morphologies inside sheared wet glass granulates and the evolution dynamics are strongly influenced by the applied shear rate. Thus, the volume redistribution within a sheared wet glass bead pile is the key factor for the rate dependence of its shear stiffening as observed in our mechanical studies. Unlike wettable glass granulates, no such temporal evolution of distributed liquid volumes is observed for non-wettable basalt granulates, continuously shear-deformed. Hence, the non-existing liquid exchange mechanism inside wet basalt bead packs might attribute its mechanical stiffness which is almost invariable on the applied shear rate. Moreover, a direct comparison between wet glass and basalt granulates also reveals that the liquid redistribution within a sheared wet glass bead sample is advancing through thin liquid layers adsorbed on the bead-surfaces. In addition, the proposed 2D model indicates that a long distance liquid transport mechanism should govern the liquid equilibration dynamics in a cyclically sheared wet granular pile; this description can be confirmed with simple shear experiments using X-ray microtomography as a imaging tool.

References

[1] R. M. Nedderman, *Statics and Kinematics of Granular Materials* (Cambridge University Press, Cambridge, 1992).

[2] A. Mehta, *Granular Physics* (Cambridge University Press, Cambridge, 2007).

[3] H. Hinrichsen and D. E. Wolf, *The Physics of Granular Media* (Wiley-VCH Verlag GmbH & Co., Weinheim, Germany, 2004).

[4] S. J. Antony, W. Hoyle, and Y. Ding, *Granular Materials - Fundamentals and Applications* (The Royal Society of Chemistry, Cambridge, UK, 2004).

[5] G. Ristow, *Pattern Formation in Granular Materials* (Springer-Verlag, Heidelberg, Germany, 2000).

[6] P. Schiffer, Nature Physics **1**, 21 (2005).

[7] P. G. de Gennes, Rev. Mod. Phys. **71**, S374 (1999).

[8] H. M. Jaeger, S. R. Nagel, and R. P. Behringer, Rev. Mod. Phys. **68**, 1259 (1996).

[9] L. P. Kadanoff, Rev. Mod. Phys. **71**, 435 (1999).

[10] S. R. Nagel, Rev. Mod. Phys. **64**, 321 (1992).

[11] S. Sepp, Wooden Hourglass, http://commons.wikimedia.org/wiki, (2007).

[12] P. Weiss, Germany, Sandcastle, (2012) (personal communication).

[13] R. L. Schuster, Landslide Hazards, Department of the Interior, US Geological Survey, USA, (1995).

[14] H. Fukuoka, S. Kyoji, and W. Gonghui, Landslides **4**, 63 (2007).

[15] W. J. Godt, R. L. Baum, and N. Lu, Geophysical Reserach Letters **36**, L02403 (2009).

[16] T. L. Gipprich, R. K. Snieder, R. W. Jibson, and W. Kimman, Geophys. J. Int. **172**, 770 (2008).

[17] H. J. Herrmann, Physica A **313**, 188 (2002).

[18] S. Herminghaus, Advances in Physics **54**, 221 (2005).

[19] N. Mitarai and F. Nori, Advances in Physics **55**, 1 (2006).

[20] I. Aranson and L. Tsimring, *Granular Patterns*, 1st ed. (Oxford University Press, Oxford, UK, 2009).

[21] J. N. Israelachvili, *Intermolecular and Surface Forces*, 3rd ed. (Academic Press, Elsevier, Oxford, UK, 2011).

[22] C. D. Willett, M. J. Adams, S. A. Johnson, and J. P. K. Seville, Langmuir **16**, 9396 (2000).

[23] J. S. M. Farlane and D. Tabor, Proceedings of the Royal Society of London. Series A, Mathematical and Physical Sciences, The Royal Society (1950).

[24] M. M. Kohonen *et al.*, Physica A **339**, 7 (2004).

[25] Z. Fournier *et al.*, J. Phys. : Condens. Matter **17**, S477 (2005).

[26] T. G. Mason, A. J. Levine, D. Ertas, and T. C. Halsey, Phys. Rev. E **60**, R5044 (1999).

[27] D. J. Hornbaker *et al.*, Nature **387**, 765 (1997).

[28] T. C. Halsey and A. J. Levine, Phys. Rev. Lett. **80**, 3141 (1998).

[29] P. Richard *et al.*, Nature Materials **4**, 121 (2005).

[30] C. Radin, J Stat Phys **131**, 567 (2008).

[31] J. B. Knight *et al.*, Phys. Rev. E **51**, 3957 (1995).

[32] P. Philippe and D. Bideau, Europhys. Lett. **60**, 677 (2002).

[33] M. Nicolas, P. Duru, and O. Pouliquen, Eur. Phys. J. E **3**, 309 (2000).

[34] G. D. Scott, A. M. Charlesworth, and M. K. Mak, J. Chem. Phys. **40**, 611 (1964).

[35] C. Josserand, A. V. Tkachenko, D. M. Mueth, and H. M. Jaeger, Phys. Rev. Lett. **85**, 3632 (2000).

[36] J. E. Fiscina, G. Lumay, F. Ludewig, and N. Vandewalle, Phys. Rev. Lett. **105**, 048001 (2010).

[37] T. Aste, M. Saadatfar, and T. J. Senden, J. of Statistical Mechanics: Theory and Experiments **July**, P07010 (2006).

[38] T. Aste, M. Saadatfar, and T. J. Senden, Phys. Rev. E **71**, 061302 (2005).

[39] Mario Scheel, Ph.D. thesis, Georg-August Universität, Göttingen, Germany, (2009).

[40] R. A. Fisher, J. Agric. Sci. **16**, 492 (1926).

[41] A. J. Liu and S. R. Nagel, Nature **396**, 21 (1998).

[42] C. S. O'Hern, S. A. Langer, A. J. Liu, and S. R. Nagel, Phys. Rev. Lett. **88**, 075507 (2002).

[43] C. S. O'Hern, L. E. Silbert, A. J. Liu, and S. R. Nagel, Phys. Rev. E **68**, 011306 (2003).

[44] M. E. Cates, M. D. Haw, and C. B. Holmes, J. Phys.: Condens. Matter **17**, (2004).

[45] C. F. Moukarzel, Phys. Rev. Lett. **81**, 1634 (1998).

[46] G. Mason and W. Clark, Nature **216**, 826 (1967).

[47] G. Mason and W. Clark, Nature **219**, 149 (1968).

[48] M. Scheel *et al.*, Nature Materials **7**, 189 (2008).

[49] M. Scheel *et al.*, J. Phys.: Condens. Matter **20**, (2008).

[50] M. Schaber, Master's thesis, Universität des Saarlandes, Saarbrücken, Germany, (2010).

[51] R. Seemann, W. Mönch, and S. Herminghaus, Europhys. Lett. **55**, 698 (2001).

[52] S. Herminghaus, T. Paatzsch, T. Häcker, and P. Leiderer, Europhys. Lett. **31**, (1995).

[53] H. Musil, S. Herminghaus, and P. Leiderer, Surface Science Lett. **294**, L919 (1993).

[54] K. D. Sattler, *Handbook of Nanophsyics - Principles and Methods*, 222 ed. (CRC Press, Taylor and Francis Group, New York, 2011).

[55] A. Samadani and A. Kudrolli, Phys. Rev. Lett. **85**, 5102 (2000).

[56] A. Samadani and A. Kudrolli, Phys. Rev. E **64**, 051301 (2001).

[57] D. Geromichalos, M. M. Kohonen, F. Mugele, and S. Herminghaus, Phys. Rev. Lett. **90**, 168702 (2003).

[58] P. C. F. Møller and D. Bonn, Europhysics Lett. **80**, 38002 (2007).

[59] J. E. Fiscina *et al.*, Physical Review E **86**, 020103 (2012).

[60] R. R. Hartley and R. P. Behringer, Nature **421**, 928 (2003).

[61] N. W. Mueggenburg, Physical Review E **71**, 031301 (2005).

[62] R. Mani, D. Kadau, and H. J. Herrmann, Granular Matter **15**, 447 (2013).

[63] H. Rumpf, *The strength of granules and agglomerates*, aggolomeration ed. (Interscience Publishers, New York, 1962).

[64] B. N. J. Persson, *Sliding Friction- physical principles and applications*, 2nd ed. (Springer, Heidelberg, Germany, 2000).

[65] J. C. Géminard, W. Losert, and J. P. Gollub, Phys. Rev. E **59**, 5881 (1999).

[66] S. Nasuno, A. Kudrolli, A. Bak, and J. P. Gollub, Phys. Rev. E **58**, 2161 (1998).

[67] S. Nasuno, A. Kudrolli, and J. P. Gollub, Phys. Rev. Lett. **79**, 949 (1997).

[68] D. R. Lide, *CRC Handbook of Chemistry and Physics*, 89 ed. (Taylor & Francis, New York, 2009).

[69] S. Maenosono, C. D. Dushkin, and Y. Yamaguchi, Colloid & Polymer Science **277**, 993 (1999).

[70] O. Pitois, P. Moucheront, and X. Chateau, J. of Colloid and Interface Science **231**, 26 (2000).

[71] M. Sipahi, Master's thesis, Georg-August Universität, Göttingen, Germany, (2009).

[72] G. Wypych, *Handbook of Solvents* (ChemTec Publishing, Toronto, Canada, 2001).

[73] N. S. Cheng, Ind. Eng. Chem. Res. **47**, 3285 (2008).

[74] C. W. Extrand and S. I. Moon, Langmuir **24**, 9470 (2008).

[75] C. Geyer and K. Daniilidis, *Computer Vision - ECCV in LNCS2351* (Springer, Copenhagen, Denmark, 2002).

[76] M. Schwamberger, Master's thesis, Georg-August Universität, Göttingen, Germany, (2008).

[77] K. A. Brakke, Phil. Trans. R. Soc. A **354**, 2143 (1996).

[78] R. H. Ewoldt, P. Winter, J. Maxey, and G. H. McKinley, Rheol Acta **49**, 191 (2010).

[79] A. P. Sheppard, R. M. Sok, and H. Averdunk, Physica A **339**, 145 (2004).

[80] H. Averdunk and A. Sheppard, Mango - 3D image analysis toolkit, http://xct.anu.edu.au/mango, (2010).

[81] Kamaljit Singh, Ph.D. thesis, University of New South Wales, Canberra, Australia, (2009).

[82] A. B. Limaye, Drishiti - Volume Exploration and Presentation Tool, http://anusf.anu.edu.au/Vizlab/drishti/, (2010).

Eidesstattliche Versicherung

Hiermit versichere ich an Eides statt, dass ich die vorliegende Arbeit selbstständig und ohne Benutzung anderer als der angegebenen Hilfsmittel angefertigt habe. Die aus anderen Quellen oder indirekt übernommenen Daten und Konzepte sind unter Angabe der Quelle gekennzeichnet. Die Arbeit wurde bisher weder im In- noch im Ausland in gleicher oder ähnlicher Form in einem Verfahren zur Erlangung eines akademischen Grades vorgelegt.

Somnath Karmakar

Saarbrücken, 30.01.2014